UNI KASSEL VERSITÄT

CINSaT Center for Interdisciplinary Nanostructure Science and Technology

AGE

MASTER THESIS

Physical Characterization and Motion Dynamics of Exchange-Biased Janus Particles

submitted by

B.Sc. Meike Reginka

14th June 2018

Study program: Nanoscience

Supervised by Prof. Dr. Arno Ehresmann and Dr. Dennis Holzinger

Cooperation Partners:

JYVÄSKYLÄN YLIOPISTO
UNIVERSITY OF JYVÄSKYLÄ

INA Institut für Nanostrukturtechnologie und Analytik

Assessors: Prof. Dr. Arno Ehresmann
                    Prof. Dr. Thomas Kusserow

Not everything that can be counted counts, and not everything that counts can be counted.

Albert Einstein

CONTENTS

CHAPTER 1

INTRODUCTION

'Honey, I shrunk the lab.'

With this title an article about microfluidics from 2002 stressed how the interests of life science have guided research towards the miniaturization of conventional laboratory devices onto the 'size of a postage stamp' within the last decades.[Kni02] The fact that a whole range of scientific journals like *Lab on a chip* and *Langmuir* are devoted to these predominantly interdisciplinary scientific objectives, like microfluidics, e.g, for miniaturized biological studies, functionalized colloids or nanomaterials etc., emphasizes the motivation of researchers within this field.

The focus of so-called lab-on-a-chip technologies is on the development of reliable and fast analysis methods that are cost-effective and can be easily operated, thus, pleasing the sophisticated needs in life science, e.g., for medial diagnostics or biochemical interaction analysis. Besides these promising advantages, the miniaturization demands control of microscopic actuators as well as handling fluid volumes in the micro- or nanoliter range for applications. One challenging task is to ensure the mixing of small liquid volumes, since mass transport is governed by molecular diffusion under laminar flow conditions with vanishing turbulences. An elegant way is the use of microparticles as active stirrers, which can be guided in the fluid by external stimuli, e.g. by electric or magnetic fields.[HLG12] Aside from the mixing, controllable microparticles can also serve as miniaturized sensors. When using magnetic particles with superparamagnetic properties, tracing their trajectory, e.g., in magnetophoresis, can reveal information about its environmental interaction when passing by the fluid chamber. With this in mind, the microspheres can e.g. serve as microrheological probes for unraveling characteristics and modifications in the microfluidic environment.[BAM05] Moreover, the microspheres also prove to be useful as actuators and carriers, when a remotely controllable transport within the microfluidic environment is enabled.[RLL16,HKB15] A future goal in biomedical applications is an *in vivo* particle transport with targeted drug delivery based on carrier particles with tailored degradation properties in which a drug is enclosed and can be released in a controlled fashion.[YSG16,BMS12,SKH16]

A highly versatile type of magnetic microparticles is represented by so-called Janus particles that are characterized by two faces with differing unique properties. These spherical but anisotropic bodies can e.g. be manufactured by coating only one hemisphere of non-magnetic microparticles with a magnetic thin film. In comparison to isotropic magnetic particles, Janus particles feature a major advantage due to their asymmetry: not only their translational but also rotational degrees of freedom can be directly accessed by the application of external magnetic fields. The rotational mobility of such a particle is related to a different dependence on its hydrodynamic radius than the translocation, which is due to the radius-dependence of viscous torque and force, respectively. Furthermore, the Janus particles' surface can be partly functionalized with a biomolecule whose interaction with other components in the liquid environment is of interest. The remote control of the magnetoresponsive particle's rotational degrees of freedom can perspectively enhance the sensitivity of biomolecular interaction analysis, since changes in the particle's dynamics, both translational and rotational, can be used to sense physiological modifications in the environment and conformational changes of the coupled biomolecule.

A lot of previous research has been performed on Janus particles with ferromagnetic caps including magnetic characterization[MNS14,SKS12,ZWM09,ALS10] and microfluidic experiments.[YBB12,SKP11] In contrast to magnetic Janus particles described in literature, the present work intends to introduce an additional, unidirectional magnetic anisotropy to the Janus particles to manipulate their magnetic state in a desired fashion. Since the magnetization state in solely ferromagnetic caps is strongly influenced by magnetocrystalline anisotropy of the ferromagnetic material, the particle diameter and the ferromagnetic layer thickness, three states were distinguished in parameter dependent phase diagrams: vortex, onion and out-of-plane magnetization. The studied ferromagnetic caps were shown to energetically favor the vortex state in the micrometer rage. Due to the limitation of these phases' presence by the experimental boundary conditions, the desired onion state can probably not be realized for a particle size that is detectable with conventional light microscopes in microfluidic applications. In order to specifically manipulate the magnetic state towards the onion phase in micrometer-sized Janus particles, an additional magnetic anisotropy will be introduced: the exchange bias. This effect refers to a unidirectional anisotropy that arises in thin film systems containing an antiferromagnetic layer aside of a ferromagnetic layer due to a coupling of the interfacial magnetic moments. The result is a shift of the ferromagnet's hysteresis curve, which offers the possibility to fix a certain magnetization state within the system, which can furthermore be modified at a later stage.[ESW11] The research on exchange-biased thin film systems has so far focused on laterally-homogeneous and planar samples, while the deposition on top of microspheres is accompanied by curvature induced effects on the magnetization texture.[ZWM09] From the deposition procedure a lateral variation of the film thickness from the cap's center towards its equatorial region is expected due to the underlying curvature of the particle, thus, creating a cap with a crescent shaped cross-section.[ALS10]

The central scientific objectives of the present work are: 1. the introduction of a reproducible fabrication route for exchange-biased Janus particles, 2. their structural and 3. magnetic characterization, and 4. theoretical and experimental investigations on the Janus particles' rotational dynamics in rotational external magnetic fields when exposed to different microfluidic media.

- It will be shown, that the developed fabrication procedure is based on the self-assembly of the templating non-magnetic microparticles and the subsequent sputter deposition of the exchange bias layer system in chapter 3.

- Next, the shape and geometry of the curved thin film will be characterized in section 5.1 using imaging techniques, such as scanning electron microscopy and atomic force microscopy. The electron micrographs of a Janus particle's cross section processed by focused ion beam will be presented, where the thickness gradient present on the sphere is estimated. This value is desired for the determination of the ferromagnetic volume which gives rise to the particles' effective magnetic moment. Additionally, the surface properties of the curved thin film and the connecting sites between the spheres located in the self-assembled array will be investigated.

- Within the third objective a monolayer of Janus particles will be magnetically characterized by Kerr magnetometry in order to confirm the presence of an exchange bias in subsection 2.4.1. The microscopic analysis of a solitary particle's magnetic net charge pattern will be accomplished by magnetic force microscopy. In contrast to the typically in ferromagnetic caps observed vortex state for the used particle size, it will be shown that the here investigated particles are described by an onion state for the for the equilibrium magnetization. Along with this observation, a comparison between the exchange bias on the spherical half shell and a planar thin film system will be drawn.

- In order to analyze the fabricated particles for their ability to coherently rotate with an external magnetic field, proof-of-concept experiments with Janus particles in microlfuidics will be outlined in section 5.5. The identification of regimes for the frequency and the strength of the applied driving field with a stable rotation of the particle synchronously with the magnetic field in contrast to asynchronous motion will be in focus of the investigation. For the comparison of the experimental findings to theoretical predictions a model will be developed in section 5.4, which is based on the viscous and magnetic torque acting on the particle exposed to rotating magnetic field.

CHAPTER 2

THEORETICAL BACKGROUND

2.1 Magnetic Interactions and Anisotropy Effects

One of the most important and interesting aspects about magnetic matter is the occurrence of anisotropies, thus, offering a specifically addressable material class with direction-dependent properties. In contrast to isotropic physical quantities, anisotropic properties are characterized by a dependence on direction. The interplay of magnetic anisotropy effects can be seen as the origin of preferred magnetization directions of the material, named easy axes. Aiming to understand the origins of magnetic order and anisotropy, first, some essential interactions between single magnetic moments will be addressed. Due to the magnetic moment's inverse dependence on the particle's mass, the description of magnetism is mainly governed by the magnetic moments of electrons and, thus, the influence of nuclei can be neglected.[BS05] Subsequently, the subsections of this chapter are dedicated to the individual anisotropies.

Starting with the interaction between individual magnetic dipoles, the dipole-dipole interaction energy depending on the distance between two dipoles and their relative orientations can be described as

$$E_{\mathrm{DD}} = \mu_0 \left(\frac{\vec{m}_1 \cdot \vec{m}_2}{|\vec{r}|^3} - 3 \frac{(\vec{m}_1 \cdot \vec{r}_1)(\vec{m}_2 \cdot \vec{r}_2)}{|\vec{r}|^5} \right) \tag{2.1.1}$$

with the vacuum permeability μ_0, the magnetic moments $\vec{m}_1$ and $\vec{m}_2$ as well as their positions $\vec{r}_1$ and $\vec{r}_2$ and their distance vector $\vec{r} = \vec{r}_2 - \vec{r}_1$.[BS05] However, the interaction cannot be presumed to be the origin of ferromagnetic order in a magnetic material, because it is to small in comparison to the thermal energy which corresponds to material specific order temperatures (i.e., Curie temperature), but as a long-range effect it certainly accounts for anisotropies.[BS05,Get08]

The interaction mediating magnetic order is the quantum mechanical exchange interaction, which is based on the fact that electrons as fermions are indistinguishable. The assumption that two electrons with individual wave functions Ψ_{a} and Ψ_{b} are indistinguishable requests their squared total wave function to be invariant upon their exchange. Since both particles are

fermions underlying Pauli's exclusion principle, the total wave function needs to be a combination of a symmetric spatial function with an antisymmetric spin function or a vice versa, thus, leading to corresponding singlet or triplet states.[Get08] The consequence for electrons in solid state material is the following: if two electrons have a parallel spin orientation (triplet), their spatial wave functions cannot coincide. By this quantum-mechanically requested spatial separation the potential energy contribution from electrostatic Coulomb interaction is reduced. On the other hand, this increased spin polarization demands the occupation of higher energetic levels in the material's band structure, which raises the kinetic energy. Only in material specific cases in which the potential energy diminishment exceeds the enhancement of the kinetic energy, a magnetic order within the sample is favored. As a measure the exchange constant J is introduced by the energy difference between the triplet and the singlet state, where positive values account for ferromagnetism and negative ones for antiferromagnetism.[BS05] A prominent way to address the exchange coupling in solid state materials is shown in the isotropic Heisenberg model with the Hamiltonian

$$\mathcal{H} = - \sum_{ij} J_{ij} \mathcal{S}_i \cdot \mathcal{S}_j, \tag{2.1.2}$$

where all exchange interaction contributions of nearest neighbors i, j with the exchange constant J_{ij} for all pairs of spins $\mathcal{S}_i$ and $\mathcal{S}_j$ are added.[Get08]

The second quantum mechanical phenomenon regarding magnetism is the spin-orbit interaction causing an electron's spin $\vec{s}$ and its orbital angular momentum $\vec{l}$ to couple to a total angular momentum $\vec{j}$. Here, the intermediary is the gradient of the nucleus' electrostatic Coulomb potential and the coupling can be conceived by simplifying the electron's motion to an orbit around its nucleus. From the electron's frame of reference the nucleus circulates around the electron generating a magnetic field that can interact with the spin of the electron itself.[BS05] By this, a spin orientation parallel to the created magnetic field is energetically preferred compared to the antiparallel case. Consequently, the favored spin orientations within a crystalline material are connected to its crystal structure. This effect is particularly prominent for materials of heavy atoms, since the mediating Coulomb potential gradient is comparatively high. In this case, the spin and orbital angular momenta of each individual electron couple to the individual total angular momenta j that are furthermore coupled to each other (jj-coupling). In contrast, for light atoms the coupling amongst the individual spins and orbital angular momenta of the electrons is stronger than the spin-orbit coupling, resulting in the so-called LS-coupling.[BS05]

2.1.1   Shape Anisotropy

Due to the long-ranging character of the dipolar interaction, the magnetic dipoles within a sample are exposed to a dipolar field that is mainly dominated by the dipoles present at the sample's surface, which consequently is the location of stray field generating, uncompensated magnetic charges. Based on this, a correlation between the sample's geometry and its magnetization direction results in shape-induced easy axes. Only for spherical objects of polycrystalline kind a genuinely isotropic magnetization is observed, since the magnetocrystalline anisotropy axes

of the individual crystallites cancel out macroscopically and, hence, no shape anisotropy is present.[Get08] Comparatively, in infinite planar films an energetic minimum for a completely homogeneously in-plane magnetized sample can be found due to shape anisotropy.[BS05] However, in any other geometry than these only inhomogeneous magnetization distributions lead to stray field energy minima. Although the reduction of the planar film to finite dimensions such as in magnetic thin film systems introduces boundary conditions that inhibit the solely uniform magnetization, a dominating shape-induced in-plane anisotropy is present due to the high aspect ratio of mostly square centimeter-sized area to nanometer-scaled thickness of the films.

2.1.2 Magnetocrystalline Anisotropy

If magnetization curves of materials with different crystal structures, such as face-centered cubic, body-centered cubic or hexagonal close-packed, are measured, it can be observed that saturation is achieved at smaller magnitudes of external magnetic fields when the measurement is performed in a specific alignment with one of the sample's crystallographic axes, named easy axes.[HS09] Here, the above-depicted spin-orbit coupling comes into play and the alignment of easy magnetization directions along crystallographic axes can be examined in more detail. Every crystalline structure of magnetically ordered materials, like transition or rare earth metals, comes along with an anisotropically distributed density of the exchange-coupled d- or f-electrons, which are responsible for the magnetic appearance of the sample. As soon as exchange-coupled spins are rotated, they exert a torque on the orbital angular momenta they are coupled to via spin-orbit interaction, leading to the likewise rotation of the latter. In particular, this means that a rotation of the spins, i.e., the magnetic moments within a crystal, causes a rotation of the orbital angular momenta. Due to the following changes in the wave functions' overlap from neighboring atoms, the energy becomes direction dependent. Because of this, the magnetization along certain axes of the crystallographic structure is energetically preferred to others, which is expressed in the material's anisotropy constants K_{an}.[BS05] Focusing on cubic crystals such as Iron or Nickel it can be shown by a series expansion of the energy density into magnetization components in polar coordinates that the energy density exhibits minima along three axes equivalent to a certain set of crystal lattice directions. For the thin film samples used in this work the symmetry can furthermore be reduced, since the shape anisotropy (subsection 2.1.1) determines the preferred plane for the magnetization and, therefore, leads to the presence of two easy and two hard axes within a thin film of cubic crystal structure. Hexagonal lattices often show a uniaxial anisotropy so that these materials are characterized by a single easy axis only.[HS09]

Important parameters that affect the strength of the magnetocrystalline anisotropy are the temperature and the stoichiometry of the applied alloy, whereby both factors have a strong influence on the anisotropy constants.[Get08] Lowering the dimensions of the specimen down to a thin film furthermore influences the magnetocrystalline anisotropy for which the term **magnetic interface anisotropy** is used. A reduced film thickness increases the surface-to-volume ratio and, thus, the breaking of the translation invariance of the crystal lattice at the surface or the interface is emphasized compared to bulk media. Due to this, the spin-orbit interaction causes the appearance of a net anisotropy orthonormal to the film surface. In order to include this in

the quantitative perspective of magnetocrytsalline anisotropy, an effective anisotropy constant K_{eff} is introduced as

$$K_{\text{eff}} = K_{\text{V}} + 2 \cdot \frac{K_{\text{S}}}{t_{\text{F}}} \tag{2.1.3}$$

with K_{V} and K_{S} as the volume and surface dependent contributions, respectively.[Get08] In Equation 2.1.3, the factor of two is added to include both surfaces of the film. In the second part of the equation, the inverse dependence on the ferromagnetic film thickness t_{F} is considered, emphasizing its importance for thin films. A critical film thickness can be derived as $d_{\text{F,c}} = -2 \cdot K_{\text{S}}/K_{\text{V}}$ below which an out-of-plane magnetization is preferred. Comparatively, in thicker films, where K_{V} dominates, an in-plane-magnetization is favored. Exemplary, a Co film in a Co/Pd multilayer has a critical thickness of 12 Å.[Get08]

2.1.3 Unidirectional Anisotropy, Exchange Bias (EB)

Extending the picture from ferromagnetic thin films to magnetic thin film multilayers, another anisotropy is introduced as soon as an interface between a ferromagnet (F) and an antiferromagnet (AF) is involved. This unidirectional exchange anisotropy in AF/F heterostructures is referred to as exchange bias (EB) and it comes along with a shift of the magnetization curve along the applied field axis resulting in a hysteresis loop not centered around zero external magnetic field but around the so-called exchange bias field H_{EB} as it is shown in Figure 2.1. The effect originates from the exchange interaction of the magnetic moments at the interface shared by F and AF.[MB57] The second characteristic of exchange bias systems is the increase of the coercivity compared to that of an individual ferromagnetic layer. Under the condition that H_{EB} is larger than H_{C} and in the case of steep slopes of the hysteresis only a single macroscopic magnetization state is realized for the ferromagnetic layer within the EB system in absence of an external magnetic field (remanent magnetization). Consequently, the anisotropy can be called unidirectional rather than uniaxial, since the two energetic minima present at 0 and 180 Â° are not degenerated. The effect is typically initialized by a field cooling procedure in which the layer system is heated to a temperature above the Néel temperature of the AF (blocking temperature for polycrystalline samples), but below the ferromagnetic Curie temperature, and subsequently cooled down in an external magnetic field that saturates and, thereby, aligns the F's magnetization parallel to this field direction. During the process, the F keeps its saturated order while the AF is first transferred to a paramagnetic phase and is then, during cool-down, aligned with its interfacial moments parallel to the F's magnetization due to the exchange interaction. Since the F's moments close to the interface are coupled to the AF moments, the magnetization reversal appears at higher magnitudes of external magnetic fields antiparallel to the initially set magnetization and, hence, resulting in the shift of the hysteresis curve.

Due to its unique characteristics, the EB is e.g. being used as a reference electrode in spin valve applications (with one pinned and one free ferromagnetic layer) which can be found in data storage devices such as read-and-write heads of hard disks and magnetic random access memory (MRAM).[RZ08] Because of the variety of used fabrication techniques and material systems influencing structural characteristics like the crystallinity and the interfacial properties
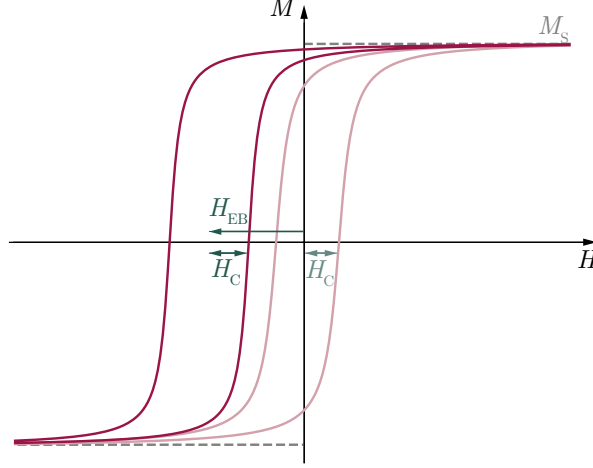
Figure 2.1: Magnetization curves in dependence of the externally applied magnetic field in parallel geometry to the main anisotropy axis of the specimen: Shifted hysteresis loop (red) of an EB system compared to the initial hysteresis of a ferromagnet (light red). The characterizing exchange bias field H_{EB}, the coercive field H_C and the saturation magnetization M_S are indicated.

of the EB systems, there is still no overall theory explaining all experimental findings in good agreement. In the following some models will be briefly presented with focus on polycrystalline layer systems due to their relevance for this work.

In 1956, when MEIKLEJOHN and BEAN first discovered the EB effect, they proposed a model to estimate the exchange bias field of the sample under the condition that both AF and F consist of single domains and share an atomically smooth interface.[MB56] Both materials exhibit a uniaxial in-plane anisotropy and the AF is assumed to be magnetically rigid during the F's coherent magnetization reversal in an external magnetic field (Ansatz from Stoner-Wohlfahrt-Model), which can be described as an infinitely large antiferromagnetic anisotropy constant. By further assuming a fully uncompensated spin structure at the interface, i.e., only ferromagnetically coupled magnetic moments, the exchange bias field can be modeled via the interfacial exchange energy per unit area J_{EB}

$$H_{EB} = -\frac{J_{EB}}{\mu_0 M_S t_F}, \tag{2.1.4}$$

where M_S is the ferromagnetic saturation magnetization and t_F the ferromagnetic layer thickness.[MB56] This equation includes the reciprocal dependence of the EB field on the ferromagnet's thickness, which was experimentally validated for several material systems.[RZ08,MSB87] Within a certain thickness regime the linear approximation of the thickness dependence holds, but for very thin and not continuous layers as well as for thick layers exceeding the domain wall length of the material the relation is not valid.[Müg16] The dependence is illustrated by experimental findings on a FeMn/NiFe system obtained by MAURI *et al.* as shown in Figure 2.2 together with the trend for the AF's thickness presented by JUNGBLUT *et al.*, where H_{EB} reaches a plateau for thicknesses above a certain threshold.[MSB87,JCJ94]

However, theoretical predictions of this model resulted in significantly larger values for H_{EB} and H_C than obtained from experiments, which led to further developing EB models during
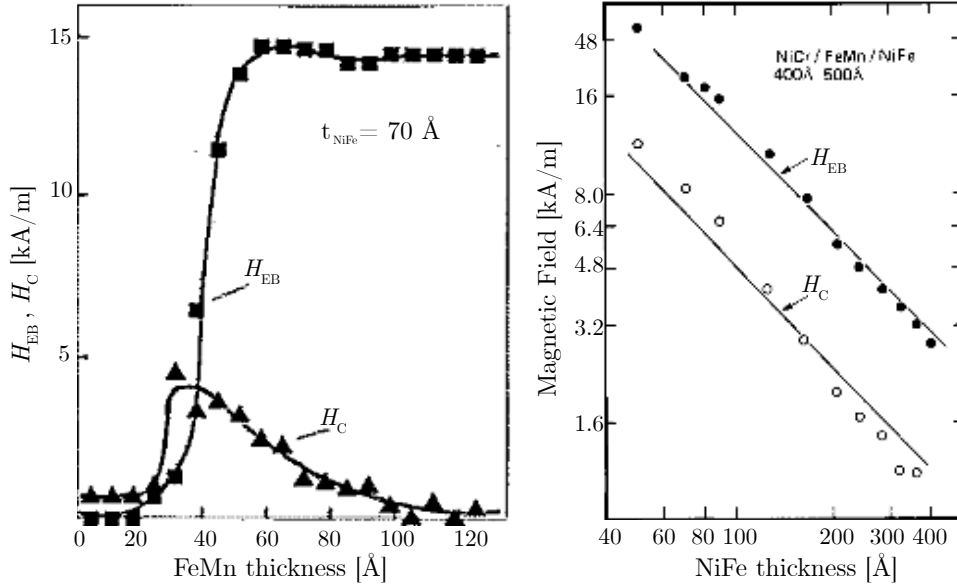
Figure 2.2: Left: H_{EB} and H_C over AF (FeMn) thickness for a [111] oriented sample and $t_F = 70\,\text{Å}$.[JCJ94] Right: H_{EB} and H_C vs. F (NiFe) thickness in a system of NiCr(400 Å)/FeMn(500 Å). The lines indicate the $1/t_F$ dependence of both properties.[MSB87]

the last 62 years.[RZ08] Soon, a more differentiated picture was desired and the focus was put on the properties of the AF,[MB57] the interfacial texture, and the formation of domains, and these contributions were included in the following approaches.[RZ08] Especially for polycrystalline samples, certain considerations needed to be implemented to the EB perspective. One early example is the picture created by FULCOMER and CHARAP, which suggests small single-domain AF grains (rather than a single domain AF) that show no interaction amongst each other and posses individual anisotropy constants $K_{AF,i}$ and volumes $V_{AF,i}$ as a result of the material's grain size distribution and the correlated size dependence of material parameters.

2.1.4 Further Anisotropies

As stated in subsection 2.1.2, magnetic alloys of cubic crystal structure exhibit easy axes due to the magnetocrystalline anisotropy. In order to access its magnitude and emphasize a rather uniaxial or even a unidirectional anisotropy in the specimen, it can be annealed in an external magnetic field. In particular, the sample's magnetization is oriented in an external field at a high temperature not exceeding the Curie temperature, where atomic diffusion and migration processes are thermally activated. During cool-down, the positions of the reoriented atoms become locked in place so that the magnetization state is frozen out and the unidirectional **induced anisotropy** parallel to the annealing field direction is set.[CG97]

Another effect that can be observed in ferromagnets is the change of its anisotropy upon mechanical deformation, which is defined by the **magnetoelastic energy**. Vice versa the phenomenon of a deformation of the sample's shape during the magnetization process is called magnetostriction and although the relative deformations are typically in the range of $\Delta l/l = 10^{-5}$ to 10^{-6}, they play an important role for domain structures of soft magnetic materials.[BS05,CG97]

2.2   Micromagnetic Description

Regarding the magnetic microstructure of an object, there are different possibilities to face this physical phenomenon from different perspectives regarding the lateral dimensions of the problem. First of all, there is the *atomic level theory* that elucidates elementary magnetic moments and their connection to the crystal lattice. However, if the sample size exceeds 1 nm, *micromagnetic analysis* is performed, in order to reveal the internal structure of domain walls in terms of continuum theory, the dynamics of magnetization processes, and stability limits. Once the dimensions are in the range of micrometers, the more global approach of *domain theory* is applied, in which the spatial arrangement of domains and their boundaries is studied. Together, micromagnetics and domain theory offer a mesoscopic picture that can furthermore be expanded by magnetization distribution functions in *magnetic texture analysis.*[HS09]

In the described mesoscopic viewpoint, the sum of all energy contributions can be understood as an effective magnetic field acting on the individual magnetic moments in the investigated system. The basic task is to find a static equilibrium state for the magnetization in which the torque exerted by this effective magnetic field on the single magnetic moments completely vanishes. In a static (not dynamic) case, this is done by choosing the appropriate vector field of the reduced magnetization $\vec{m}(r) = \vec{M}(r)/M_{\mathrm{s}}$ in order to minimize the ferromagnet's total free energy E_{tot} as it has been presented by Landau and Lifshitz in 1935 considering the following terms:[HS09]

- First of all, the **volume exchange stiffness energy** E_{ex} is described as the ferromagnet's energy term that is equal to zero for a constant equilibrium magnetization. It is derived from the Heisenberg model, while the magnetization vector field's gradient is used to describe the discrepancy from the desired solely parallel alignment of the magnetic moments:

$$E_{\mathrm{ex}} = A \int (\mathrm{grad}\ \vec{m})^2 \mathrm{d}V \qquad (2.2.1)$$

  with the material and temperature dependent exchange stiffness constant A_{ex}[HS09] that includes not only the exchange constant J but also the number of nearest neighbors and the distance between them.[CG97]

- As a second factor influencing the magnetization direction $\vec{m}$, the direction-dependent energy contributions are introduced via the **anisotropy energy** density $\mathcal{E}_{\mathrm{an}}$ that collects all the present magnetic anisotropies in the system. Exemplary, the energy density for a thin film system with cubic crystal structure is given as

$$E_{\mathrm{an}} = \int \mathcal{E}_{\mathrm{an}}\ \mathrm{d}V = \int K_{\mathrm{cub}} \sin^2(2\phi)\ \mathrm{d}V \qquad (2.2.2)$$

  with the material-specific anisotropy constant of the cubic crystal K_{cub}. This equation results in four energetic minima for the alignment of the ferromagnet's magnetization.[HS09] Although the magnitude of the magnetocrystalline energy is small compared to the exchange energy, it remains the main factor determining the magnetization direction as the exchange energy only asks for parallel aligned moments without dictating their direction.

The considerable anisotropies, their physical origins, and their single influences were discussed in more detail in section 2.1, while especially shape-induced anisotropy effects are not contained here, but are rather taken into account in the stray field energy described below.[HS09]

- Next, the interaction energy arising from the external field $\vec{H}_{\text{ex}}$ that surrounds the magnetization vector field $\vec{m}$ is described as[HS09]

$$E_{\text{Z}} = -M_{\text{S}} \int \vec{H}_{\text{ex}} \cdot \vec{m} \ \mathrm{d}V. \tag{2.2.3}$$

This term also referred to as **Zeeman energy** adds up to the magnetic field energy with the next term, the stray field energy.

- The emergence of stray fields from the magnetic body itself can be understood from Maxwell's equation $\mathrm{div}\vec{B} = 0$ that prohibits magnetic monopoles in the first place and, thereby, requests a flux closure, which can be achieved via this stray field and the demagnetizing field $\vec{H}_{\text{ex}}$ that is internally opposed to the magnetization. Editing the equation by inserting $\vec{B} = \mu_0 \vec{H}_{\text{d}} + \vec{M}$, it can be seen from[HS09]

$$\mathrm{div}\vec{H}_{\text{d}} = -\mathrm{div}(\vec{M}/\mu_0) \tag{2.2.4}$$

that sinks and sources in the magnetization appear as net magnetic charges for the demagnetizing field. It should be strongly pronounced that this concept of magnetic charges only holds true for this picture and that individual magnetic charges never appear isolated as it is the case for electric charges creating electric fields. The resulting **stray field energy** E_{d} in a finite sample can be written as[HS09]

$$E_{\text{d}} = -\frac{1}{2} \int \vec{H}_{\text{d}} \cdot \vec{M} \mathrm{d}V. \tag{2.2.5}$$

Making use of the stray field's potential Φ_{d}, the mentioned magnetic charges can be incorporated as the reduced volume charge density $\lambda_{\text{V}} = -\mathrm{div}\,\vec{m}$ and the surface charge density $\sigma_{\text{s}} = \vec{m} \cdot \vec{n}$, where $\vec{n}$ is the surface normal vector. By this, Equation 2.2.5 results in[HS09]

$$E_{\text{d}} = \frac{1}{2} M_{\text{s}} \left[\int \lambda_{\text{V}} \Phi_{\text{d}} \mathrm{d}V + \int \sigma_{\text{s}} \Phi_{\text{d}} \mathrm{d}S \right]. \tag{2.2.6}$$

- In case that the studied ferromagnetic thin film shares an interface with an antiferromagnet, the exchange bias effect has to be considered. Formally, the energy contribution from the unidirectional anisotropy can be implemented by an effective interlayer exchange constant J_{EB} and the angle θ between the induced anisotropy axis and the F's magnetization, which is assumed to be uniform. Integration over the interface then leads to:[HS09]

$$E_{\text{EB}} = -\int J_{\text{EB}} \cos(\theta) \, \mathrm{d}S. \tag{2.2.7}$$

Finally, the sum of all contributions in a thin film system (shape anisotropy considered) of cubic crystallinity can be integrated over the sample volume:[HS09]

$$E_{\text{tot}} = \int \big[\, A(\operatorname{grad}\vec{m})^2 \,+\, K_{\text{cub}}\sin^2(2\phi)$$
$$-\, \vec{H}_{\text{ex}}\cdot\vec{M} \,+\, \frac{1}{2}\vec{H}_{\text{d}}\cdot\vec{M} \,\big]\,\mathrm{d}V \,-\, \int J_{\text{EB}}\,\cos(\theta)\,\mathrm{d}S \tag{2.2.8}$$

Note that magnetoelastic effects are neglected in this depiction.

2.3 Magnetic Textures in Curved Geometries

Extending the thin film considerations elaborated before from planar cases to three-dimensional (3D) geometries, one will soon encounter new possibilities but also challenges in understanding the prevalent magnetic textures, domains, and their boundaries. Examples for 3D magnetic objects are those in which magnetic thin films possess a curved geometry due to a curved underlying substrate, e.g., ripple structures, wires, or spheres. Within the last decade, different curvilinear-shaped ferromagnets have been studied including the occurring anisotropies connected to the curviness and the arising magnetization textures.[SFK16]

One of these textures that gained a lot of attention in this field is the magnetic vortex. Considering exchange, anisotropy, and stray field energy minimization it is known that above a certain diameter micromagnetic discs will show a flux-closure alignment of magnetic moments, i.e. vortices, where stray fields are only created by the vortex core, but that it is unlikely for small discs due to the high impact of exchange energy in the core. Soon investigations on magnetic rings with rectangular cross sections started because the removal of the vortex core from a disc geometry makes this texture more stable.[KVLD03] These hollow cylinders with a small height-to-radius ratio were produced by lift-off or lithography processes.[KVLD03] Looking at the magnetization switching behavior in external fields it was shown how these ring vortices (see Figure 2.3 a.) transition into a saturation configuration via the following steps: Starting with slight spin rotations (b.) in the applied field a reversed domain (bottom in c.) nucleates and then grows until the onion state (d.) with two domains, in which the moments still follow the circumference of the ring, is reached. With increasing field strength the ring will end up in a saturated single domain state dismantling the two domain walls (not shown).[KVLD03] Considering the contribution of exchange, anisotropy, and stray field energy within a ring, it was deduced that an increased height preferably leads to a vortex texture due to the quadratic influence of the height for the stray field energy, whereas thin rings with strong uniaxial anisotropies favor an onion formation.[KVLD03]

Since the fabrication of these novel 3D magnetic objects was realized, the topic has also been theoretically approached in order to understand the curvature effects and the behavior of the magnetization vector field.[GKS14] However, this problem seems far from being fully understood, especially for systems of arbitrary shape, as the main difficulty lies in the interplay between the curvilinear geometry of the underlying substrate and the nontrivial topology of the magnetization distribution within. In many cases, a strictly tangential treatment in which the magnetization
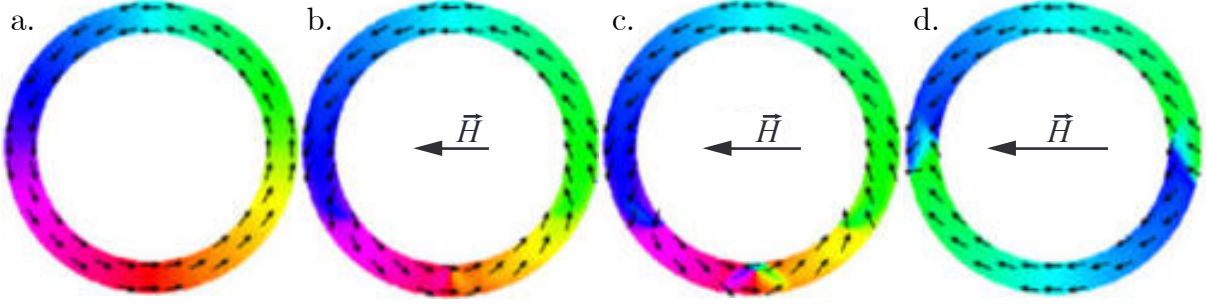
Figure 2.3: Magnetization distribution in a ferromagnetic ring at applied fields of increasing magnitude indicated by the arrow length. Explanations for the single images in the text. Adapted from[KVLD03]

vector field is bound to the curved surface was shown to be valid. Nevertheless, a closer look on an arbitrary magnetization distribution of a ferromagnet is desired, because the recent progress in microstructure fabrication makes complicated shapes of microscopic magnetic objects possible for which a strictly tangential perspective may be too restrictive.[GKS14] A 3D model based on exchange and general anisotropy contributions, that include shape anisotropy, thus, neglecting dipole-dipole aspects was derived by GAIDIDEI *et al.*.[GKS14] It gives the surface energy functional of a 3D magnetic shell in an anisotropic Heisenberg model under the condition that the shell's thickness t is smaller than its curvature radius:

$$E = t \int [\, l^2 \, \mathcal{E}_{\mathrm{ex}} + \lambda (\vec{m} \cdot \vec{n})^2 \,] dS. \tag{2.3.1}$$

Here, the first integrand represents the exchange energy density $\mathcal{E}_{\mathrm{ex}} = (\mathrm{grad}\,\vec{m})^2$ and the second term corresponds to the anisotropy energy density by taking into account for a uniaxial anisotropy. Here, n is the normal vector, l denotes the exchange length and λ the normalized anisotropy coefficient ($0 \leq |\lambda| \leq 1$), which is set to $\lambda = 1/2$ for soft and $\lambda = 1$ for hard magnetic materials) by the authors.[GKS14] Correspondingly, the domain wall width of the system is $\sigma = l/\sqrt{|\lambda|}$. The anisotropy coefficient λ expresses an easy-surface anisotropy for positive values and an easy-normal anisotropy for negative ones. For a strong easy-surface anisotropy the magnetization is dominated by its tangential component m_{t}. The expression of the total energy E can be done via a separation of the exchange energy density $\mathcal{E}_{ex}$ into a term $\mathcal{E}_{\mathrm{ex}}^0$ for the strictly tangential magnetization and a curvature-induced component which arises from a curvature-induced effective magnetic field F_{t}. This effective magnetic field points perpendicular to the main magnetization direction m_{t}, more explicitly, normal to the surface geometry, like shown in Figure 2.4. The same holds for the easy-normal anisotropy in a reverted manner, i.e., F_{n} points along the surface and perpendicular to the normal magnetization component m_{n}. The origin of this additional effective magnetic field in curvilinear geometries is due to two effects: an exchange component $\mathcal{E}_{\mathrm{ex}}^A$ that shows a curvature-induced anisotropic behavior and the effective Dzyaloshinskii-Moriya interaction (DMI) $\mathcal{E}_{\mathrm{ex}}^D$, which can be both considered as additional contributions to the exchange energy density

$$\mathcal{E}_{ex} = \mathcal{E}_{\mathrm{ex}}^0 + \mathcal{E}_{\mathrm{ex}}^A + \mathcal{E}_{\mathrm{ex}}^D \tag{2.3.2}$$
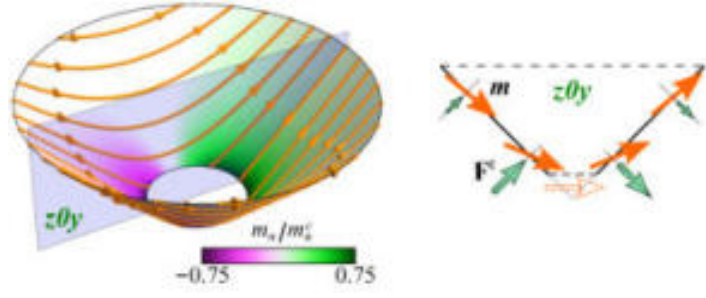
Figure 2.4: Left: onion state magnetization distribution in streamlines on a conical surface induced by a easy-surface anisotropy. The subordinate normal component m_n is indicated as a measure for the tilting. It is normalized by the ratio between the squared domain wall width and the squared cone radius $m_n^c = \sigma^2/R^2$. Right: schematic magnetization distributions and effective curvature-induced field F_t within the cross section of the cone in the plane $z0y$ indicated in the left image. [GKS14]

with the isotropic exchange expression $\mathcal{E}_{ex}^0$. [SKG15] For tangential anisotropies ($\lambda > 0$), it turns out that the curvature-induced effective magnetic field is zero only in planar films, but is present for every other kind of curvature. On the other hand, a strictly out-of-plane (surface normal) magnetization distribution based on an easy-normal anisotropy ($\lambda < 0$) can only be realized in spheres and cylinders when $F_n = 0$. [GKS14] The described effective curvature magnetic field is responsible for magnetization distributions with a tilting from the confining surface, which has been presented for an onion state in a cone surface. [GKS14] For visualization, the effective curvature field F_t for a tangential anisotropy is shown to be increased at positions with higher curvature on the cone in Figure 2.4. Once torsion comes into play, as it is the case in helices, it works together with the curvature to affect the tilt angle of the magnetization from the local surface.

Applying these general results from GAIDIDEI *et al.* to concrete geometries, like cylinders and spheres, the expressions for specific cases of other groups are concluded, of which also experimental proof has been furnished.

Correspondingly, the fact that the curvature induces exchange energy components which are anisotropic and even antisymmetric, like DMI, also allows for the explanation for magnetochiral effects. One example for a magnetic texture with magnetochiral properties is the above-described vortex. For flat circular shapes, e.g., discs, a vortex allows mostly divergence-free in-plane magnetization excluding the small core area. In these flat shapes, the clockwise or anticlockwise rotational sense of magnetization (chirality) and the upward and downward core orientation (polarity) are energetically degenerated. Due to this, the switching of the polarity is symmetrical with respect to the vortex chirality. [SKS14] In contrast, SLOIKA *et al.* were able to numerically show that the introduction of curvature lifts this degeneracy and depending on its chirality the switching of the vortex polarity from in- to outward ($p_{in} = -1$ to $p_{out} = 1$) or vice versa is accomplished by different amplitudes of an external magnetic field pulse. In a spherical magnetic cap the clockwise chirality requires smaller pulses to invert the vortex polarity and, hence, it can be seen that the curvature breaks the symmetry towards the polarity switching, which is present in planar systems. [SKS14]
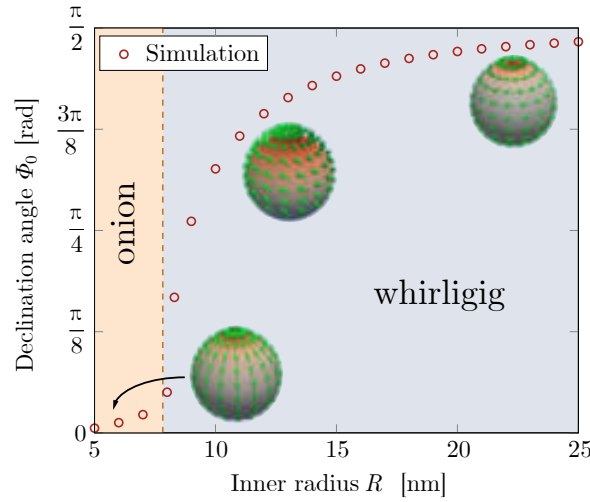
Figure 2.5: Results obtained by micromagnetic simulations for permalloy shells with a thickness of 10 nm. The declination angle strongly depends on the shell's radius, the consequence being a transition from onion to whirligig texture with increased radius. In addition, the equilibrium magnetization states are shown. Adapted from SLOIKA.[SSK17]

Reaching further from magnetic caps (half spheres) to hollow spheres, different options for magnetic textures were investigated. In the case of easy-surface anisotropy, either the same or opposing vortex polarity combinations at the poles of a spherical magnetic nanoshell are possible, thus, leading to so-called whirligig and onion configurations, while the latter only occurs for opposite polarities.[KSS12] Here, the declination angle Φ describes the magnetization's slope with respect to the longitude/meridian between an inward- and an outward-facing vortex ($p_1 = -1$ to $p_2 = 1$) on the sphere. Depending on the thickness and the radius of a spherical ferromagnetic nanoshell, Φ varies between $0°$ in the onion case and $90°$, which is shown in the simulated data provided by SLOIKA *et al.* in Figure 2.5.[SSK17]

2.4 Janus Particles

A prominent example for the above discussed curved magnetic textures are spherical magnetic half shells like ferromagnetic caps deposited on top of spherical templates, for which the term Janus particles (JPs) is used. Generally, the prefix for these miniaturized building blocks originates from the Roman god 'Janus' who is the god of beginnings, transitions, and endings. Janus is often depicted with two faces that enable him to look to the past and the future at the same time. The name first came up in 1988, when CASAGRANDE published the fabrication of glass particles that had different hydrophobicity on their hemispheres and were emphasized as a mesoscopic version of surfactant molecules by DE GENNES, when he gave his Nobel lecture in 1992.[De 92] Nowadays, the expanded definition of Janus particles includes any particle that owns two or more regions, which vary in their properties, such as electrical, optical, chemical, or magnetic properties. Often the functionality is introduced via metal vapor deposition, namely electron-beam physical vapor deposition or sputter deposition. A major factor that always has to be considered when dealing with deposited thin films on curved templates like spheres is the induced thickness gradient,

that might affect, e.g., the strength of the implemented property. In particular, this means that the film thickness of the half shell deposited on a spherical template has a nominal value at the highest point and decreases towards the equator. A second aspect is that during the deposition process grains generated within the equatorial region possess a tilted growth direction and, hereby, a reduced grain size. This is expected to play a role for the introduced property and especially in case of thin film systems, where the radially dependent growth process might lead to intermixing between the individual layers.

Due to the importance in context of this work, current research from literature regarding magnetic JPs will be presented in the following.

2.4.1   Magnetic Janus Particles

A lot of experimental effort was invested to studies on easy-surface anisotropy JPs using the example of soft magnetic permalloy ($Ni_{81}Fe_{19}$) caps on non-magnetic spheres in different sizes, among others by STREUBEL *et al.*. A common technique to reveal the magnetic texture of a cap is x-ray magnetic circular dichroism photoelectron emission microscopy (XMCD-PEEM), which was already explored for the characterization of magnetic JPs. To spatially resolve the magnetization pattern, the technique exploits the proportionality between the number of emitted photoelectrons and x-ray absorption at an energy characteristic for the investigated material as well as the magnetization-dependence of the absorption of a circular polarized x-ray beam.[SFK16] Different absorption cross sections of left and right circular polarized beams at wavelengths specific for the absorptions in a certain material, e.g. Co, are used to distinguish between the parallel and antiparallel magnetization components with respect to the propagation direction of the incident electromagnetic wave. By means of this, vortices on a curvature can be identified as quadrupole-like patterns in the XMCD-PEEM contrast and this data was allocated to the simulated phase diagram of individual permalloy caps as shown in Figure 2.6.[SKS12] In addition to investigations on individual caps, STREUBEL *et al.* could also show that two spheres in contact possess alternating vortex chirality due to magnetostatic interaction, correspondingly resulting in chirality frustration in an arrangement of close-packed caps.[SMK12] Although this vortex circulation coupling is present, it was described that the adjacent caps do not promote a polarity coupling, since the vortices in an array showed evenly distributed polarity in the charge contrast of magnetic force microscopy images.[SKR16] With the absence of polarity-chirality coupling as a result, the aforementioned occurrence of DMI in curved samples cannot be approved in the specific case of caps in an array. In addition, it was demonstrated that the onion phase is extended towards larger cap diameters in close-packed formations, because of the magnetostatic interaction during the vortex nucleation in the transition from saturation to remanence. The phase diagrams of both close-packed and individual soft magnetic caps simulated under consideration of a thickness gradient from the particles' pole to their equator are presented in Figure 2.6.

Besides the so far described easy-normal textures in magnetic half shells, out-of-plane magnetized caps were fabricated and intensively studied, too. Typical out-of-plane easy-axis systems like $[Co/Pd]_N$ multilayers were deposited on polymeric beads that were previously arranged in a monolayer (hexagonal packed). The authors stated, that the central area of the cap can be assumed as a single domain, where the Co/Pd layers can be well distinguished. In contrast, the
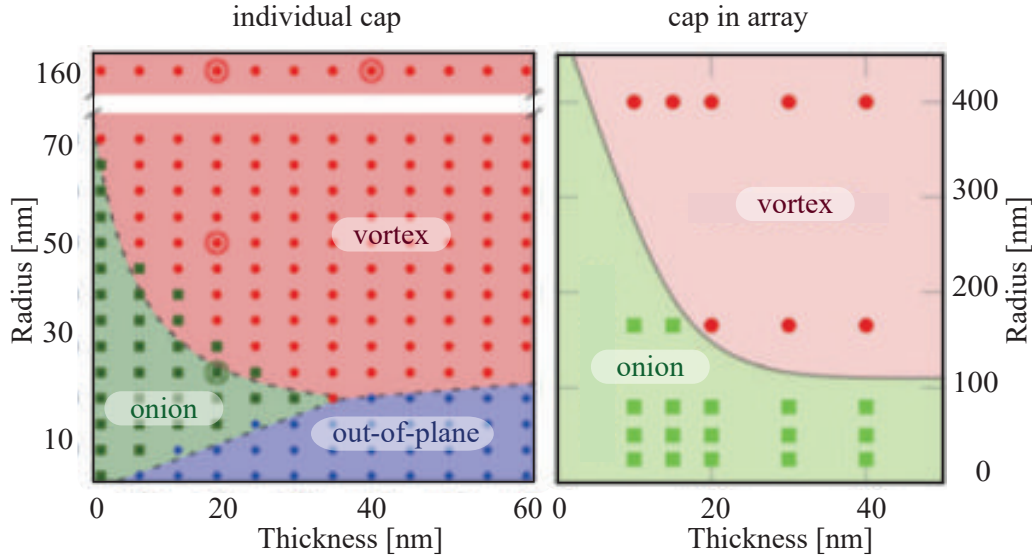
Figure 2.6: Phase diagrams of different possible magnetic textures within permalloy half spheres as a function of cap thickness and radius. Note the different scale of the coordinate axes in the left image for individual caps and the right one for a cap situated in a close-packed array. While the data points for the assembled caps arise from PEEM experiments, the data points for an individual cap were obtained from simulation results. Additionally, experimental results are included by the double circles and the dashed line indicates the simulated phase boundaries for individual planar discs. Adapted from STREUBEL *et al.*[SKS12,SMK12]

the intersection between the spheres has a granular mixture of both materials resulting in a paramagnetic behavior responsible for an exchange decoupling of the individual caps.[KKP10]

Apart from the aforementioned systems with strictly in-plane or out-of-plane magnetization, also systems that change their anisotropy direction depending on the shape were studied. AMALADASS *et al.* were able to experimentally show dramatic changes in the effective magnetic anisotropy of typically in-plane magnetized Fe/Gd multilayers sputter-deposited on an array of nanospheres. Confirming calculations of the demagnetization energy for the system saturated to the out-of-plane magnetized state revealed why the so-called spin reorientation transition (SRT) occurs for the layer system if it possesses a cap-like geometry. This behavior is due to stray field energy minimization: compared to a disc with saturated out-of-plane magnetization, a spherical half shell of the same size and composition creates far less uncompensated charges for the saturated state in which the magnetization points perpendicular to the equatorial plane.[ALS10] These findings are in agreement with the depicted out-of-plane phase occurring for small radii in Figure 2.6 and is therefore an important aspect when considering the magnetic behavior of half-shell geometries.

2.4.2 Introduction of EB to Janus Particles

The so far presented research on JPs mainly focused on solely using ferromagnetic capping materials. Therefore, the aim of this work is to introduce exchange bias thin films with in-plane anisotropy as a novel cap material for magnetic JPs of spherical shape. These objects can

be expected to offer a versatile and precise tuning of the magnetization states within the cap, especially for in-plane onion states and out-of-plane easy-axis systems since the additional unidirectional anisotropy can be implemented to energetically stabilize certainly chosen magnetization directions. Especially the thickness dependence of the exchange bias discussed in subsection 2.1.3 needs to be taken into account when dealing with this special kind of JP. Some of the very few examples yet present in literature are displayed in the following.

Using sputter-deposited permalloy as a soft magnetic material in combination with NiO, ZHANG *et al.* fabricated an array of in-plane magnetized JPs from polystyrene beads with a diameter of 200 nm, whereby isolated magnetic caps were expected, as the thickness of the bilayer was chosen to be much smaller than the radius of the spheres so that exchange interactions and dipolar interactions between the magnetic caps are limited.[ZWM09] By means of vibrating sample magnetometry, the group observed a symmetric hysteresis loop of the nanostructured EB film on top of the spheres that showed a nearly doubled exchange bias field in comparison to the flat bilayer system and a broad switching field distribution, which was attributed to inhomogeneities in the underlying colloidal array. After proving that the increased H_{EB} did not originate from the nanodots, that are created during deposition as a shadow effect and remain on the substrate after harvesting the spheres,[ZWM09,KKC04] the investigation was considered to be a consequence of the thickness gradient present on the cap.[ZWM09] The reduced ferromagnetic layer thickness in the equatorial region was approximated via $t(\theta) = t_0 \cdot \sin(\theta)$, where t_0 is the top thickness of the cap and θ is the angle with respect to the sample plane,[ZWM09] which is in correlation to the $1/t$ dependence of the EB field described in Equation 2.1.4.

Studies on perpendicular exchange bias multilayers on top of nanosphere arrays of the same group revealed changes in the structured film's hysteresis for a variation of the spheres' size. Minimizing their diameter entailed broader switching field distributions and higher coercivity, which was attributed to dipole-dipole interactions, since the caps are expected to be exchange decoupled,[ZLL12]. The observed effects could as well be related to the crystal growth and the grain size distribution that is possibly being influenced by the curvature which is increased for a smaller sphere diameter. Since the array showed an overall hexagonal symmetry except for regions with irregularities, each sphere can be assumed to be surrounded by six nearest neighbors that magnetostatically interact via their stray fields.[ZLL12] During magnetization reversal the magnetic moment of the first cap is switched at a lower magnitude of the external magnetic field than for the isolated cap due to the contribution of the neighbors' stray fields which is visualized in Figure 2.7. On the other hand, the last cap's initial magnetization state is stabilized by the reversed dipoles in its vicinity causing comparatively increased switching field magnitudes.[ZLL12] The result is a sheared hysteresis due to this switching field distribution by the twelvefold demagnetization field of an individual cap. These results prove that at least for out-of-plane magnetized JPs in an array the dipolar fields of the neighboring beads cannot be neglected as it has been done before[ZWM09] but rather influences the magnetization reversal behavior of the structured film.[ZLL12] Additionally, ZHANG *et al.* could support the expectations and findings from previous work proposing a decoupling of the close-packed JPs in terms of exchange interaction due to the small interconnection sites and the short range character of
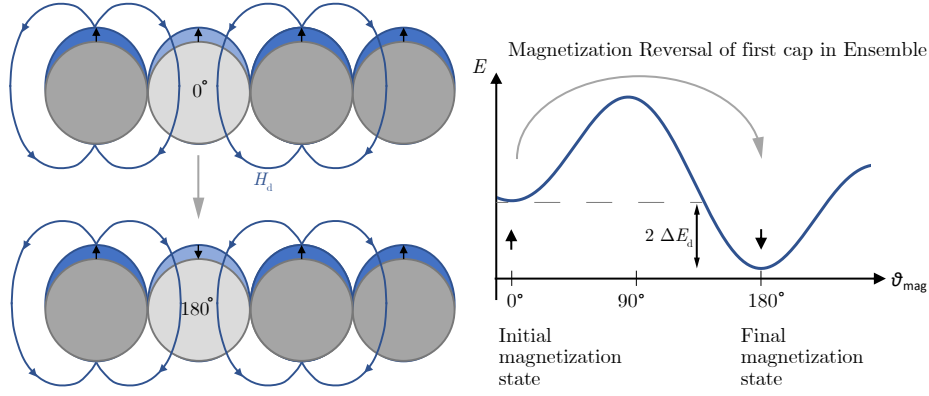
Figure 2.7: Schematic representation of the stray fields created by the neighbors of an out-of-plane magnetized half-shell (light gray) assuming a homogeneously magnetized row of caps. The cap's energy in dependence of its magnetization angle with respect to the other caps is shown by further assuming that this cap is the first to be switched during hysteresis. While a cap in a close-packed monolayer is surrounded by six neighboring JPs, this would result in a reduction of the switching field magnitude by $6\Delta H_{\mathrm{d}}$ Here only two neighbors are taken into account, causing in a switching field magnitude reduced by $2\Delta H_{\mathrm{d}}$. Based on this influence of the dipolar fields the hysteresis curves of magnetic Janus particles with out-of-plane anisotropy is broadened. However, the influence can be expected to be more complex when considering a rather simultaneous switching of the caps.

this type of interaction.[KKP10,AHG05,SMK12,SKR16] As a reason for the increased coercivity it is named that the predetermined shape of the cap constricts the formation of the AF's domain walls, i.e. its granular structure, since a shift in the grain size distribution of polycrystalline samples to smaller grain volumes enhances H_{C}. The domain motion is strongly restricted by the local barriers of the spherical geometry.[ZLL12]

Also for these out-of-plane magnetized caps the increasing exchange bias effect was attributed to the fabrication induced thickness gradient of the layer system and the $1/t$ dependence of H_{EB}. Additionally, it was stated that H_{EB} increases with the decrease of the particle size with a strong increase below $60\,\mathrm{nm}$. This is ascribed to the enhanced ratio between layer thickness and sphere diameter that causes the formation of interconnections and, hence, allows for exchange coupling, which is assumed to be negligible for larger spheres.[ZLL12] However, the magnetic behavior of the investigated exchange-biased particles is still not fully understood and a combination of several reasons could be responsible for the observed effects which emphasizes the necessity of further research in this field.

2.5   Transport of Magnetic Particles

The variety of magnetic colloids has increased during the last decades in which different kinds of particles reaching from the nano- to the micrometer-scale with different properties and origins of magnetic behavior were fabricated and implemented in applications. Up to now, mostly superparamagnetic particles have been of interest in transport experiments, but recently also Janus particles have been addressed in microfluidic environments.[YSG16] In general, several techniques for a directed movement of magnetic particles have been presented, starting from classical

magnetophoresis describing the translational movement of magnetic particles in a magnetic gradient field,[LLB07] to more sophisticated transport concepts applying artificial microscopic stray fields arising from a magnetically structured substrate and temporally shaped external fields inducing a periodical transformation of the particles' energy landscape.[HKB15] In addition, approaches in which the rotational degrees of freedom of Janus particles can be specifically addressed were performed to extend beyond solely translational transport concepts.[BAM05,YBB12]

2.5.1   Acting Forces

Starting with a particle in a liquid environment it is first of all exposed to the interplay of gravity F_G and buoyancy F_B for which three regimes are possible: the particle will either sink ($F_G > F_B$), move upwards ($F_G < F_B$) or hover at the given height ($F_G = F_B$). When extending the experiment to any of the above mentioned experimental approaches with magnetic particles, several forces have to be considered to quantitatively model the motion characteristics of the particles surrounded by a microfluidic environment. The presence of a substrate as well as other particles in proximity of the regarded particle adds surface forces to the picture, like electrostatic and van-der-Waals forces. Furthermore, the particle can be exposed to the magnetic field gradients of either static or dynamically changing magnetic field landscapes in order to actuate it in a controlled manner. In general, this causes the magnetic particle in a viscous environment to experience a balance of forces between magnetic and viscous forces as well as surface forces, gravity and buoyancy. However, the two latter are often neglected, because their contributions are of minor importance, due to the increased surface-to-volume ratio for particles with micrometer-sized dimensions.[WSFX05] The consideration of surface forces becomes important for the particle's interaction with the substrate: they can either be adsorbed or repelled from the substrate surface and by adjusting these forces the particle substrate distance can be tuned. Furthermore, interparticulary electrostatic and van-der-Waals forces play a role in the agglomeration of particles to larger ensembles and can be tuned to prevent this clustering. For the description of the translational movement itself, mainly the magnetostatic force $F_{M,x}$ along a particle's movement direction and the opposing drag force F_D need to be taken into account,[WSFX05] while a steady-state velocity can be derived from balancing them.[HKB15]

To further take into account for rotational movement behavior, it is required to consider the magnetic torques, that are acting on the particles, which will be shown in more detail in section 5.4 for Janus particles.

Starting with the **magnetostatic force**

$$\vec{F}_M = \mu_0 \left(\vec{m}(H_{ex}) \cdot \vec{\nabla}\right)\vec{H}_{ex} \tag{2.5.1}$$

exerted by an inhomogeneous external magnetic field $\vec{H}_{ex}$, the magnetic moment of the particle $\vec{m}$ has to be known. In case of superparamagnetic particles (SPP) for which the magnetic susceptibility $\chi = \mathrm{d}m/\mathrm{d}H$ can be assumed to be constant for small external fields, the magnetic moment can be approximated by $\vec{m}_{SPP} = \bar{\chi} \cdot V_{SPP} \cdot \vec{H}_{ex}$, where $\bar{\chi} = 3\chi/(\chi + 3)$ is the shape corrected susceptibility of a sphere and V_{SPP} its volume.[EMS16] In most experiments the magnetic

fields do not reach the critical value above which the magnetic moment's dependence on the magnetic field becomes nonlinear.

If Janus particles with a ferromagnetic or an exchange-biased cap are used instead of SPPs, the maximum magnetic moment can be written as $\vec{m}_{\mathrm{JP,max}} = M_{\mathrm{s}} \cdot V_{\mathrm{F,cap}}$ with the saturation magnetization M_{s} of the ferromagnetic layer and its volume $V_{\mathrm{F,cap}}$ in the cap. Exemplary, the saturation magnetization of the ferromagnetic material used for the exchange-biased JPs in this work is $M_{\mathrm{s}}(\mathrm{Co_{70}Fe_{30}}) = 1.23 \cdot 10^{6}\,\mathrm{A/m}$.[HGM17] Assuming that the hysteresis of the JP shows a high coercivity and comparably steep slopes for the magnetization reversal, the remanent magnetization of the particle can be assumed to be close to the saturated state. Due to this, the dependence on the external magnetic field strength is rather small compared to the aforementioned linear behavior the case of SPPs.

The magnetostatic interaction between two spheres can furthermore be described similarly to Equation 2.5.1 with $\vec{H}_{\mathrm{ex}}$ being the magnetic field generated by the second particle. SPPs possess magnetic moments that are aligned parallel with the external field so that the only net force amongst individual SPPs occurs, when they are aligned with the magnetic field lines is attractive, thus, creating agglomerated chains. On the other hand, JPs possess a remanent magnetization in the absence of an external field and can therefore interact with each, even when randomly oriented. For this, the **magnetostatic force between two particles** with identical magnetic moments $|\vec{m}_1| = |\vec{m}_2|$ can be approximated by the negative gradient of the magnetic dipole interaction energy (Equation 2.1.1) in point-dipole approximation:

$$F_{\mathrm{M}} = \frac{3\mu_0 m^2}{|\vec{r}|^4}\,(3\,\cos(\alpha)\,\cos(\beta) \,-\, \cos(\beta - \alpha)), \tag{2.5.2}$$

where $\vec{r}$ is the distance vector between the spheres and α, β are the angles between this vector and the magnetic moments $\vec{m}_1$ and $\vec{m}_2$, respectively. The inverse distance dependence to the power of four already shows the strong effect of magnetostatic interactions between particles with a permanent magnetization for short distances.

In laminar fluid flows with low Reynolds numbers, the particle is furthermore subjected to a **drag force**

$$\vec{F}_{\mathrm{D}} = -6\,\pi\eta\,R \cdot \vec{v} \cdot f_{\mathrm{D}}(z) \tag{2.5.3}$$

that depends on the particle's hydrodynamic radius R and its velocity $\vec{v}$ in a viscous fluid with the dynamic viscosity η. Here, f_{D} denotes the drag coefficient that depends on the distance z separating the moving spherical object and a wall in its vicinity, e.g., the substrate surface.[WSFX05] It is equal to one for distances exceeding 10 μm for a sphere of $R = 1$ μm and reaches a maximum value of $f_{\mathrm{D}} = 3$ for an infinitely small distance.[Hol15]

Proceeding with the surface forces, the electrostatic interaction between the particles and a microfluidic chamber wall as well as between the particles can be either described by attractive or repulsive Coulomb interaction. The particles in aqueous suspension with a certain electrolyte concentration possess a surface charge due to the absorption of ions from and/or dissociation of surface groups in the liquid medium. Oppositely charged and solvated ions electrically screen (damp) this surface charge forming the so-called diffuse electrical double layer, which separated
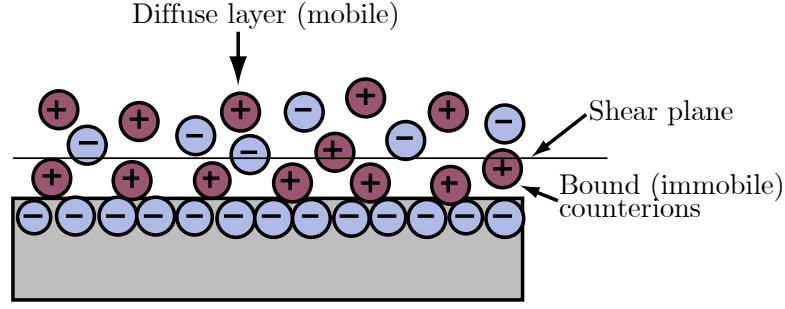
Figure 2.8: The shear plane of the electric double layer as the location of the ζ-potential is indicated between the layer of essentially bound ions and the diffuse layer. Adapted from[Mye99].

from the particle's surface via a layer of immobile ions as it is shown in Figure 2.8. The so-called ζ-potential is the effective surface potential present at the slipping or shear plane, which is the plane that separates the immobilized fluid layer from the mobile diffuse layer.[BGK03] Under the practical assumption of an electrical potential $\Psi(z) = \Psi_0 \exp(-\kappa z)$ exponentially decaying from the surface,[Mye99] the **electrostatic force** between two spheres separated by a distance z of which both posses an electric double layer and an associated potential Ψ_i can be described by:

$$\vec{F}_{\text{el}} = \frac{2\pi \cdot \epsilon \cdot R \cdot \kappa}{1 - \exp(-2\kappa z)} \cdot [2\Psi_{0,1}\Psi_{0,2}\exp(-\kappa z)$$
$$- (\Psi_{0,1}^2 + \Psi_{0,2}^2) \cdot \exp(-2\kappa z)] \cdot \vec{e}_z. \tag{2.5.4}$$

In Equation 2.5.4 constant surface potentials are assumed which allows for the use of ζ-potentials for the particles and the substrate. Here, $\epsilon = \epsilon_0\epsilon_{\text{r}}$ is the permittivity of the medium and κ the Debye-Hückel inverse double-layer thickness as a measure for the attenuation of the electric potential, that depends on the ionic strength I of the electrolyte solution ($\kappa \propto \sqrt{I}$).[WSFX05] If both surfaces show a negative ζ-potential, as it is the case for the Janus particles' spherical body, for the capping layer of the deposited layer system and also for the used substrate in the microfluidic experiments carried out in this work the electrostatic force is repulsive. In the case of carboxyl-functionalized silica spheres ($R =500\,\text{nm}$ $\zeta =-32\,\text{mV}$) the electrostatic force is in the range of 20 and $0.1\,\text{pN}$ for distances between $1\,\text{nm}$ and $600\,\text{nm}$.

Besides the electrostatic interaction, the **Van-der-Waals force** between two objects 1 and 2 in a medium 3 originates from the interaction of dipoles and/or induced dipoles on the objects' surfaces. The energy can be calculated from the contribution of all dipoles for any kind of geometry. The overall Van-der-Waals force between two spheres with radii R_1 and R_2 in dependence of their distance $|\vec{r}|$ is given by

$$\vec{F}_{\text{VdW}} = -\frac{A_{123}}{6|\vec{r}|^2} \left(\frac{R_1 R_2}{R_1 + R_2}\right) \cdot \frac{\vec{r}}{|\vec{r}|}. \tag{2.5.5}$$

In case of two identical particles the expression can be further simplified to:

$$\vec{F}_{\text{VdW}} = -\frac{A_{123} \cdot R}{12|\vec{r}|^2} \cdot \frac{\vec{r}}{|\vec{r}|}. \tag{2.5.6}$$

Here, A_{123} is the so-called Hamaker constant, which is a measure for the interaction energy which depends on the materials 1 and 2, of which the objects consist, and on the surrounding medium 3.[BGK03] The Hamaker constant of the overall system A_{123} can be approximated by using the individual Hamaker constants A_{ii} in vacuum via $(\sqrt{A_{11}} - \sqrt{A_{33}})(\sqrt{A_{22}} - \sqrt{A_{33}})$.[Isr11] For distances above $5\,\mathrm{nm}$ retardation effects have to be considered, which can be included by the following correction:

$$A_{123,\mathrm{ret}} = A_{123} \cdot \frac{1}{1 + p \cdot |\vec{r}| \cdot \lambda_{\mathrm{ret}}}, \tag{2.5.7}$$

where λ_{ret} is the retardation length often assumed to be $100\,\mathrm{nm}$, since it is approximated as the characteristic wavelength of the electromagnetic interaction mediating the van-der-Waals interaction.[Gre81] The factor p is set to 5.3 for flat surfaces, to 11 for spherical surfaces and to 14 for the interaction between a sphere and a wall.[Isr11] As an example, the Van-der-Waals force between two JPs ($r = 500\,\mathrm{nm}$, $A_{123} = 3.9 \times 10^{-21}\,\mathrm{J}$) can be estimated to be within the range of $300\,\mathrm{pN}$ and $2\,\mathrm{fN}$ for distances between $1\,\mathrm{nm}$ and $100\,\mathrm{nm}$, respectively.

2.5.2   Janus Particles in Microfluidics - *state of the art*

The next step towards the applications of Janus particles is to approach their dynamic behavior within microfluidic experiments, in which the magnetic addressability of the different degrees of motion is investigated. Once the characteristics of transport and rotation are well understood, Janus particles may serve as microprobes for e.g. analyzing rheological properties of liquid samples,[BAM05] as actuators in micromixing devices[YHH10] and in sensing applications.[YSG16] Some experimental approaches of magnetic JPs in microfluidic environment from which the magnetic controllability of different degrees of motion can be studied will be presented in the following.

A very early strategy for a so-called rotational nanoviscosimeter was presented by BEHREND *et al.* and uses fluorescent non-magnetic particles, that are metal-capped on one hemisphere in order to break the optical symmetry. The blinking of these modulated optical nanoprobes (*MOONs*) in fluorescence microscopy was used as an indicator for the rotation of the spheres and could thereby be related to browninan motion. These non-magnetic blinking Brownian MOONs undergoing rotational diffusion were compared to so-called *MagMOONs* with ferromagnetic content, that were rotated by means of an above rotated permanent magnet, with the aim of studying microscopic viscous forces and torques. From the relative fluorescence intensity the rotation rate was evaluated for rotational frequencies above $1\,\mathrm{Hz}$ at unknown magnetic field strength. The observations showed a rotation rate which was reduced with respect to the driving frequency accompanied by a rocking motion at this frequency.[BAM05]

Apart from magnetic beads capped with non-magnetic metals, also spherical hydrogel (i.e., hydrated hydrophilic polymer networks) particles have been presented by YUET *et al.*, that contain magnetic material within the whole hemisphere. Employing a technique, called *direct monodispere droplet formation*, in a microfluidic channel structure and subsequent UV irradiation microparticles are formed. Supplying two co-flowing prepolymeric mixtures of which one contains
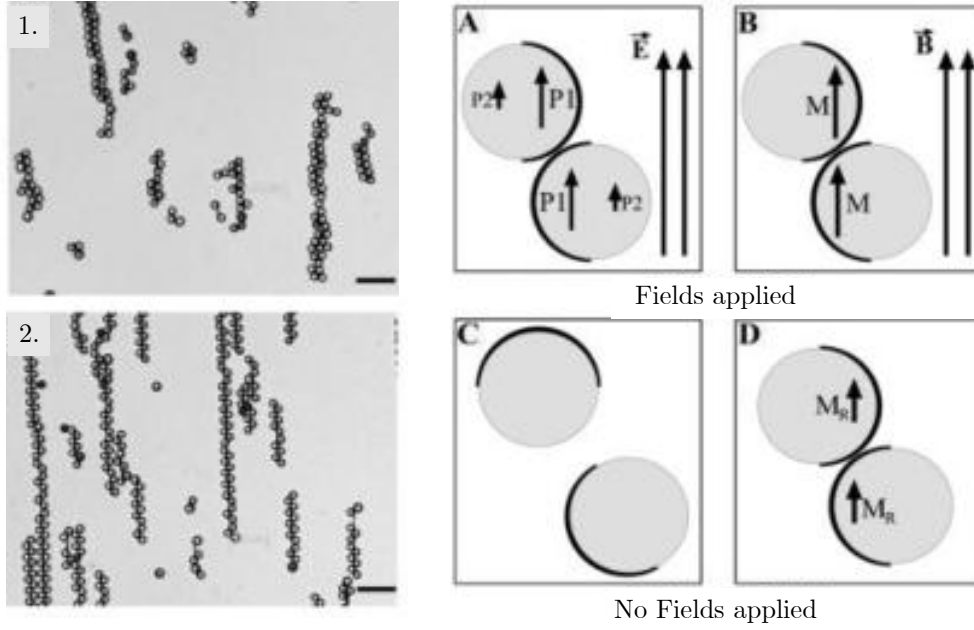
Figure 2.9: 1. Double chain and 2. staggered chain formations of ferromagnetically capped polystyrene particles exposed to electric or magnetic fields. The right scope shows the effect of either an alternating electric (A) or a magnetic field (B) on the assembly of the spheres. While the polarization P within the particles is not permanent when the electric field is removed (C), a remanent magnetization M_R remains within the JPs after the removal of the magnetic field (D). Therefore, the chains induced by a magnetic field are permanent. Taken from [SGM09]

magnetic material and the other does not, microparticles with one superparamagnetic hemisphere were fabricated and afterwards individually rotated by in-plane rotational fields, where a chain like assembly could be observed for flux densities of $14\,\mu\mathrm{T}$.[YHH10]

However, except some examples including the previous, the most widely investigated type of magnetic JPs remains that of non-magnetic spherical objects covered with a magnetic material on one hemisphere as previously described in subsection 2.4.1 and subsection 2.4.2. The following examples of magnetic JPs in microfluidic experiments refer to these kind of magnetically capped particles.

The before mentioned assembly of magnetic JPs in chains was furthermore investigated in the presence of magnetic as well as electric fields.[RRS12,SGM09] For this purpose, an experimental cell with gold electrodes deposited on the substrate for applying AC electric fields containing the aqueous suspension of JPs (cap from deposition of Fe) was used. The investigations revealed the formation of staggered as well as double chains of the spheres that were generated upon the application of either a magnetic ($150\,\mathrm{mT}$) or an alternating electric field ($400\,\mathrm{kHz}$ and $25\,\mathrm{V}$) with the caps in adjacent positions as shown in Figure 2.9.[SGM09] Since the caps keep their remanent magnetization, the chains were remained after removing the magnetic field. These permanent structures were shown to be disassembled by remote demagnetization which corresponds to an alternating ($60\,\mathrm{Hz}$) magnetic field while gradually decreasing the field strength. Contrastingly,

a)

b) precession of single JP

c) JPs forming a
    hexagonal sheet
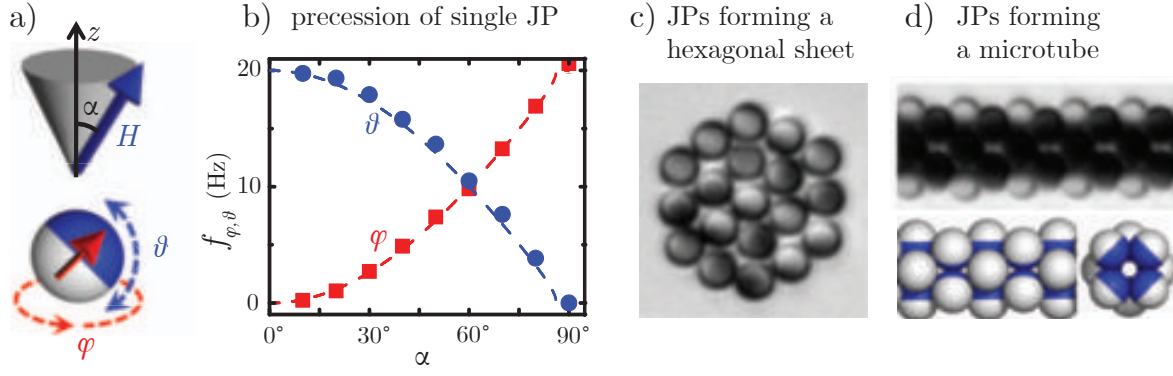
d) JPs forming
    a microtube

Figure 2.10: a) Sketch of Yan and coworkers' experimental geometry for ferromagnetically coated $3\,\mu m$ JPs: the rotation of the Janus director (red, angle φ) around the precession axis z is accompanied by a perpendicular oscillatory movement (angle ϑ) in a precessing field H with a precession angle α. b) Measured frequencies of the rotational and oscillatory movement vs. the field's precession angle. c) and d) Self-assembly geometries of a planar sheet for larger precession angles and of microtubes for smaller precession angles, respectively. Adapted from Yan *et al.*.[YBB12]

the JP assemblies induced by an electric field were observed to break up after the removal of the field, since the interaction was mediated by the polarization of the metallic caps that cannot be retained by the caps in the absence of the field as illustrated in Figure 2.9.[SGM09] The type of assembly structure built by the spheres was furthermore connected to the extend of iron oxidation during the deposition process. Depending on the stoichiometry of iron and oxygen within the cap it becomes either ferro-, ferri- or antiferromagnetic, which results in staggered chains, double chains or no assembly, respectively.[RRS12]

Aiming to understand basic principles in self-assembly processes, that are usually only investigated for equilibrium systems, Yan *et al.* observed a dynamic system of JPs in precessing magnetic fields ($\approx 5\,\mathrm{mT}$) and related their findings to the particles' motion synchronization. For single ferromagnetically capped silica beads ($3\,\mu m$) a simultaneous rotation around the precession axis z (angle φ in Figure 2.10) and a perpendicular oscillation (angle ϑ) were measured. A rotational in-plane magnetic field ($\varphi = 0°$) resulted in strictly rotational movement of the beads at the driving field frequency without any perpendicular oscillation. On the other hand, comparatively small precession angles resulted in a solely rocking of the JPs at that frequency. Furthermore it was observed that ensembles of these JPs exhibit different self-assembly geometries depending on the external field frequency and the angle of the magnetic field towards its precession axis (α). Here, planar hexagonal sheets of JPs were imaged for almost in-plane rotating magnetic fields ($\alpha = 70°$ to $90°$), whereas zigzag chains and microtubes were formed at smaller angles α. For all the microtubes, that posses polygonal cross sections with three to five edges, the metallic caps of the JPs were found to face inward speaking for their synchronization induced stability.[YBB12]

A promising biological application of JPs seems to be the remote control of activating T cells, which are part of the adaptive immune system and accomplish central tasks in cell-mediated immunity. Certainly, their controlled activation, upon which a recognition of cancer cells can

be achieved, offers an approach for *in vivo* cancer treatment based on the patient's own T cells.[LYY16] LEE *et al.* designed JPs, of which one hemisphere was Ni coated and thereby magnetic and the other one was functionalized with antibodies for T cell stimulation. These can be translocated in magnetic gradient fields to approach the T cells and subsequently rotated in order to bring the antibody bound hemisphere in contact with the cell, upon which the T cell is activated.

Combining the degrees of freedom accessible for Janus particles with a novel transport concept based on the dynamic alteration of the particle's magnetic potential energy landscape results in motion characteristics previously studied by R. HUHNSTOCK within this group.[Huh17] A topographically flat EB substrate, modified to possess an artificial magnetic domain pattern of parallel stripes in head-to-head and tail-to-tail configuration, creates a periodically structured microscopic stray field distribution and therefore a potential energy landscape for the above located magnetic particles in microfluidic environment with minima at the positions of the domain walls, i.e., the stray field sources.[HKB15] This energy landscape can be varied upon the superposition of the substrate's magnetic field landscape (MFL) with an temporally shaped external magnetic field. The first of these trapezoidal magnetic field sequences is applied parallel to the sample surface normal (H_z) and the second one is applied along the short stripe axis of the domain pattern (H_x). The combination of both magnetic field components with a defined phase shift leads to a periodic shift of the particles' energetic minima. Thus, a directed and step wise transport of the magnetic beads from one domain wall to its neighboring domain wall is achieved.[HKB15] In case of SPPs, only a translocation was observed, since the homogenous appearance of SPPs does not allow to optically distinguish between different particle orientations in space. In contrast, the investigations on exchange-biased JPs in this transport system showed a combination of translation and rotation of the capped magnetic beads. The reorientation of the effective magnetic field during the application of the pulsed field sequence leads to a torque which is periodically changing. The torque acting on the magnetic moment of the JPs in their remanent magnetization state exceeds the viscous torque exerted by the surrounding liquid phase and therefore induces the rotational movement.[Huh17]

CHAPTER 3

FABRICATION OF JANUS PARTICLES

The fabrication of the exchange-biased Janus particles (JP) used in the present work will be explained in the following and is schematically shown in Figure 3.1. The process consists of two major steps, namely the self-assembly of non-magnetic spherical microparticles on a substrate and the subsequent deposition of the exchange bias layer system on top of the assembled spheres. The experiments in this work focused on the fabrication of JPs from silica particles with a diameter of 1 and 1.5 μm, whereas a previous work by R. HUHNSTOCK concentrated on 3 μm JPs.
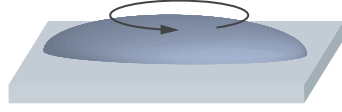
As a note, the terms 'particle' and 'bead' for the used microparticles are used interchangeably throughout this and the following chapters.

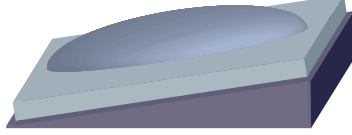## 3.1 Self-Assembly of Spherical Non-Magnetic Particles

Aiming to create a sample on top of which consistent regions of close-packed monolayers of silica particles (1 and 1.5 μm in diameter) are assembled a procedure of two subsequent steps was used. At first, a glass (or in some experiments Si) substrate with an area of $1\,cm^2$ was cleaned with concentrated sulfuric acid for 24 hours to increase the hydrophilic character of the substrate and afterwards stored in ethanol.[MFO95] For the self-assembly process, the aqueous stock suspensions of silica particles were diluted with water and 10 vol% ethanol to a mass concentration of 1.5 mg/ml. To perspectively provide access for biofunctionalization, amorphous silica particles *sicastar*® with a carboxyl termination on the surface were purchased from *micromod Partikeltechnologie GmbH* with a nominal concentration of 50 mg/ml. Subsequently, a drop of 30 μl was placed in the center of a substrate using a microliter pipette. The substrate with the drop containing 1 μm (1.5 μm) beads was then spin coated at a low speed of 120 rpm (90 rpm) for 600 s in order to distribute the particles inside the drop and to avoid the deposition of large agglomerates and multilayers. In a following step the sample was carefully placed and fixed in the center of an evaporation box which was closed and positioned at an angle of 6° and 9° with respect to the horizontal plane for the 1 μm and 1.5 μm particles, respectively. The chosen angles were optimized for the respective particle size to achieve a homogenous coverage of the sample with particles with a high portion of monolayered regions. This technique is often

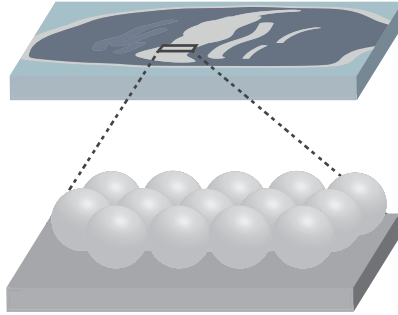1. Self-assembly of silica spheres   2. Sputter deposition

1.a. Slow spin
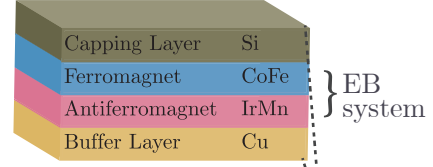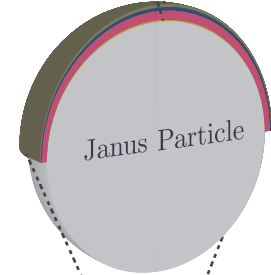   coating

1.b. Tilted
      evaporation

1.c.

2.a.

Capping Layer	Si
Ferromagnet	CoFe
Antiferromagnet	IrMn
Buffer Layer	Cu

} EB
  system

2.b.

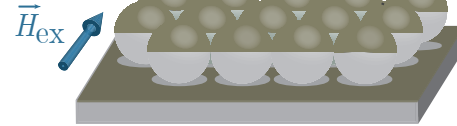Janus Particle

2.c.

$\vec{H}_{ex}$

Figure 3.1: The two-step process for the fabrication of exchange-biased Janus particles and the cross section of the fabricated bead are show: Starting with the self-assembly (1.) procedure, first, the droplet containing the particle suspension is spin coated (1.a). After the evaporation with the sample tilted at a fixed specific angle (1.b) resulted in a submonolayer of hexagonal close-packed silica particles (1.c), the sputter deposition (2.) was performed. The material is deposited on top of the spheres, on the plain substrate and also on the substrate through the interstices of the close-packed array creating the so-called shadow effect (2.b). The depicted cross section of a JP indicates the decreasing cap thickness towards the sphere's equator. Although the ratio of the individual layer thicknesses is imaged correctly, the ratio of sphere to cap is reduced by a factor of 2.5. The deposited thin film system with the included materials is shown on the top right (2.a), whereas the thicknesses of the individual layers are not to scale.

applied for self-assembly processes, especially when nanoparticles are used. Such a procedure allows for a decrease of the evaporation rate due to the fixed atmosphere, which also prevents disturbance from external air flow. The evaporation process starts from the upper edge and proceeds towards the lower edge of the drop resulting in a layer formation in close-packed arrays in the central area and a submonolayered surrounding.[MFO95] Note that a precise temperature control ensuring temperature stability is highly desirable for this method.[MFO95] After the liquid phase was completely evaporated, typically after 4 hours, the sample was analyzed in an optical microscope. The chosen combinatorial approach of slow spin coating and tilted evaporation of the drop containing the silica beads dispersed in a water-ethanol mixture using glass as a substrate was observed to result in consistently arranged monolayer stripes within the overall submonolayer. These regions were also distinguishable by eye and are depicted in Figure 3.2 together with microscopic images. In case that only the static evaporation technique was used,
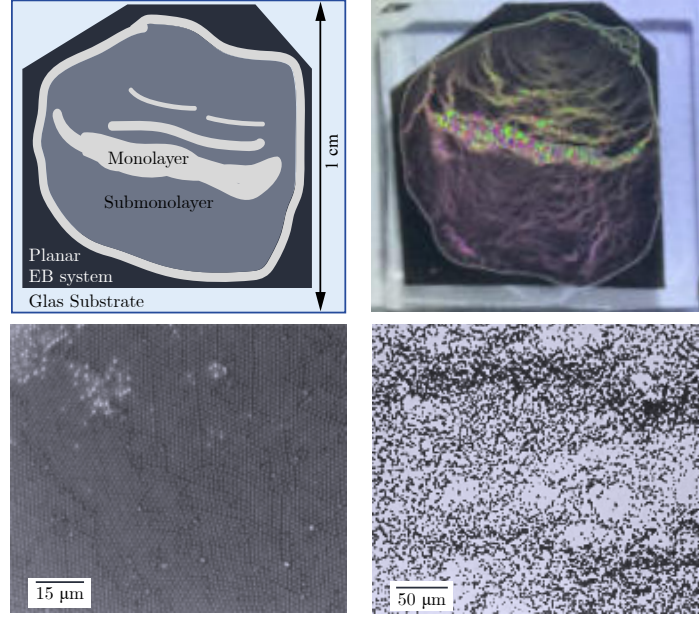
Figure 3.2: Top: A sketch of a typical sample after sputter deposition is shown in comparison to a photograph. Interference effects from the layered regions are visible in the photograph from which the monolayered regions were spotted for further experiments, e.g. for the laser alignment in Kerr magnetometry measurements. The corners of the sample did not contain any particles and were therefore chosen as a planar EB reference region. Bottom: Microscopic images of different magnification form a monolayer (left) and a submonolayer (right) area.

the particles sedimented towards the lower side of the drop due to gravity, creating a large multilayerd edge which could be prevented by the additional spin coating.

3.2   EB Layer Deposition on top of Assembled Particles

In the next step, the intended magnetic properties were introduced to the JPs by the deposition of the nanometer-scaled magnetic thin film caps. For the fabrication of these typically planar thin films, sputter deposition, i.e., a physical vapor deposition technique, is used and this method was also utilized for the JP fabrication. During this process atoms of a target material are ejected due to the transfer of momentum from energetic ions, where typically inert gases like Argon are used. In this respect, the Ar atoms of the gas phase are ionized by applying a high voltage (here in alternating polarity at radio frequency, RF-AC) and therefore, a plasma is created. The charged Ar ions are then accelerated towards the target which is set on negative potential. Due to the collisions on the target's surface, atoms are ejected when their energy exceeds the binding energy of the target. These atoms are then transferred to the gas phase from which a subsequent deposition onto the substrate which is located below the target in the deposition chamber takes place. The now physically adsorbed atoms can undergo diffusion parallel to the substrate's surface until chemisorption happens at an energetically favored position and the atoms are chemically bound to the surface. By this, polycrystalline thin films are formed, since sputter deposition typically does not lead to epitaxial growth.[Ses12]

By means of this sputter deposition technique a four-layered thin film system containing an AF/F bilayer, as shown in Figure 3.1, was deposited on top of the before prepared samples with assembled silica particles in the RF sputter deposition system *Leybold Heraeus Z400*. While the base pressure in the chamber is $p_B = 3 \times 10^{-7}$ mbar, the process was performed at a working pressure of $p_{Ar} = 10^{-2}$ mbar with a Ar flow of 140 sccm after a presputter procedure was executed for every target in order to guarantee stable sputter rates.

The deposited bilayer system contained 30 nm of the antiferromagnet $Ir_{17}Mn_{83}$ and 10 nm of the ferromagnet $Co_{70}Fe_{30}$. Below the EB bilayer, a 5 nm thick Cu buffer layer was deposited which promotes the (111) crystallographic texture for the growth of the AF layer on top. Additionally, the bilayer was covered by an oxidation protective capping layer of Si with a thickness of 10 nm. Due to oxidation processes the capping layer will later on exhibit the same surface charges as the plain silica part of the JP, and thus, electrostatic and Van-der-Waals forces are expected to act on the JP in an isotropic manner. During the deposition process a homogenous magnetic field of $H_{ex} = 28$ kA/m was applied parallel to the substrate surface was applied within the chamber,[Huc17] which induces a uniaxial magnetocrystalline anisotropy axis of the ferromagnet parallel to the direction of this magnetic field and a preferred orientation of the unidirectional anisotropy due to the alignment of the antiferromgnetic grains.[MB56,MB57] The deposition parameters are summarized in Table 3.1. A field cooling procedure to set the AF ordering state was omitted in the fabrication process of JPs, since preparatory experiments revealed thermal instability, i.e., melting of the particles. In these experiments, silica particles on a glass substrate were treated on a hotplate at a temperature of 200 or 300 °C for 30 to 70 min, because the samples are typically heated at 300 °C for 1 hour and subsequently cooled down to room temperature at a rate of 40 °C/min to maximize the EB for comparable planar systems while still avoiding thermal diffusion processes.[Hol15] For the lower temperature it can be seen from microscopic images of the previously heated silica particles that the amorphous particles had started to melt from the edge of the monolayered regions, whereas the higher temperature resulted in a complete melting and subsequent setting of the silica layer as depicted in Figure 3.3.
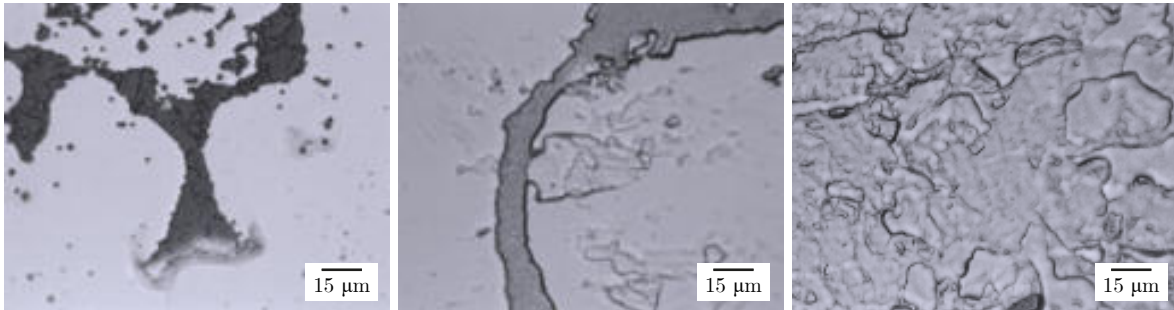

Figure 3.3: Silica particles ($d = 1$ μm) after heating. Left: at 200 °C for 30 min. Center and Right: at 300 °C for 70 min.

Table 3.1: Sputter deposition parameters for the deposition of the EB layer system on top of the assembled microsphere arrays.

Material	Sputter rate [nm/min]	Ar gas flow [sccm]	DC potential [V]
Cu	8.12	140	700
$Ir_{17}Mn_{83}$	4.87	140	600
$Co_{70}Fe_{30}$	3,00	700	700
Si	3.34	140	700

3.3 Harvesting Process

For the execution of microfluidic experiments, the JPs were transferred from their initial substrate to a dispersion, which was either based on pure water or on a glycerol water mixture (50:50 w%). For this purpose a small liquid volume of approximately 7 µl was placed on the sample with a pipette, whose tip was subsequently used to carefully scratch above the area from where the beads were harvested (usually 25 % of the sample area). The volume was taken with the pipette and stored in a small plastic container (*Eppendorf* PCR tube, $V = 200$ µl). The procedure was repeated one or two times in order to collect as many particles as possible. If further repetitions were desired, the particles were collected at the bottom of the tube by a permanent magnet in its vicinity. Then the volume for the repetition of the harvesting process was taken carefully from the top of the liquid in the tube. The JP dispersions were stored in the tubes sealed with *Parafilm*® M and were treated by ultrasonication for 5 to 10 minutes prior to the application to the microfluidic chamber.

4.1 Imaging Techniques

When dealing with objects on the micro- and nanometer scale, imaging becomes a major issue in gaining knowledge about the sample's properties. During the investigations on Janus particles a combination of different techniques leads to a better understanding of their geometry and other characteristics. In this section the applied methods will be presented.

4.1.1 Scanning Electron Microscopy

In classical light microscopy, where optical lenses are used to magnify a microscopic object, the resolution is the minimum distance between the features that are desired to be distinguished as individual points:

$$d = \frac{\lambda}{2 \cdot NA} \tag{4.1.1}$$

It is limited due to the diffraction of light with the wavelength λ and the numerical aperture of the optical system NA. Depending on the refractive index of the used medium n (n_{air} =1.000, n_{oil} =1.515) the numerical aperture can be calculated from:

$$NA = n \cdot \sin(\theta). \tag{4.1.2}$$

Here, θ is the angle of the half cone of incident light that is able to enter or exit the objective lens which is closest to the sample. With visible light and immersion objectives the resolution cannot be pushed below 200 nm. This diffraction limit is due to the point objects being imaged as airy disks arising from the first minima in the so-called point spread function of the intensity distribution behind the optical path.[Kub13]

In electron microscopy, e.g. scanning electron microscopy (SEM), where the source of illumination is changed from light to electrons accelerated via a voltage U_{acc}, the resolution becomes much higher due to the shortening of the used wavelength. It is in this case given via the de Broglie wavelength $\lambda = h \cdot c / E$ with the energy $E = U_{\text{acc}} \cdot e$ of the electron with its elementary charge

e, the speed of light c and Planck's constant h. This non-relativistic calculation, which is valid for acceleration energies below $50\,keV$, does not consider the velocity of the electron leading to a wavelength error for higher acceleration voltages.[RP77] The electron beam has a probe diameter on the sample surface in the range of 1 to $10\,nm$ and carries a current of 1 to $100\,pA$.[Rei85]

The main components of the reflection based SEM are the electron source, which most often uses field emission, the objective and condensor lenses, which are magnetically or electrostatically focusing the beam, a deflection coil unit for scanning the beam and certain detectors. All these elements are arranged in a column in which the background pressure does not exceed $10^{-6}\,mbar$, whereas it is kept below $10^{-9}\,mbar$ at the field emission electron gun.[RP77]

During the imaging process the so-called primary electron (PE) beam is scanned over the area of interest on the sample and interacts with its atoms. The following processes occur: Within the first $10\,nm$ below the surface and close to the focal spot, secondary electrons (SE1, $< 50\,eV$) are created by inelastic scattering. In this case the energy transfer from the primary electron is high enough for the excited electron to overcome the material's work function.[Rei85] From a larger region of the interaction volume (at a depth of $100\,nm$ to $1\,\mu m$) elastically backscattered electrons (BSE) with energies above $50\,eV$ arise.[RP77] If in this case the energy loss is low, the BSE can still generate secondary electrons (SE2) from an area around the focal spot, which is not desired for sharp imaging. Because of the different ways of generation of the detectable particles, SEs and BSEs can be distinguished due to their different energies. A third process of the interaction is the emission of characteristic X-rays which offers the chemical characterization of the investigated features through so-called energy-dispersive X-ray spectroscopy (EDX). In these compositional images the resolution cannot be lower than $1\,\mu m$, because the characteristic X-rays arise from the whole interaction volume around the focal spot.[Was12]

The most often used detectors for SEM are the three following:

- **Everhart-Thornley detector (ETD):** This detector collects the low-energy ($< 50\,eV$) secondary electrons by accelerating them through a positively charged grid ($+100$ to $+200\,V$) onto a scintillator, which luminesces under the impact of the incoming SEs.[RP77] A photomultiplier amplifies the signal and a digital image can be generated from the mapped intensities. Although BSEs can be collected from a small solid angle alongside with the SEs, the BSE signal is substantially smaller then of the SEs, which have low enough energy to be deflected towards the detector.[RP77] The brightness of the image then depends on the amount of SEs collected. The Everhart-Thornley detector is placed to one side of the sample stage, which leads to a three-dimensional appearance. The sidewise positioning dissembles an illumination of the sample from one side causing more electrons to be detected from edges facing the detector than features facing the other direction, thus, leading to the appearance of seeming shadow effects.[Was12]

- **Energy selective backscattered electron detector (EsB):** This detector is sensitive to high-energy electrons that have been backscattered or reflected from the specimen and is located in the column above the objective in a doughnut shape, which causes a small angular distribution of the detected electrons. The heavier the material (higher atomic number),

the larger is the effect of elastic scattering of the primary electrons, which causes more BSE for a brighter appearance of these materials in the image giving the BSE detection the property of material contrast, while there is no topographic information included. In order to exclude SEs from the detection, a filtering grid, which can also be tuned to select BSE from a certain threshold energy, is mounted in front of the detector.[Car16d] Due to a higher signal-to-noise ratio this detection method enables lower lateral resolution than the Everhart-Thornley detector.

- **Inlens SE detector:** This technology in newer generation SEMs offers high resolution of surface and topography information from SEs. Through an implemented so-called beam booster the SEs are accelerated back into the column and focused to the annular Inlens SE detector by the objective lens.[Car16b] Due to the normal incident, there are no shadow effects like in Everhart-Thornley detection but a high contrast of surface features.

For the selection of imaging parameters some compromises are necessary depending on the characteristics of the sample and the properties that are aimed to be visualized. First of all, only the combination of different detection methods allows the operator to gain characteristic and precise information on the specimen's topography as well as composition. An important parameter is the acceleration voltage for the PE beam, which for high voltage leads to an increased resolution but a loss of contrast, because the electrons are scattered more strongly. Furthermore, the working distance has to be chosen and the operator has to consider that small distances eventuate in reduced depth of focus and field of view but in higher efficiencies for the detectors in the column.[Was12] A crucial point in SEM are the conductive properties of the sample itself, where conductive metal samples on the one hand can be easily grounded. On the other hand, when working with isolating samples, the accumulation of charges affects the image quality, as they become visible as bright spots or lines in the image. Here, the integration procedure for the image generation strongly affects this charge built-up. Compared to pointwise integration the charging can be reduced by integrating over the scanning lines or even over the whole image, which on the other hand diminishes the image sharpness. One option to prevent charging is the deposition of a conductive layer by sputtering, which may lead to artefacts and a loss of information. Another possibility is given in environmental SEM (ESEM), where the sample is placed in a chamber with relatively high pressure neutralizing the charges. In this case the column is differentially pumped in order to guarantee the required free mean path of the electrons.[Dan81] Lastly, it has to be kept in mind that a tilt of the sample stage results in changed detector efficiencies and a distortion of the image, which can be corrected afterwards for correct distance measurements.

4.1.2   Helium Ion Microscopy

In order to push the resolution in topographic imaging even further, ion microscopes have been developed, since the higher mass of an ion allows substantially shorter wavelengths and, thus, even fewer restrictions from diffraction.[HNS12] The development of liquid metal ion sources (LMIS) in the 1970s resulted in functional ion microscopes based on a focused gallium ion beam that had a major drawback coming from the ions' high mass, which is in fact five orders of
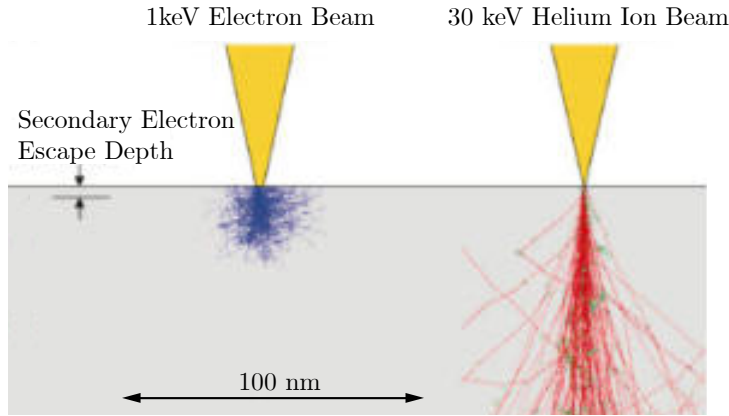
Figure 4.1: Monte-Carlo simulations for representative electron and He+ ion beams into silicon, while the latter shows a narrower interaction volume. Adapted from NOTTE *et al.*.[NWE07]

magnitude larger than of an electron: concurrent to the collection of the microscopic image the area of interest is sputtered to some extent diminishing the resolution. The breakthrough in ion microscopy was then accomplished in 2005 when the gas field ion source (GFIS) was developed for helium as a source gas. Shortly after, the first scanning helium ion microscope (HIM) was commercialized by Carl Zeiss.[HNS12] The source is made of a single crystal metal, which is fabricated in a needle shape, and its atomic structure can be visualized as in classic field ion microscopes. After the insertion to the source chamber the source is modified to possess a pyramidal structure on its apex. This is achieved by raising the extractor voltage up to the point of field evaporation in order to rearrange the atoms in the tip until a trimer structure is visible in the emission pattern.[HNS12] During the imaging process helium gas is applied under a controlled rate close to the needle in the source chamber. The needle is set at high positive voltage, typically between $25\,kV$ and $35\,kV$.[Car16c] The helium atoms in the trimer's vicinity are polarized due to the electric field gradient of the needle and electrons can tunnel from a helium atom into the metal needle leaving positively charged helium ions behind.[NWE07] From the three emerging ion beams originating from the very small trimer area of only a few Å^2 the portion of one single apex atom is guided into the column. These helium ions are accelerated through the ring shaped extractor entering the ion optics which are typically quadrupoles and octopoles.[Car16c] The focused beam is scanned across the sample surface via a deflection unit while the generated SEs are detected with an Everhart-Thornley detector. The important difference between HIM and SEM to mention is the slow diverging of the helium beam beyond the surface as shown in Figure 4.1. In SEM backscattered electrons still have the potential to generate SEs in some distance to the actual focal spot of the incident beam (SE2). These SE2s give information to the image which is not originating from the scanned position and thus causing broader feature edges than in HIM.[NWE07] Another advantage in HIM is the option to use a so-called flood gun. This is an electron gun located on one side of the sample chamber which can be operated to flood the sample surface with electrons in order to compensate the positive charges that are built up during the imaging process. Charging effects that are typically a crucial issue in SEM can be overcome by this technique when dealing with isolating samples.[Car16c] Lastly, HIM offers a large depth of field (5 times higher than in SEM), which is also assigned to the small convergence angle of the beam due to the reduced diffraction.[NWE07]
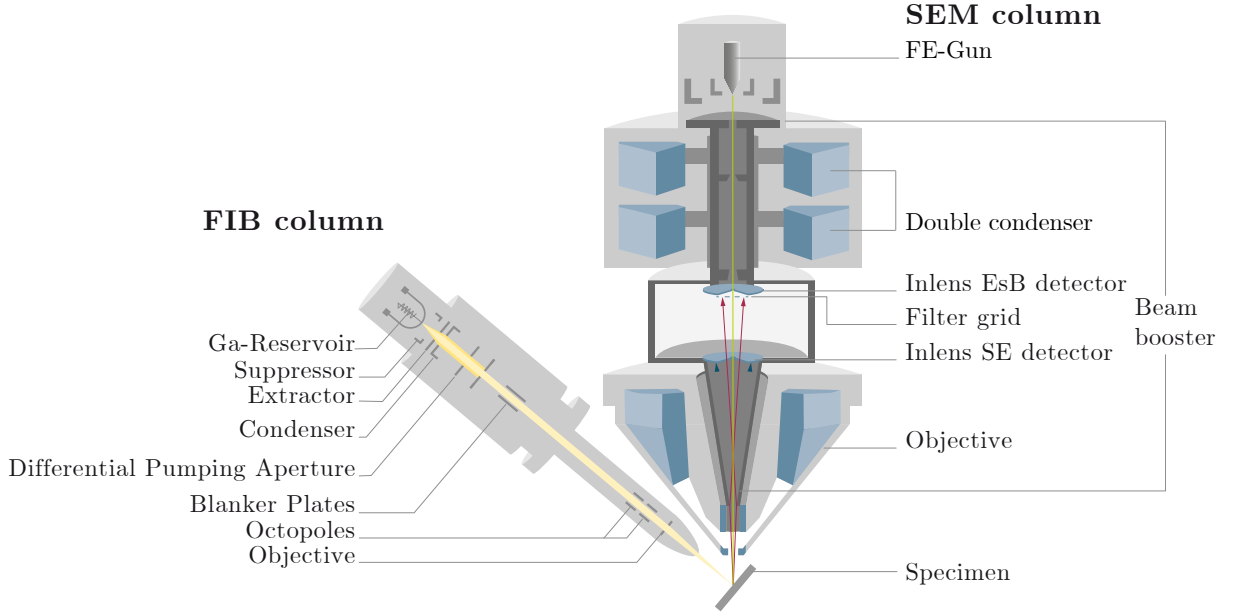
Figure 4.2: Schematic setup of a crossbeam FIB-SEM with one column for electronic imaging and one column for sputtering by Ga$^+$ ions. The ETD and the gas injection needle are located in front of and behind the sketch's plane. Taken from[Car16a].

4.1.3   Focused Ion Beam - Scanning Electron Microscopy

As stated in the prior section (subsection 4.1.2), gallium LMIS was accompanied by sputtering of the sample through the ion beam, which is nowadays taken advantage of for nanomachining in focused ion beam (FIB) applications. This technique combines a LMIS in an ion optics column in order to precisely mill parts of the specimen with a SEM for imaging in a so-called crossbeam geometry. The device can be used to create cross sections of certain sample features or to cut lamellas, which can then be transferred to a transmission electron microscope (TEM), as well as to take tomographic images by cutting and imaging slice by slice. A FIB-SEM setup with two crossbeam columns is shown in Figure 4.2. The main requirement for a precise FIB manipulation is to find the coincidence point for the electron and the ion beam, while the sample stage is tilted to an angle for perpendicular ion beam incidence.[Gia05] A beam blanker is necessary to deflect the beam from the sample preventing its destruction outside of milling times. Furthermore, for the milling of cross sections it is advisable to protect the milling site by beforehand depositing an additional layer. This is feasible in FIB due to the provided gas injection system: precursor gas molecules are adsorbed on the specimen's surface and decompose in the region, where the ion beam strikes. This ion beam assisted chemical vapor deposition assists the built-up of the deposited material, which is usually a metal or an insulator.[Gia05] For the purpose of good contrast a material is chosen where the conductivity differs from the imaged sample feature's conductivity. Afterwards cross section or lamella milling can be performed without damaging the edges, where for this work ion beam currents around 80 pA at 30 keV were chosen for accurate milling and polishing of the JPs.

4.1.4 Scanning Probe Microscopy

The techniques combined under the name scanning probe microscopy are not comparable with optical or electronic imaging, but rather have the mapping of forces between a sharp tip and the investigated sample in common. Their development dates back to the 1980s and to the invention of the scanning tunneling microscope by Binning and Rohrer.[EW14] For the present work atomic and magnetic force microscopy was used in order to reveal the Janus particle's topographic as well as magnetic properties.

Atomic Force Microscopy

Due to its relevance for the experiments, the dynamic modes of atomic force microscopy (AFM), which are based on van-der-Waals and electrostatic forces, will be introduced in the following.

The sharp probe which is mounted at the end of a cantilever structure is scanned relative to the sample surface by means of piezoelectric positioning while the cantilever's deflection is measured employing the so-called optical lever method.[Was12] In all dynamic modes of AFM the cantilever is driven to oscillate at a frequency ω by an additional piezo element during the measurement as depicted in Figure 4.4. The oscillation is monitored as the position of a laser beam on a photosensitive diode after being reflected on the topside of the cantilever. As soon as the interaction with the sample's surface atoms comes into play, the apparent spring constant of the driven oscillator is modified by the sample's force field gradient. Hence, the cantilever's resonance frequency ω_0 changes while still operated at the driving frequency. The consequence is a change in the oscillation amplitude A and the phase shift between the excitation signal and the probe's vibration.[Har99,EW14] Aiming to maximize the detected amplitude signal on the photo detector (amplitude modulation), the cantilever is driven at a fixed frequency near the resonance, but slightly off like shown in Figure 4.3. By this the change in the amplitude ΔA of the catilever's oscillation is maximized with the sign of ΔA indicating whether the interaction is repulsive or attractive.
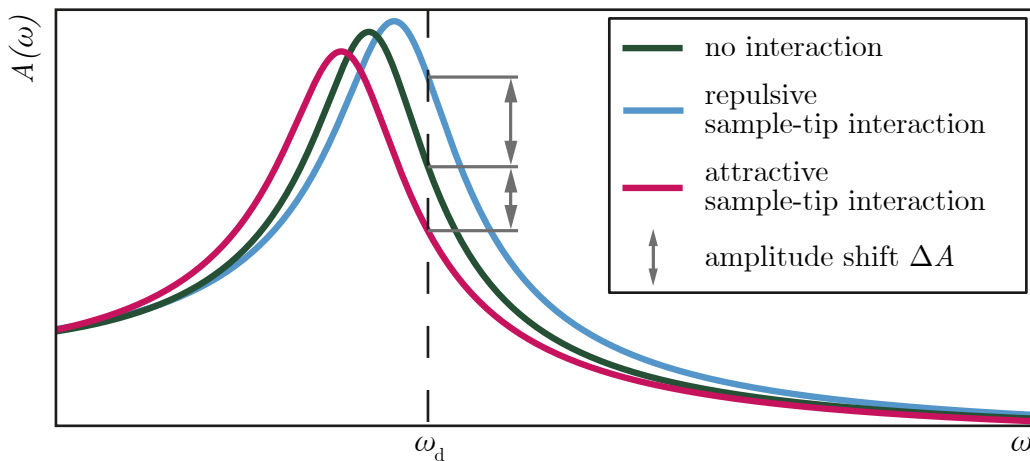

Figure 4.3: Amplitude-versus-frequency curves of the cantilever driven at a frequency ω_d depending on the force field gradient of the sample being positive or negative (attractive or repulsive interaction, respectively). The according amplitude shifts of different sign are indicated for both cases.
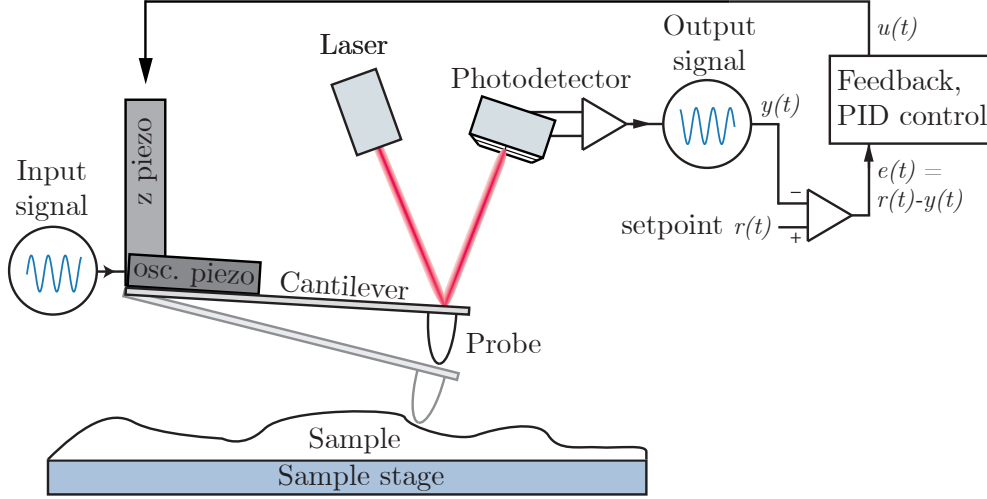
Figure 4.4: Setup for dynamic AFM modes including a sketch of the experimental setup and the block diagram of the feedback loop. Adapted and extended from[EW14]

A feedback loop is used for the height adjustment of the vertical piezo in order to tune the vibration back to the initial resonance frequency. This means that in case of an accurately reacting feedback loop a constant interaction between tip and sample is provided while scanning.

In order to understand the imaged structure it is necessary to know the tip's size and geometry, because the image always results from the mathematical convolution of the sample's and the tip's geometry. The task of the operator is then to choose appropriate scanning parameters, such as the scanning speed and the feedback parameters for the proportional (P), integral (I) and derivative (D) controller (see Figure 4.4), depending on the imaged features on the sample and their aspect ratios. The PID controller gives an output voltage to the z-piezo depending on the detected amplitude change. The output of the feedback controller is then calculated as

$$u(t) = K_\mathrm{P} \cdot e(t) + K_\mathrm{I} \cdot \int e(t)\mathrm{d}t + K_\mathrm{D} \cdot \frac{\mathrm{d}e(t)}{\mathrm{d}t} \tag{4.1.3}$$

with the difference signal $e(t)$ and the factors $K_\mathrm{P}, K_\mathrm{I}$ and K_D for the proportional, integral and derivative control, respectively.[EW14]

The resulting z-height for each grid point of the measurement then generates the image, which is first of all the map of constant effective force, but in the case of chemically homogeneous surfaces also reflects the topography. Accordingly, maps for the detected amplitude and phase shifts are output by the device. In the ideal case that the feedback reacts fast enough to the topographic changes but also does not overshoot, the amplitude and phase images do not show any features so that all the information of the sample is contained in the z-height image. In theory the lateral resolution of AFM reaches the atomic scale when high-aspect ratio probes with an atomically sharp tip are used. For standard devices and standard *NC* tips the resolution is limited to a range of 1 to 10 nm due to the probe's size and the geometry as well as the precision in its positioning.[EW14]
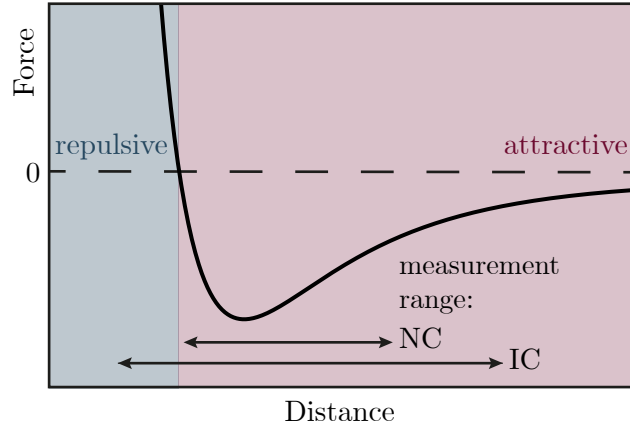
Figure 4.5: Simplified force-distance curve arising from the LENNARD-JONES potential and operating regimes of *NC*- and *IC*-AFM.

The distinction in two modes named non-contact (*NC*) and intermittent (*IC*) mode is due to two different regimes of the oscillation amplitude, at which the cantilever is operated. In case of both electrically neutral sample and tip the LENNARD-JONES potential, as it is given in Figure 4.5, shows an attractive regime because of the van-der-Waals interactions and a repulsive regime due to the Pauli exclusion principle. The *NC* mode operates within the attractive regime only, which is ensured by applying small oscillation amplitudes, while the *IC* mode makes use of higher vibration amplitudes for the cantilever. As a result, this measurement mode operates both within the attractive and the repulsive regime of the interaction potential.[EW14]

Magnetic Force Microscopy

With the aforementioned information about AFM considered, now magnetic force microscopy (MFM) can be faced in order to use the opportunities that arise from using a tip coated with a hard magnetic material, which is magnetized in a known direction before the measurement.[EW14] With the aim to solely monitor magnetic forces between the tip and the magnetic structure of a sample, which are orders of magnitudes smaller than the short-range forces desired in AFM, it is necessary to measure them at a distance in the range of 5 up to several hundred nanometers from the surface.[EW14] Usually this is achieved by performing a second scan after a *NC* topography scan, for which the probe is raised by the desired tip-lift height. This can either be realized by measuring in a certain distance to the averaged line profile for planar magnetic samples or by the so-called BARD method, which means that the second scan includes the topography from the first scan with the addition of the tip lift to every measured pixel.[EW14] This method is also referred to as contour mode and allows for the investigation of magnetic domains in samples of three-dimensional geometry, like the curved magnetic layers present on the JPs investigated in this work. Due to the ferromagnetic coating enhancing the tip radius and the increase of the sample-tip distance during the MFM measurements it appears that the lateral resolution (5 to 30 nm) is worsened compared to AFM.[HS09,EW14]

Since the technique measures the force gradient between sample and tip, the image results from the second derivative of the Zeeman energy E_Z (cf. section 2.2) of the sample in the tip's stray field under the condition that other interactions are negligible:[HS09]

$$E_{\mathrm{Z}} = -\int_{\mathrm{sample}} \vec{M}_{\mathrm{sample}} \cdot \vec{H}_{\mathrm{tip}} \mathrm{d}V. \qquad (4.1.4)$$

In this expression, the tip's magnetic field can be substituted by the negative gradient of its scalar potential $\vec{H}_{\mathrm{tip}} = -\mathrm{grad}\,\Phi_{\mathrm{tip}}$ and the sample's magnetic volume charges $\varrho = -\mathrm{div}\,\vec{M}_{\mathrm{sample}}$ as well as the surface charges $\sigma = \vec{M}_{\mathrm{sample}} \cdot \vec{n}$ can be implemented, where $\vec{M}_{\mathrm{sample}}$ is the sample magnetization and $\vec{n}$ the surface normal vector.[HRT97] The magnetostatic force, whose gradient relates to the later on measured MFM signal, can be written as

$$F_{\mathrm{Z}} = \int_{\mathrm{sample}} \sigma\,\frac{\partial \Phi_{\mathrm{tip}}}{\partial z} \mathrm{d}S + \int_{\mathrm{sample}} \varrho\,\frac{\partial \Phi_{\mathrm{tip}}}{\partial z} \mathrm{d}V, \qquad (4.1.5)$$

which is the negative gradient of the aforementioned interaction energy with z being the vertical coordinate along that the measurement is performed.[HRT97] In case that only weak interactions appear and the presence of the tip in close proximity to the sample does not influence the sample itself, the image resembles a convolution of the sample's magnetic charge pattern with the second derivative of the tip's scalar potential. For the theoretical case of Φ_{tip} being perfectly localized and the tip can be approximated as a monopole the image exactly reflects the *magnetic charge contrast* of the sample. The absence of mutual influences can be proven, if a second MFM image with reversed tip magnetization gives an inverted contrast.[HS09]

For the occurrence of reversible interactions one also speaks of *susceptibility contrast* and in case of irreversible interactions stronger than the local coercivity the term *hysteresis contrast* in used. While interpreting MFM data, it always has to be considered, that the images only depict a two-dimensional projection of the sample's charge distribution and do not offer an exact visualization of the entire magnetic information, i.e, the magnetization vector field from which the charge pattern results itself. When the tip-lift method is used, it should also be considered that the MFM image corresponds to the projection of the magnetic information from the three-dimensional surface to a two-dimensional image plane also including distortion effects. For an estimation of the three-dimensional structure of the sample's domain pattern it is necessary to combine the experimental data with micromagnetic calculations.[Har99]

4.2 Kerr Magnetometry

The Kerr magnetometer as a measurement device sensitive for a sample's magnetization is based on the magneto-optical Kerr effect (MOKE) which describes the variation of polarization and/or intensity of light reflected from a metal surface depending on its magnetization. Analogously, the Faraday effect can be observed for transmitted light. In a classical picture the effect arises from the Lorentz force which deflects the electrons of a magnetized material when they are agitated by the incident beam of linear polarization. Within the metal the electrons can be perceived as driven harmonic oscillators due to the electric force $\vec{F}_{\mathrm{el}} = -e \cdot \vec{E}$ (with the elementary charge e) exerted from the electrical field $\vec{E}$ of the incoming electromagnetic radiation. The acting of the Lorentz
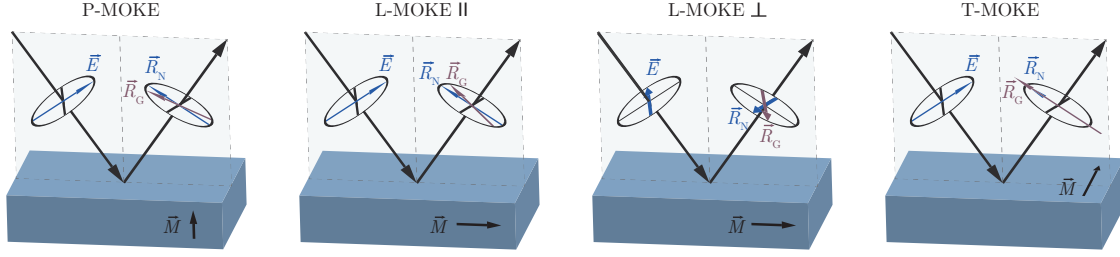
Figure 4.6: The magneto-optical Kerr effect in its different geometries. For L-MOKE use of different kinds of linearly polarized light results in Kerr amplitudes with opposing directions. The transverse geometry only yields an effect for parallel polarized light and results in a change of intensity but not in a rotated polarization plane. For reasons of clarity the Kerr amplitude R_K is not shown but the total amplitude from the superposition $R_G = R_N + R_K$.[HS09]

force $F_L = e\vec{v} \times \vec{B}$ on the electrons with velocity $\vec{v}$ is both perpendicular to the electric field vector and the magnetization of the sample. It results in a slight rotation of the oscillation plane causing the light emitted from these elementary dipoles to own a changed polarization.[HS09,BS05] The polarization of the emerging light is often characterized by a superposition of $R_G = R_N + R_K$. Here, R_N is the regularly reflected electric field amplitude parallel to the polarization plane of the incoming light. Additionally, in a magnetic sample the Kerr amplitude R_K gives rise to the magnetization dependent polarization rotation.[HS09]

Depending on the magnetization direction with respect to the surface and the plane of incidence the MOKE is divided in different geometries, shown in Figure 4.6. For some of these configurations a different behavior occurs for parallel vs. perpendicular polarized light. Here, the electric field vector of the parallel polarized beam is parallel to the plane of incidence while it is orthogonal to this plane for perpendicular polarized light.

- If the magnetization is oriented perpendicular to the sample surface the polar MOKE (P-MOKE) can be observed. Parallel as well as perpendicular polarized light leads to the same rotation due to symmetry.[HS09]

- In the longitudinal geometry (L-MOKE) the magnetization points along the plane of incidence and parallel to the surface. The sense of the Kerr amplitude's rotation is opposite for parallel and perpendicular polarization of the incident beam.[HS09]

- For a magnetization orientation perpendicular to the plane of incidence but parallel to the plane of the sample surface the term transverse MOKE (T-MOKE) is used. Only parallel polarized light creates a Kerr amplitude, which has the same direction as the regularly reflected amplitude resulting in a change of the reflected amplitude's magnitude but not in its polarization angle. On the other hand, perpendicular polarized light does not result in a Kerr amplitude, since the Lorentz force is zero when the electric field vector is parallel to the magnetization direction.[HS09]

A magnetometer with longitudinal configuration was used in this work for the magnetic characterization of Janus particles assembled in a close packed array. The device is operated by using a diode laser with a wavelength of $\lambda = 635\,\text{nm}$ which is focused to a beam diameter

on the sample surface of approximately $100 \, \mu m$.[Hol15] The additional components necessary for the recording of hysteresis curves are the following: The polarizer in the beam path behind the light source is oriented in a way that only perpendicular polarized light hits the sample in order to eliminate transverse components of the magnetization during the magnetization reversal process.[Müg16] An electromagnet provides the externally applied field parallel to the sample plane for the magnetization reversal. The analyzer is located and oriented in a certain angle in order to detect the rotation of the polarization plane while maximizing the signal-to-noise ratio.[Müg16] Additionally, converging lenses are positioned behind the analyzer to focus the reflected beam onto the detector which is the last element in the illumination path.[Müg16]

Because this setup allows to measure the magnetization properties of a sample locally (beam spot diameter $\approx 100 \, \mu m$), it is possible to only address the monolayered regions on the JP samples or an area with the planar layer system in absence of particles.

4.3   Particle Rotation Setup

For the realization of rotational experiments with the fabricated Janus particles in microfluidic environment, the transport setup existent in the group was extended in order to apply rotational external magnetic fields. The setup consists of a brightfield microscope unit, which can be moved along the z-direction with a step motor for focusing, a sample holding stage and an electromagnet which is a set of three Helmholtz coil pairs for the generation of magnetic fields along the three directions x, y and z. For electrical currents in the coils with the same direction the Helmholtz pair generates a magnetic field with a high degree of homogeneity in the central area between them, which is due to the characteristic geometry in which the distance between the parallel aligned coils and the coils' radius are equal. The sample holder is located in the Helmholtz coils' center and is horizontally movable along the x and y direction. The setup is positioned on a concrete plate mounted on a stand which is damped by a passive air pressure damping system in order to suppress disturbing vibrations during the experiments. The illuminating light from a sideways mounted LED is guided through a condensor lens in the optical path onto a non-polarizing beam splitter with a 50:50 split ratio from where half of its intensity is reflected into the objective. The used objective (*CFI Plan Apo VC 100X Oil* from *Nikon*) is an immersion objective with 100x magnification and a numerical aperture of 1.4. When the microfluidic cell containing the water based dispersion of particles is placed on the sample holder, a drop of immersion oil of $V \approx 40 \, \mu l$ needs to be placed between the cover glass and the objective in order to reach the given numerical aperture (c.f. Equation 4.1.2). The light reflected from the specimen is collected and magnified by the objective lens, passes the beam splitter and is furthermore focused by the tube lens (*TTL200* from *Thorlabs*) onto the detection unit. For the data acquisition in form of microscopic videos a high speed camera (*EoSens® 12CXP* from *Mikrotron*) is mounted on top of the microscopic unit. During the experiments, the recording parameters, like frame rate and image size, were varied and individually optimized for the desired temporal resolution and field of view.

In order to apply rotational magnetic fields, a dual channel arbitrary function generator (*AFG2225* from *Good Will Instrument Co., LTD*) was connected to the power supply for the Helmholtz coils. Due to the availability of two channels and two power supply inputs, only magnetic field configurations of two spatial directions (either xy, xz or yz) can be chosen. A rotational magnetic field $\vec{H}(t)$ is then generated by the superposition of two sinusoidal field sequences with a 90° phase shift for the two directions of the rotational plane. Exemplary, this results in

$$\vec{H}(t) = H_{\mathrm{x}} \cdot \sin(\omega t) \cdot \vec{e}_{\mathrm{x}} + H_{\mathrm{y}} \cdot \sin(\omega t + \pi/2) \cdot \vec{e}_{\mathrm{y}}, \qquad (4.3.1)$$

for the xy-plane with the rotational frequency ω and equal magnetic field magnitudes H_{x} and H_{y}. The function generator is connected to the measurement computer which allows for the remote control via a corresponding home-built *LabView* program with the interface depicted in Figure 4.8. The operator can chose the frequency, the magnetic flux densities and furthermore, whether the x and y or the x and z coils are connected to the function generator, so that the program accesses the correct calibration factors for the magnetic field output. For this, the linear relation between the applied voltage V and the generated magnetic flux density B was evaluated for each Helmholtz coil pair by Hall probe measurements. The alteration rates were determined to be $5.84\,\mathrm{mT/V}$, $8.42\,\mathrm{mT/V}$ and $8.45\,\mathrm{mT/V}$ for the x,y, and z Helmholtz coil pairs, respectively. The highest magnetic field values that can be applied in this setup with the used power supply are $8\,\mathrm{mT}$, $4\,\mathrm{mT}$ and $18\,\mathrm{mT}$ for the x,y, and z pairs, respectively.

For the transport experiments, a microfluidic chamber was prepared from a Si wafer as a substrate and a cover glass slide as a lid. The lateral boundaries were built by a quadratic piece of *Parafilm*® *M* with a $\approx 5\,\mathrm{mm}$ x $5\,\mathrm{mm}$ cut-out notch creating a chamber of the approximate dimensions $5\,\mathrm{mm}$ x $5\,\mathrm{mm}$ x $0.13\,\mathrm{mm}$. Although the theoretical volume of this chamber is $V \approx 3.25\,\mathrm{\mu l}$, it was usually filled with $10\,\mathrm{\mu l}$ of the JP dispersion by pipetting in order to avoid the trapping of air bubbles when closing the chamber with the cover glass.

Good results were also obtained, when the Si wafer piece was previously coated with a layer of polymethylmethacrylate (PMMA) and no *Parafilm*® *M* was used. After placing the JP containing drop on the substrate the glass cover slide was directly placed on top. The generated liquid film in between served as a thinner microfluidic chamber than with the above described method. The technique was used alternatively, because the working distance of the objective and the height of the microfluidic chamber are in the same range, which causes the objective to strain the chamber.

Figure 4.7: Photographs of the rotation / transport setup with the individual components. The optical path (a.-e.), the sample stage (f.-h.) and the electronic control units (i.-k.) are depicted: a. high speed camera, b. tube lens, c. beam splitter, d. 100x objective and e. LED. f. three Helmholtz coil pairs, g. movable stage, h. sample holder, i. arbitrary function generator, j. step motor control unit and k. power supply for two of the Helmholtz coil pairs.
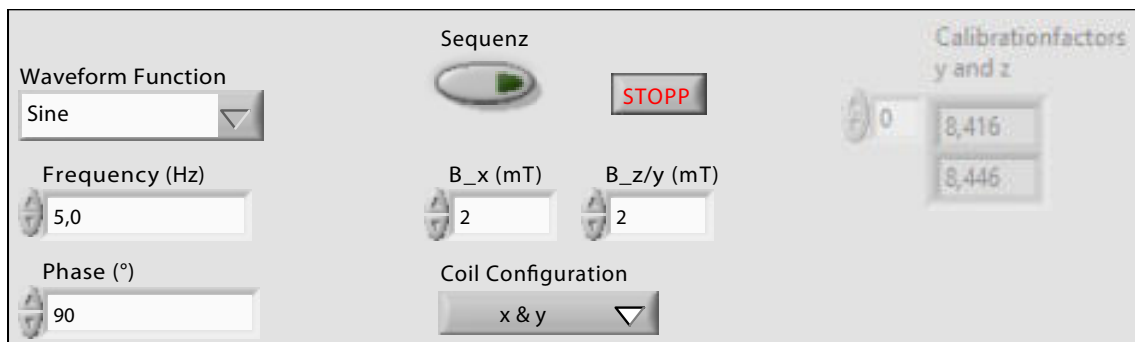

Figure 4.8: *LabView* interface for the magnetic field control via the function generator.

In this chapter the evaluated data gained from experiments and methods described in chapter 4 is presented. At first, the structural characterization of the fabricated Janus particles (JPs) is described and subsequently the magnetic properties will be discussed. Afterwards the theoretical considerations on the rotational dynamics of the JPs will be addressed before the chapter finishes with the presentation of the results from the experiments with the JPs in external rotational magnetic fields. Due to simplicity reasons, the diameter of the JPs discussed is often included as the following: a JP with a diameter of $1\,\mu m$ is in this case called a $1\,\mu m$ (sized) JP, bead or particle.

5.1 Structural Characterization

Aiming to gain a better understanding of the designed spherical magnetic building blocks in terms of appearance and geometry, the imaging techniques FIB-SEM, HIM and AFM were applied for samples containing exchange-biased JPs that were self assembled previously to the deposition process on a Si or glass substrate. The influence of the substrate material is discussed based on the recorded SEM images. Furthermore, the high resolution of HIM uncovers the structure of connecting sites between the JPs. Most importantly, the FIB-SEM results offer a possibility to calculate the half shell's actual volume from estimations about the cap's thickness gradient. In order to additionally reveal the structural properties of the caps' surfaces, AFM images were recorded from which surface roughness measurements were performed.

5.1.1 Cross-Sectional Analysis - FIB-SEM

As a starting point for the structural characterization of the designed JPs, SEM images of the beads were taken with the FIB-SEM crossbeam device *NVision40* from *Zeiss* which also allowed for the imaging of the JPs' cross sections. Prior to the milling of cross sections, the full JPs were visualized. Comparing the images shown in Figure 5.1 reveals certain characteristics of the fabricated beads. First of all, the monolayered regions that had already been identified by light microscopy could then be illustrated by SEM in detail, emphasizing on the hexagonal close-packed structures with distinct vacancies and line defects like dislocations. Secondly, $1\,\mu m$
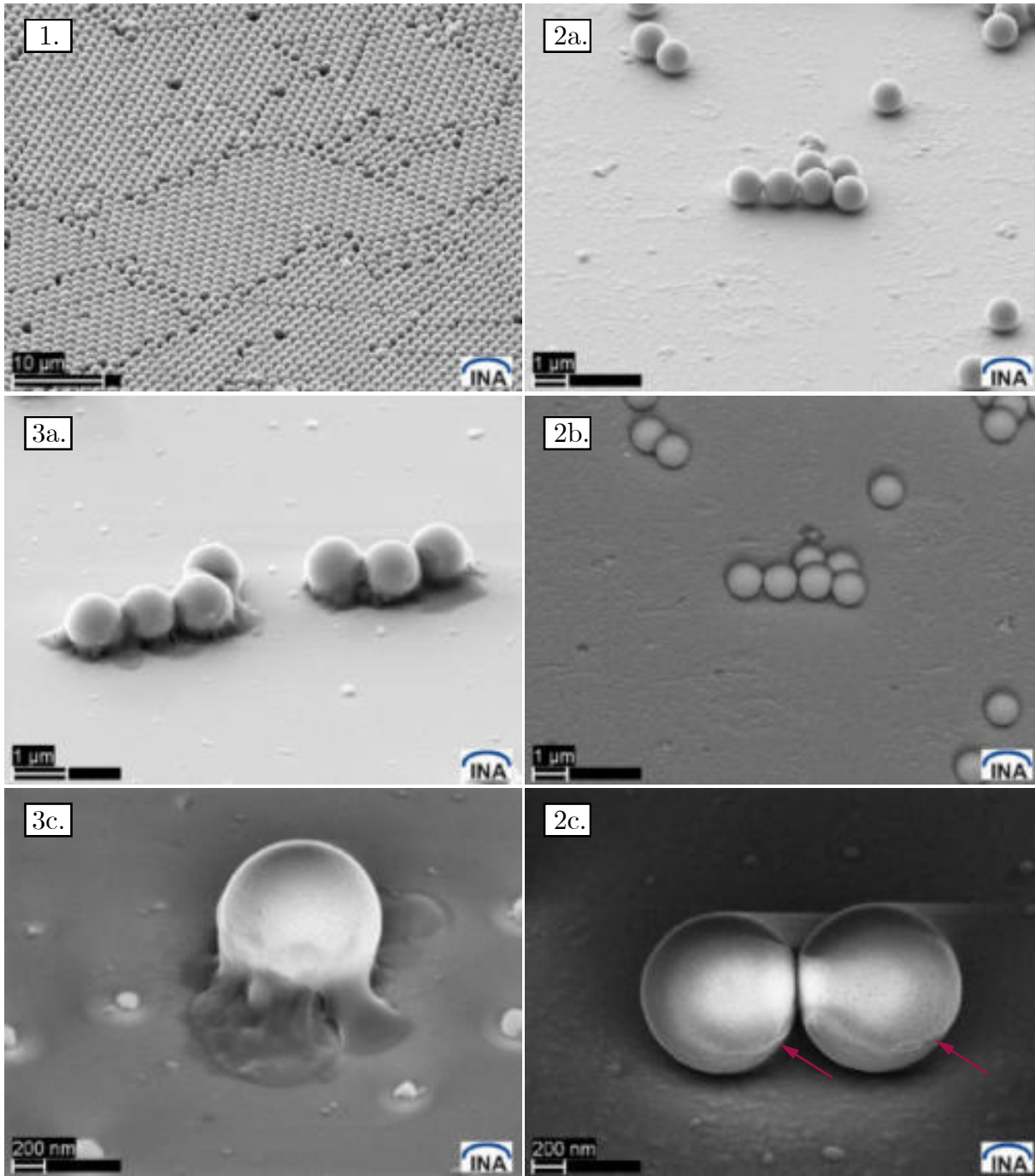
Figure 5.1: SEM images of JP samples from different fabrication procedures with a sample stage tilt of 54°: 1. Overview imaged indicating the hexagonal patterns in a monolayer with lattice dislocations of 1.5 µm JPs. 2. JPs with a diameter of 1 µm fabricated via self-assembly on glass substrate. 3. JPs (1 µm) fabricated via self-assembly on a Si substrate. For 2. and 3. images from different detectors and magnifications are shown: a. Everhart-Thornely detector (ETD), b. Energy selective backscattered electron detector (EsB) and c. Inlens detector. The images reveal a difference in deposition characteristics of the EB layer system depending on the substrate used for the silica particles. The red arrows indicate features which possible hint on the edge of the deposited cap.

sized JPs from two samples of different substrate materials were characterized, where individual JPs as well as JPs arranged in smaller groups (2-5) were imaged. While the use of a glass substrate resulted in JPs with a spherical shape, the particles fabricated via the self-assembly on a silicon wafer piece show aspherical geometry and the JPs seem to have a sticky connection to the substrate. The rather consistent deposition of the sputtered layer system on the particles assembled on a glass substrate can be attributed to the similarities in the spheres' and the substrate's properties. Both have an amorphous silica surface of similar surface roughness. On the other hand, when depositing the sputtered metal on spheres assembled on a Si substrate, the metal atoms are exposed to different surface properties. The rough surface of the silica sphere offers more nucleation sites than the smooth surface of the Si substrate, thus, causing a preferred adhesion of the sputtered atoms on the spheres. This effect of surface tension influences the shape of the particle during the thin film deposition, which was the reason for the exclusive use of glass substrates for subsequent experiments.

Although the EsB detector is suitable to obtain material contrast in SEM, the image 2b. in Figure 5.1 does not show any feature from which the cap and the plain silica bead could be distinguished. This is due to the fact, that the capping layer out of Si oxidizes after the fabrication, so that both parts of the JP effectively possess almost identical surface properties. In order to use the EsB for visualization of the cap border, another material should be considered for the capping layer of the thin film system for future experiments, such as gold, because it has a much higher atomic number and thereby results in a stronger electron scattering. In the image 2c. in Figure 5.1, which was generated from the Inlens detector, the contrast is high enough to recognize features (red arrows) on the side of the JP below its equatorial plane, which could be attributed to the edge of the deposited cap. Due to thee strong charging effects that potentially distort the image and the relatively large uncertainty uncertainty of the feature's measure, an estimation about the covered fraction of the particle is not applicable.

In the next step, the milling function of the FIB-SEM device was used to generate cross sections of JPs that were imaged in order to gain knowledge about the expected thickness gradient of the deposited cap. Prior to the milling, a protective layer derived from the decomposition of a carbon precursor gas was deposited on top of the JPs to achieve a high contrast between the metallic cap and this insulating protective layer. In the recorded SEM images of the cross-sectioned JPs the cap has a bright appearance compared to the sphere which is due to the higher electron density present in the metallic layers of the thin film system. From the images of two 1 µm sized beads performed with the three different detectors with a nominal pixel size of 2.233 nm distance measurements of the cap contrast at the sphere's top and in its equatorial region were taken with the *Carl Zeiss Tiff Annotation Editor*. The resulting mean cap thickness on the top is $\bar{t}_{\text{top}} = 53.6 \pm 17.1$ nm and the side thickness is $\bar{t}_{\text{side}} = 21.0 \pm 9.6$ nm. Here, the error is due to a statistical contribution of the measurement and a systematic uncertainty related to the method, where the latter was estimated to a value of two pixels, i.e., 4.47 nm. The results speaks for a reduction of the film thickness down to 39 ± 15 % at the equator of the sphere with a nominal thickness of 100 % at the sphere's top. Assuming that these findings can be scaled linearly to the individual layers (nominal: 5 nm Cu, 30 nm IrMn, 10 nm CoFe, 10 nm Si) of the deposited
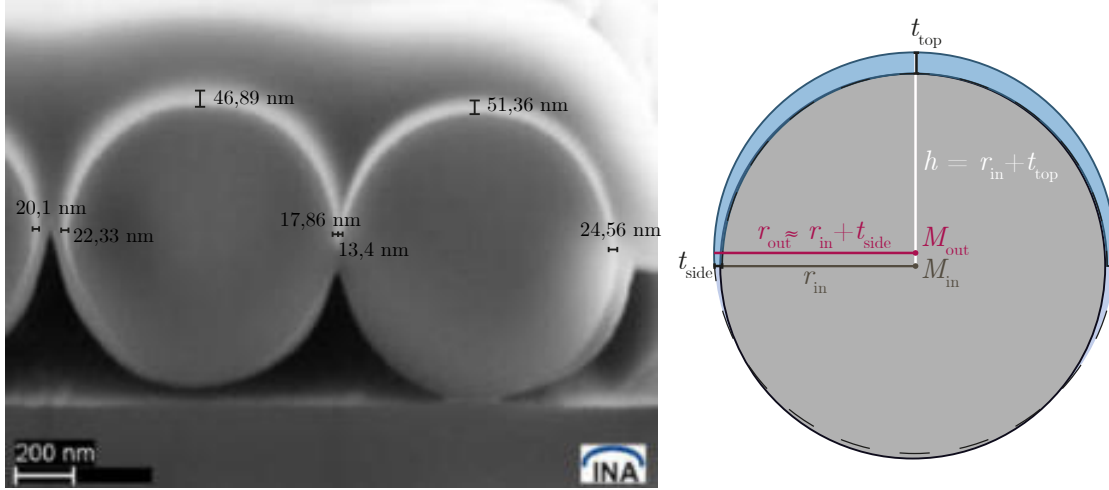
Figure 5.2: Left: tilt corrected SEM image from an ET detector of 1 μm exchange-biased JPs'
cross sections milled via FIB. Exemplary measurement markings for the evaluation
of the cap thickness are included. Right: The measured cap thickness values (t_{top}
and t_{side}) from FIB-SEM images can be used to estimate the spherical half shell's
(blue) volume. The inner circle (center M_{in}) resembles the plain silica bead and the
outer circle with a radius of r_{out} can be used to estimate the volume of a spherical
cap/dome cut at the plane of the inner circle's equator. Subsequently, subtracting
the volume of the inner half sphere yields the half shell's volume.

system, the equatorial layer thicknesses are: 2.0 nm Cu, 11.8 nm IrMn, 3.9 nm CoFe, 3.9 nm
Si. Assuming that the behavior of the here used F and AF is similar to the behavior of the
materials in Figure 2.2 it can be expected that the deposited layer system exhibits the exchange
bias field in both the polar and the equatorial region, although the thickness is reduced. At the
downscaled value of 11.8 nm for the AF the thickness dependence of H_{EB} has reached the plateau.
Furthermore the inverse thickness dependence of H_{EB} for the ferromagnetic layer suggests that
the EB is even increased at the equator of the sphere. On the other hand, the reduced Cu layer
thickness could possibly have an opposing effect: when the buffer layer is too thin in order to
promote the (111) crystal texture for the AF layer growth, the EB could even be suppressed.

Additionally, a geometric model for half shells with a thickness gradient was developed in
which the above described distance measurements were used to approximate the volume of the
half shell. In contrast to the approach of Zhang *et al.* using the relation of $t(\theta) = t_0 \cdot \sin(\theta)$
which results in a thickness of zero at the equator, the finite thicknesses of the individual layers
that are still present in the equatorial region are taken into account for. Figure 5.2 exemplary
shows one of the images used for the evaluation and a sketch with the necessary components for
the modeling of the cap's volume.
The cap volume can either be calculated in a classical approach via the subtraction of two half
spherical volumes neglecting the thickness gradient:

$$V_{\text{cap}} = \frac{2}{3} \cdot \pi((r_{\text{in}} + t_{\text{top}})^3 - r_{\text{in}}^3).$$ (5.1.1)
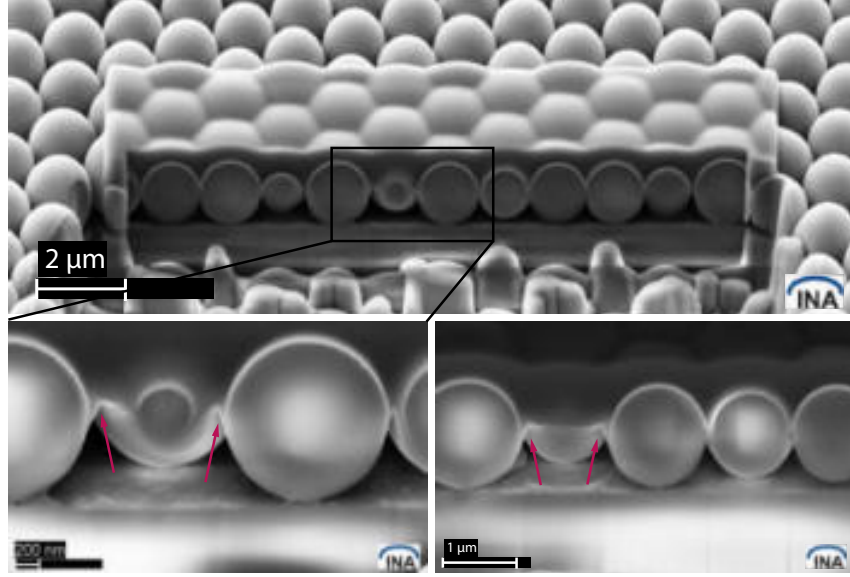
Figure 5.3: SEM micrographs with different magnification. Top: ETD image of a monolayered region of 1.5 µm JPs after the deposition of a carbon protective layer and the milling of an area for the generation of JP cross sections. Bottom left: Inlens image with higher magnification from upper image. Bottom right: Inlens image with higher magnification after further milling time. Red arrows indicate connecting sites.

Here, r_{in} denotes the inner radius measured from the center to the transition line between the sphere and the cap that has the thickness t_{top} at the upper pole. By including the measured thickness values for t_{side} at the JP's equator an alternative method is the following: the volume of the inner half sphere is subtracted from the volume of the spherical dome with radius $r_{\text{out}} = r_{\text{in}} + t_{\text{side}}$. More explicitly, the dome is the portion of the outer sphere cut off at the height $h = r_{\text{in}} + t_{\text{top}}$ by the plane, which includes the center of the inner sphere (blue part in Figure 5.2):

$$V_{\text{dome}} = \frac{\pi h^2}{3}\left(3\left(r_{\text{out}} - h\right) = \frac{\pi (r_{\text{in}} + t_{\text{top}})^2}{3}\left(3\left(r_{\text{in}} + t_{\text{side}}\right) - \left(r_{\text{in}} + t_{\text{top}}\right)\right)\right. \tag{5.1.2}$$

Since the volume of the inner sphere is

$$V_{\text{in}} = \frac{4}{3} \cdot \pi r_{\text{in}}^3, \tag{5.1.3}$$

the half shells volume can be calculated by subtracting half of the inner sphere's volume from the dome's volume:

$$V_{\text{half shell}} = V_{\text{dome}} - \frac{1}{2}V_{\text{in}} \tag{5.1.4}$$

Inserting the mean values $\bar{t}_{\text{top}}$ and $\bar{t}_{\text{side}}$ for the JPs with a diameter of 1 µm as estimated from the FIB cross sections, the corrected volume of the cap is $V_{\text{half shell}} = 6.25 \times 10^{-2}\,\mu\text{m}^3$, whereas the use of Equation 5.1.1 neglecting the thickness gradient leads to a volume of $V_{\text{cap}} = 9.62 \times 10^{-2}\,\mu\text{m}^3$. In order to use this insight for further calculations, the ratio between the corrected and the uncorrected volume is formed as $\lambda = V_{\text{cap,corr}}/V_{\text{cap}} = 66.2\,\%$. It should be noticed that this factor

can be used to also determine the volume of caps on spheres with different diameter. However, the aoccuring discrepancy increases for higher deviations in the particle size. Most importantly, λ will be used later for the consideration of the particle's magnetic moment, which is based on the volume of the ferromagnetic layer (c.f. Equation 5.3.4).

The accuracy of the introduced factor λ is strongly limited due to the errors occurring during the determination of t_{top} and t_{side} from the experimental data. In addition, there is no possibility for the operator to control the milled area during the milling process in terms of a precise JP fraction. However, tho operator can stop the milling process once the image gives the appearance of a half sphere. The effect becomes visible in Figure 5.3, where an area of a monolayered region was removed with the ion beam. Depending on the portion which had been removed with the ion beam the appearance of the cross section is different. Due to the angle between the scan line of the FIB and the hexagonal lattice of the monolayer some of the particles are cut in less or more than half. It can be distinguished that the individual JPs in this close-packed region are connected to each other by the thin film via so-called connecting sites (see red arrows in Figure 5.3).

5.1.2   Connecting Junctions between monolayered Janus Particles - HIM

For the purpose of an even more realistic depiction of the caps's surface structure, high resolution ion microscopic images were taken with a helium ion microscope of type *ORION NanoFab* from *Zeiss*. In the HIM micrographs of Figure 5.4 without sample stage tilt the connecting sites as already identified by SEM can be now analyzed with higher magnification. The higher resolution of HIM also allows to identify a filamentary or fiber like structure of these connections, while the strength of the connecting fibers varies for different positions on the sample. This observation of local inhomogeneities gives rise to the statistical nature of the sputter deposition process which also relates to the average distance between arranged particles and their size fluctuation as well as surface properties of the individual silica spheres. A second characteristic that becomes visible in the HIM images is the surface structure of the deposited material. However, the HIM technique does not offer the evaluation of surface roughness parameters, since it does not contain information about the depth of the visualized topography. For this purpose AFM measurements were performed.

5.1.3   Surface Roughness - AFM

In accordance to the above described HIM images, AFM measurements on top of a single particle ($d = 1.5\,\mu\text{m}$) reveal quantitative structural information. The acquisition of AFM NC topography images with a scan size of 500x500 nm subdivided by 512x512 measurement points on individual JPs as well as on self assembled plain silica beads was used to determine the surface roughness parameter S_{a}. This measure describes the absolute value of the arithmetical mean deviation of the surface structure from its median plane and can be determined in *Gwyddion* as follows: The measured z height data on the surface of a sphere needs to be leveled with a polynomial of second degree along both directions, x and y. Additionally, measurement artefacts within one scan line were reduced by the function 'align rows'. From a minimum of five measurements for each type
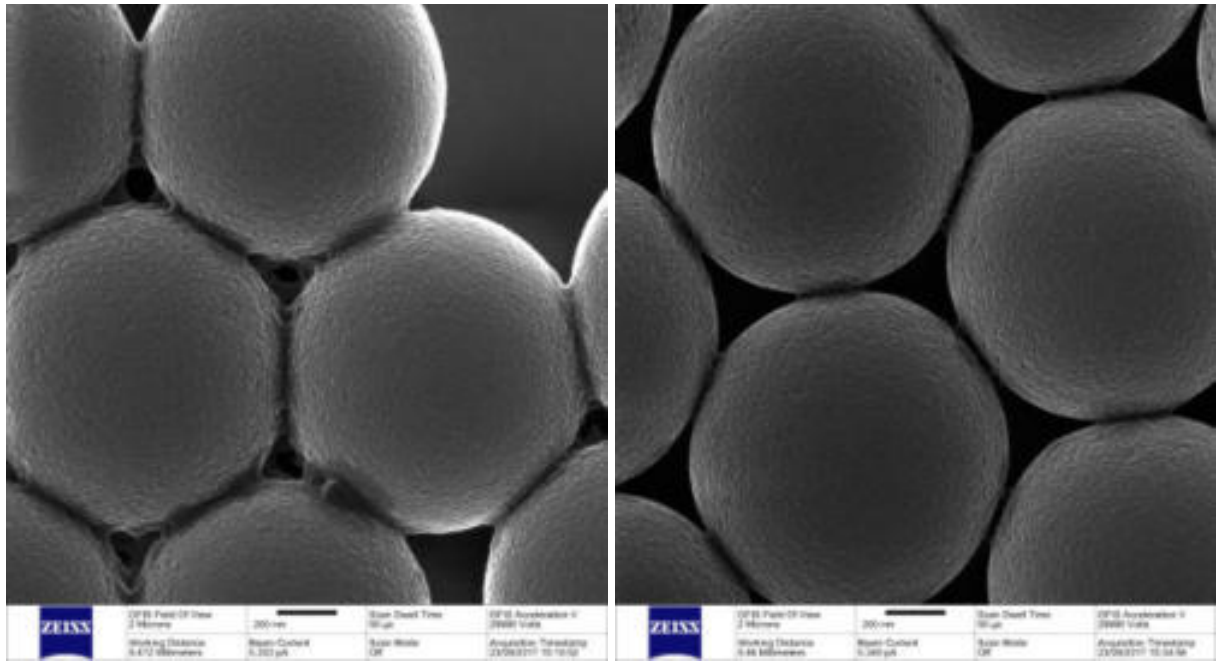
Figure 5.4: The high resolution HIM images illustrate the granular structure of the JPs magnetically capped surface. Furthermore, connecting sites induced by the deposition process between the individual spheres of an array are visible. Left and right image were recorded on different areas of the sample, thus, indicating a variation of the connecting site's strength.

of particle the surface roughness of the plain beads was determined to be $S_{\mathrm{a,pl}} = 486 \pm 105\,\mathrm{pm}$, while $S_{\mathrm{a,JP}} = 442 \pm 198\,\mathrm{pm}$ resulted for the surface of the capping layer on an exchange-biased JP. Since both values are in the range of uncertainty of the other, no significant changes on the particles' surface structure could be assigned to the thin film deposition process. In this given error range it is possible that the thin film growth is determined by the underlying surface of the bead. Still, the measured surface roughness of the EB capping layer is in the range that has been previously evaluated for thin film systems deposited on Si wafer under comparable deposition conditions (100 to 800 pm),[Mer18] which accounts for the fact that the influence of the predefined substrate structure of the silica beads is in the same order like the influence of deposition parameters.

5.2 Magnetic Characterization

For the magnetic characterization of the fabricated exchange-biased JPs that were predominantly ordered in a hexagonal array structure, MOKE magnetometry in longitudinal geometry was first used to record the magnetization curves of the JPs' caps. Since the L-MOKE measurements integrate over the magnetoresponsive volume of the sample within the focus of the laser spot including several thousands of JPs, no details concerning the microscopic alignment of magnetic moments within an individual half shell can be obtained. Therefore, MFM was used to investigate the spatial distribution of uncompensated magnetic net charges in the cap. These magnetic net charges are due to surface and/or volume charges and the technique allows to make conclusions about the magnetization pattern, which is, however, not unique.

5.2.1 Longitudinal Kerr Magnetometry

Magnetization curves of arrays of the fabricated JPs were recorded with a longitudinal Kerr magnetometer (L-MOKE) in two different measurement geometries to check for anisotropic behavior: the external magnetic field was either applied parallel (1) or perpendicular (2) with respect to the direction of the induced anisotropy axis during sputter deposition resulting in easy and hard axis loops, respectively. The Laser spot was adjusted to hit the sample on a monolayered region (ML), which can be identified by eye, as shown in Figure 3.2. However, the signal-to-noise ratio when measuring an array of magnetically capped spheres with diameters comparable to the wavelength of the incident light beam is strongly decreased compared to planar systems. Owing to the curvature of the particles, the incident beam only hits parts of the spheres. Thus, the reflected light reaching the detector originates from a small solid angle only. In order to compensate for the poor signal-to-noise ratio, the curves were recorded from 70 measurements per point and averaged over 30 hysteresis cycles. Still, it has to be considered, that the method is not sensitive to the magnetization of the full exchange-biased cap, but only senses the cap's area from which reflected laser light can be detected. For an estimation of this factor, the central angle of a half sphere from which reflected light is collected by the convex lens in the L-MOKE setup was determined to be

$$\delta = \arctan\left(\frac{\text{lens radius}}{\text{sample} - \text{lens distance}}\right) = \arctan\left(\frac{0.025\,\text{m}}{0.29\,\text{m}}\right) = 5°. \qquad (5.2.1)$$

The area around the cap's upper pole, which is measured, is derived from the area of a circle with a radius that is equivalent to the arc $b = \delta r$ on the sphere. This results in a fraction of the measured area towards the full half sphere's area of

$$\frac{A_{\text{HS,MOKE}}}{A_{\text{HS}}} = \frac{\pi(r\delta)^2}{2\pi r^2} \approx 0.4\,\%.$$

Correction: *b = 1/2 delta r*
The ratio now is 0.18 %

12.10.18 MeRe

This calculation assumes strictly parallel incident light from the Laser, however, the detectable fraction is expected to be slightly higher due to the divergence of the beam.

In addition to the measurements on monolayered regions, magnetization curves were also taken from an area with planar EB layer system on the same sample as a reference (i.e. a region on which the EB system was sputtered, but which was outside the area on which the dispersion drop was originally placed for the silica sphere self assembly). Exemplary, one measurement for each kind of region (JP ML and planar system) on a sample with $1\,\mu\text{m}$ JPs leads to the normalized magnetization curves shown in Figure 5.5.

First of all, both easy axis curves show a distinct hysteresis shift with the characteristic fields $H_{\text{EB,pl}} = -8.89 \pm 0.82\,\text{kA/m}$ and $H_{\text{EB,JP}} = -12.00 \pm 0.66\,\text{kA/m}$ for the planar system and the monolayered JP array, respectively. It can be noted that the deposition of the EB thin film system on a $1\,\mu\text{m}$ sphere array causes a significant increase of H_{EB}. The measurements were performed at three different positions for each region. While the deviation between the individual measurements for the EB of the caps in an array is less than $1\,\text{kA/m}$, the EB values differ by $6\,\text{kA/m}$ for the planar system depending on the measures position. This speaks for position
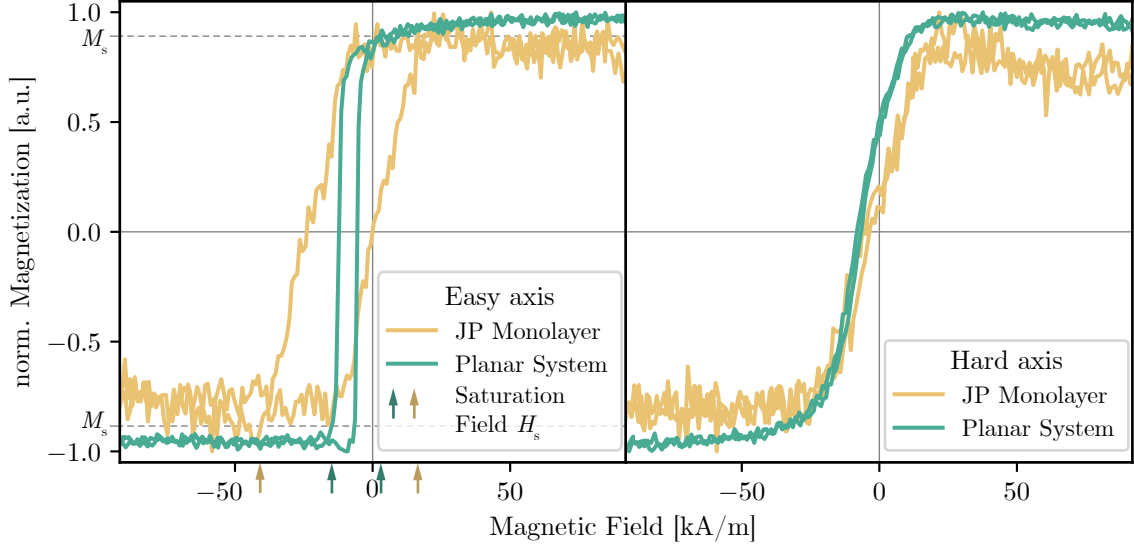
Figure 5.5: Magnetization curves recorded with LMOKE with the external field applied along the direction of the easy axis (left) and along the hard axis (right) measured on the planar EB layer system and on a monolayered region of the 1 μm JPs. The lines between are added as a guide-to-the-eye. The saturation magnetization is approximated as 90 % of the maximum magnetization in order to estimate the saturation fields which are indicated by the arrows.

dependent deposition rates during the sputter deposition process that have also been reported within the group earlier. Due to the location of the MLs in the central sample area, the deviation for the measurements of the ML is small compared to the measurements in the outer sample regions for the planar case.

The corresponding values for the coercive fields of the planar EB system and the JP ML are $H_{\mathrm{C,pl}} = 3.34 \pm 0.82\,\mathrm{kA/m}$ and $H_{\mathrm{C,JP}} = 11.95 \pm 0.66\,\mathrm{kA/m}$ for the easy axis loops, respectively. For both, the exchange bias and the coercive field, a significant increase was obtained for the JP ML, which comes along with a broader and also more tilted hysteresis curve. As a result, the magnitude of the saturation field, i.e., the external field required to magnetically saturate the sample is higher for an array of spherical half shells exhibiting EB than for a planar system. Due to the relatively high noise in the saturation region of the curves, the saturation magnetization was approximated as the value for 90 % of the maximum magnetization. The difference between the magnetic fields required for the positive and negative saturation is $\Delta H_{\mathrm{s,JP}} = 60.9\,\mathrm{kA/m}$ for the JPs and $\Delta H_{\mathrm{s,pl}} = 25.0\,\mathrm{kA/m}$ for the planar system, while the individual saturation fields are indicated as arrows in Figure 4.6.

Besides the above described characteristics in terms of the exchange bias, the coercivity and the saturation, the easy axis magnetization curve for the JP ML furthermore shows a change in the slope $\mathrm{d}M/\mathrm{d}H$ during the magnetization reversal. The reasons for the observed properties of the JP ML compared to the planar EB system are diverse since the two investigated systems differ in their dimension, their structure, their curvature and due to the latter also in their film thickness characteristics.
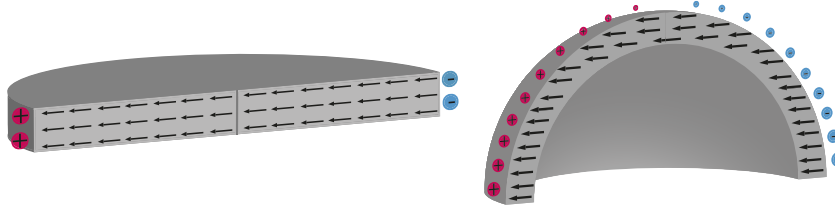
Figure 5.6: Schematic cross sections of a saturated planar disc and a saturated curved half
shell are shown depicting the different amount of net magnetic charges at the
objects' boundaries, which results in a different stray field energy contribution at
the saturated magnetization state. The higher stray field energy contribution in
the magnetic half shell is the origin of the increased broadness of the corresponding
hysteresis curve in Figure 4.6.

When comparing the above described magnetization curves, the substantial differences are the
size and the shape of the investigated magnetic bodies, which influences the shape anisotropy and
by this the magnetic characteristics. Reaching from an extended planar thin film system towards
micrometer sized planar discs the aspect ratio decreases, thus, reducing the shape anisotropy
which typically favors an in-plane magnetization state. The effect of this in-plane magnetization
in planar extended thin films causes a decrease of the demagnetization (or stray field) energy,
since the configuration minimizes the occurrence of magnetic charges at the boundary surfaces of
the film, where the magnetization possesses a finite component normal to the film surface. For
the comparison of planar thin films and thin films deposited on microstructured substrates (e.g.
discs or wires) the reduced dimensions of the latter cause the shape anisotropy to be strongly
decreased when compared to the magnetocrystalline anisotropy. As a result, there is a critical
size for ferromagnetic discs below which out-of plane magnetization states are formed, which is
commonly referred to as spin reorientation transition (c.f. subsection 2.4.1).[VOK03,ALS10] For
planar ferromagnetic discs the critical size was calculated to be around 230 a, with a being the
nearest neighbor distance,[VOK03] which, e.g., results in a feature size of 65 nm for $Co_{70}Fe_{30}$ with
a lattice constant of 0.2842 nm.[Int] Even for exchange-biased discs of sizes close to the critical
size, the occurrence of SRT is not expected, since the additional unidirectional anisotropy parallel
to the sphere's equator is induced during the deposition in an external magnetic field, which is
expected to act as a torque preventing the local reorientation of the magnetization perpendicular
to the surface.

Besides the lateral dimensions, the curvature of the here investigated particles is a second
important feature influencing the magnetization behavior. Considering a ferromagnetic half
sphere with an effective in-plane anisotropy the equilibrium magnetization points tangential
along the surface in an onion configuration. Consequently, the magnetostatic charges generating
the stray field are mainly present at the edges of the half shell and are not expected on the
spherical 'face' surface. Thus, the surface charge density differs from zero only in the equatorial
region at the magnetic poles (c.f. Figure 5.9).[SKS12] Saturating the cap leads to a single domain
magnetization state parallel to the sphere's equator for this object that is depicted in Figure 5.6
in comparison to the saturation magnetization of a disc. Looking at the demagnetization energy
again - now comparing a curved and a planar geometry - the amount of arising magnetic net

surface charges occurring in the magnetically saturated half shell is higher than for the disc. By this, both the outwards directed stray field and the internally directed demagnetization field of the saturated half shell are effectively larger than of the disc. Hence, a higher value for the Zeemann energy due to the application of an external magnetic field is required to overcompensate the stray field contribution, thus, higher magnetic field magnitudes are required for saturation. For the EB capped microsphere array, this can be interpreted as a possible reason for the broad switching field distribution of the hysteresis curve in Figure 5.5, i.e., the slopes for the magnetization reversal process $\mathrm{d}M/\mathrm{d}H$ are less steep than in case of the planar film. (The opposite effect can be observed for ferromagnetic out-of-plane magnetized caps, c.f. subsection 2.4.1[ALS10])

Moreover, the width of the magnetization curve and accordingly the coercivity might be affected by local fluctuations in the spheres' properties, i.e. size, surface roughness, magnetic characteristics, as well as irregularities in the array formation. Here, different lattice orientations in the hexagonal close-packing (c.f. Figure 5.1.1.) could affect the anisotropy within the region due to the direction of the connecting sites. As can be seen from the HIM measurements (Figure 5.4), the strength of the contact junctions can significantly differ when comparing different positions within the particle array so that the possibility for an effective exchange coupling between the spheres cannot be absolutely excluded. A mutual interaction may lead to different hysteresis curves of the individual ensembles of close-packed particles within the measured area on the sample, thus, creating a broader curve from their superposition with higher coercivity. Furthermore, it can be noted that the contribution of the stray fields arising from neighboring half shells possibly influences the magnetization reversal process of an individual cap. Similar observations were made for out-of-plane magnetized exchange-biased spherical micro arrays, which as described in subsection 2.4.1 and illustrated in Figure 2.7.[ZLL12] In this specific case of JPs with perpendicular EB, the authors observed that the switching field was enhanced by a factor of twelve times the stray field of an individual cap.

Besides the before mentioned influencing factors, i.e., shape anisotropy stray fields from neighboring caps and inhomogeneities within the array, the microstructuring of the deposited thin film system also leads to constrictions with respect to the magnetization reversal process, e.g. the formation of domain walls. Effectively, the geometric boundaries of the half shells are local barriers for domain wall motion so that the magnetization reversal can mostly be accomplished by rotational processes.

The last and probably most important aspect to notice from the magnetization curves is the EB field increase. Although the method only senses the top area of the half sphere in which no significant thickness gradient is present, the reversal process depends on the properties of the whole cap. Due to the inverse dependency of the EB field on the ferromagnetic layer thickness, the unidirectional anisotropy is increased while following the surface of the sphere towards the equator which is responsible for the enhanced effective anisotropy of the full cap. According to the findings on the here presented JPs, the increase in H_{EB} for both, in-plane and perpendicular exchange-biased nano- and microcap arrays has also been reported by other groups.[ZWM09,ZLL12]

5.2.2 Magnetic Force Microscopy

To unravel the microscopic magnetic properties of an individual sphere in high resolution, magnetic force microscopy (MFM) was used. In combination with AFM topography images in *NC* mode, MFM phase contrast images were recorded by the use of a magnetic tip while tracing the AFM topography signal in a contouring manner with a relative tip height of 100 nm and an oscillation amplitude of 60 nm. The imaged area of 1.5 μm x 1.5 μm was chosen to include a particle ($d = 1$ μm) within a close-packed area, since the forces exerted by the tip on an individual particle without neighbors caused the detachment from its original position. For a 1 μm JP the result is shown in Figure 5.7 with the z-height images from the AFM scan at the top (1.) and the normalized phase contrast MFM images below (2.).

The first column depicts the images recorded with a probe that was previously magnetized to possess a north pole at its tip while the second column represents the measurements from the use
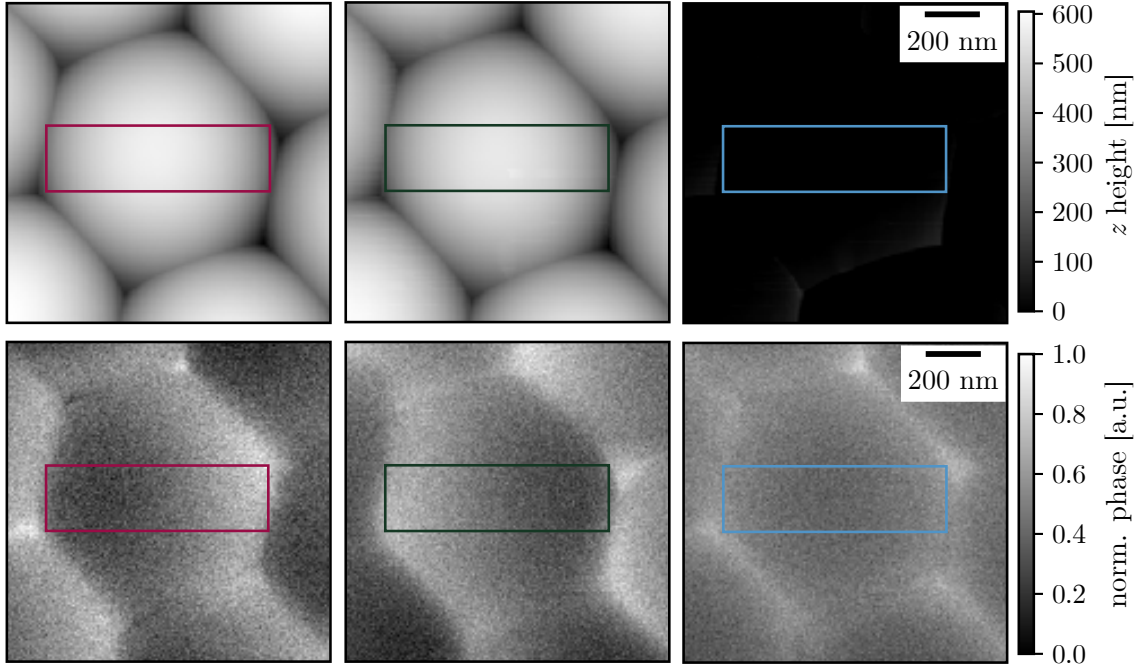

Figure 5.7: 1. AFM topography images of a 1 μm JP with its expected EB field along the x-direction as introduced by the magnetic field applied during sputter deposition and 2. corresponding MFM phase contrast images. For both rows the measurements a. were performed with a magnetic north pole tip, while a south pole tip was used for the measurements b. Subtraction of the images 1.a and 1.b results in the small contrast, i.e., no apparent topography in image 1.c indicating a good spacial alignment of the the topography scans. The fact that 2.b gives the inverted contrast of 2.a and the low contrast in the average of both images in 2.c prove that there is no significant interaction between tip and surface during the scan, i.e., magnetic charge contrast imaging is performed. The contrast variation along the x direction indicates the a alteration of the magnetic charge density from left to right and is in agreement with the EB field orientation. The rectangular patches in each picture illustrate the areas from where the line profiles in Figure 5.8 have been averaged.
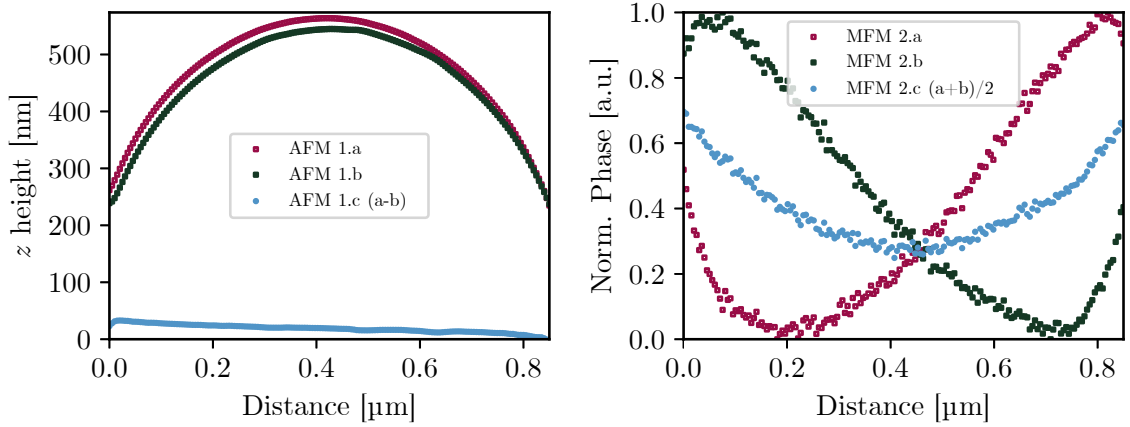
Figure 5.8: Horizontal line profiles extracted from the areas marked by the rectangles in Figure 5.7 averaged over 50 rows per image. Left: line profiles from AFM images measured at the same position for both tip magnetizations (1.a and 1.b) and the corresponding differential signal (1.c). Right: MFM line profiles for both tip magnetizations (2.a and 2.b) showing an inverted signal progression as well as the line profile for the averaged signal (2.c).

of an oppositely magnetized probe, i.e., with a magnetic south pole at its tip. The accordance of the topography images 1.a and 1.b indicate the accuracy of the spacial alignment between the two measurements, which is also emphasized by the small contrast in the difference signal in 1.c. As a quantitative measure for the contrast, the root-mean-square (RMS) of 1.c was evaluated to be $x_{rms} = 29\,\text{nm}$ which corresponds to $5\,\%$ of the measured z-height range in 1.a and 1.b. For further comparison, line profiles that have been extracted from the images by averaging over 50 lines in the the marked rectangular regions are summarized in Figure 5.8. The two MFM images 2.a and 2.b reveal an inverted contrast which is due to the use of a differently magnetized probe and is a proof for a charge contrast depiction without any susceptibility features arising from a possible influencing of the tip by the sample and vice versa (c.f. section 4.1.4). Based on the good accuracy in the alignment identified by the small contrast of the differential AFM image there are no deviations between the individual MFM images with opposing tip polarity to be expected from a misalignment of the particle, since they are measured at the same positions like the topography.

Although the distance along the z direction between the contact junctions and the top of a sphere is theoretically its radius, i.e., $500\,\text{nm}$, the obtained height profile in the AFM data is within a range of 300 to $400\,\text{nm}$. The reason for this uncertainty in the topography scan relates to the fact that the probe is not only vertically but also laterally repelled by the specimen, since the aspect ratio of the pit between two spheres is rather high compared to the geometry of the tip itself. This uncertainty propagates in the MFM measurements since they are measured in a relative position to the topographic profile that was acquired during the prior performed AFM scan. This results in a variation of the actual tip height during the MFM measurement with respect to the cap surface, and hence, the tip senses the scalar magnetic potential of the sample at a different distance, where its magnitude non-linearly decreases with increasing probe-sample distance. The propagation of the error becomes visible in the line profile shown in Figure 5.8.2.c where the average of the individual MFM measurements with reversed tip polarity is given. An
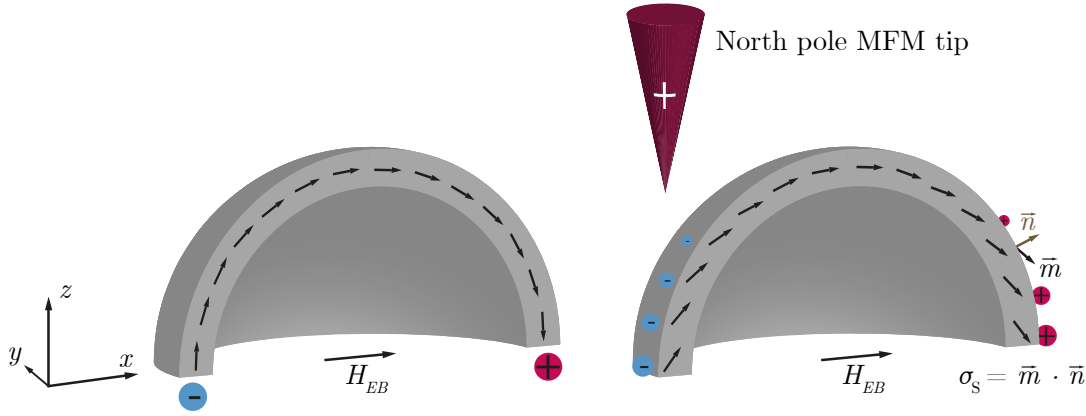
Figure 5.9: Left: magnetization distribution within a magnetic half sphere in an onion configu-
ration with strictly tangential orientation of the magnetic moments. Right: possible
magnetization pattern derived from the measured MFM image of the JP's cap.
The surface projected magnetic net charges are indicated, where the charge density
scales with the dot product of the magnetic moment $\vec{m}$ and the surface normal
vector $\vec{n}$ and is maximum for parallel and antiparallel alignment, respectively.

idealistic measurement would result in a constant phase signal of 0.5 without any contrast for the
averaged image, whereas for the present case the it is in the range of 0.25 to 0.70 with respect to
the range of the two individual normalized phase contrast images.

Assuming an onion state for the magnetic half shell, the magnetization texture is represented
by a parallel alignment of the x and y components of the magnetic moments but a successive
change in its z component as depicted in Figure 5.9. The contrast change from left to right within
the images confirms the presence of this onion state, whereas a MFM image of a magnetic vortex
would result in a radial contrast modulation from the vortex core towards the equatorial edge of
the half sphere as it has been presented by MITIN *et al.*.[MNS14] From previous measurements of
the magnetic surface charge distribution in artificial stripe domain structures[HZK13] it is known,
that a bright appearance in the MFM phase contrast image measured with a tip possessing a
north pole hints on the presence of positive magnetic net charges. For the presented MFM image
of the JP this results in the presence of negative and positive magnetic net charges on the left-
and right-hand side of the images, respectively. Correspondingly, magnetic stray field lines arise
from the magnetic pole on the particle's right side which is in accordance to the orientation of
the sample during measurement with its exchange bias field direction from left to right. Note
that MFM measurements of the 1.5 μm JPs showed the same characteristics which confirmed the
presence of an onion state within these larger caps, too.

In case of the formation of a strictly surface-tangential magnetization pattern in an onion
state the magnetic net charges only appear at the edges of the half sphere. However, it is
possible that the magnetization orientation is slightly tilted towards the surface, so that sur-
face charges are generated as it is illustrated in Figure 5.9, since the images show a contrast
gradient from the center of the cap towards its edge. This effect could be introduced, because
the magnetization pattern is predetermined by the interplay of shape anisotropy favoring the
tangential alignment of magnetic moments and the exchange bias as a unidirectional anisotropy
set during the deposition in an external magnetic field. Since the deposition field does not

follow the circumference of the spheres, but is orientated parallel to their equatorial plane, it can induce an onion state which is not strictly parallel to the half sphere's surface but with a tilted magnetization direction. Additionally, these findings might be affected by the curvature induced effective field described by GAIDIDEI *et al.* inducing a tilt on the magnetic moments from the surface of the curved object (c.f. section 2.3). Note that for these interpretations the broadened contrast gradient could also be related to the systematic uncertainty of the method: since the measurement is performed at a certain distance with respect to the origin of the magnetic net charges and due to the spatial extent of the tip, the observed magnetic charge pattern is broadened.

In case that the extraction of a quantitative measure for the effective surface charges form these measurements is desired, quantitative knowledge concerning the tip transfer function is needed to deconvolve the imaging function from the actual sample signal. In this method, called quantitative MFM (qMFM), the MFM tip's transfer function is quantified via a well characterized reference sample.[ZAV17] However, it should be noted that the magnetic characteristics of the reference sample, i.e., feature size, next neighbor interaction, etc. should be comparable to the specimen of interest, since otherwise the deconvolution procedure is not applicable.

5.3   Physical Quantities of Janus Particles

In order to model the motion dynamics of JPs in rotational external magnetic fields, the relevant physical properties of the particle need to be defined beforehand. At first, the volumes of the JP and its components, the silica sphere (s), the half shell (hs) and the ferromagnetic layer (F), can be described without considering the observed thickness gradient of the cap

$$V_{\mathrm{s}} = \frac{4}{3} \cdot \pi \cdot r_{\mathrm{s}}^3 \tag{5.3.1}$$

$$V_{\mathrm{hs}} = \frac{1}{2} \left(\frac{4}{3} \cdot \pi \cdot \left((r_{\mathrm{s}} + t_{\mathrm{hs}})^3 - r_{\mathrm{s}}^3 \right) \right) \tag{5.3.2}$$

$$V_{\mathrm{F}} = \frac{1}{2} \left(\frac{4}{3} \cdot \pi \cdot \left((r_{\mathrm{s}} + t_{\mathrm{hs}} - t_{\mathrm{cap}})^3 - (r_{\mathrm{s}} + t_{\mathrm{hs}} - t_{\mathrm{F}} - t_{\mathrm{cap}})^3 \right) \right) \tag{5.3.3}$$

with the silica sphere's radius r_{s}, the half shell's nominal thickness t_{hs}, the ferromagnet's thickness t_{F} and the capping layer thickness t_{cap}. The fabrication-induced thickness-gradient of the cap is not considered in this calculation (Equation 5.3.3). However, the correction factor λ, which was approximated to be $66.2\,\%$ for a $1\,\mu\mathrm{m}$ JP from the FIB measurements, can be added to the equation resulting in $V_{\mathrm{F,corr}} = V_{\mathrm{F}} \cdot \lambda$ and $V_{\mathrm{hs,corr}} = V_{\mathrm{hs}} \cdot \lambda$. This correction mostly affects the magnetic moment and, thus, the torque exerted from the external magnetic field, but it also affects the cap's mass and by this the overall mass of the particle, as well as the center of mass and the moment of inertia.

The magnetic moment μ_{JP} of the JP can be estimated via the ferromagnetic volume V_{F} and the saturation magnetization of the material M_{s} as follows:

$$\mu_{\mathrm{JP}} = V_{\mathrm{F,corr}} \cdot M_{\mathrm{s}}. \tag{5.3.4}$$

Table 5.1: Parameters used for calculations on the properties of JPs with three different sizes including values acquired with and without the use of the correction factor λ.

Beadsize $2r_\mathrm{s}$ [µm]	Silica density ρ_s [kg/m^3]	Mass m_JP [pg]		Mag. moment μ_JP [10^{-14} Am^2]		Moment of inertia J_JP [10^{-28} kgm^2]		Eff. density ρ_JP [kg/m^3]	
			corr.		corr.		corr.		corr.
1	1800	1.71	1.45	2.30	1.49	1.64	1.52	2763	2470
1.5	1800	4.85	4.30	4.88	3.23	10.18	9.75	2456	2255
3	2000	34.73	32.66	18.45	12.46	293.42	289.87	2324	2224

Here, it should be noted that a JP in its expected onion configuration possesses a smaller magnetic moment than compared to Equation 5.3.4 which described the moment of a magnetically saturated cap. Since the metallic half shell possesses a higher density than the silica sphere the center of mass is shifted from its geometrical center. This shift is given by[Huh17]

$$d = \frac{m_\mathrm{hs}}{m_\mathrm{hs} + m_\mathrm{s}} \cdot \frac{3}{8} \frac{(r_\mathrm{s} + t_\mathrm{hs})^4 - r_\mathrm{s}^4}{(r_\mathrm{s} + t_\mathrm{hs})^3 - r_\mathrm{s}^3} \tag{5.3.5}$$

and needs to be considered for determining the JP's moment of inertia J_JP. The individual contributions of the cap and the sphere, J_s and J_hs, are given by:

$$J_\mathrm{s} = \frac{2}{5} m_\mathrm{s} \cdot r_\mathrm{s}^2, \tag{5.3.6}$$

$$J_\mathrm{hs} = \rho_\mathrm{hs} \int_{r_\mathrm{s}}^{(r_\mathrm{s}+d_\mathrm{hs})} \mathrm{d}r \int_0^\pi \mathrm{d}\phi \int_0^\pi \mathrm{d}\theta r^4 \sin(\theta)^3 = \frac{4}{3}\pi\rho_\mathrm{hs} \cdot \frac{1}{5}((r_\mathrm{s} + d_\mathrm{hs})^5 - r_s^5). \tag{5.3.7}$$

In consideration of the parallel axis theorem, the JP's moment of inertia for a rotation through its actual center of mass is described by

$$J_\mathrm{JP} = J_\mathrm{s} + J_\mathrm{hs} + m_\mathrm{JP} \cdot d^2 \tag{5.3.8}$$

for any of the three principal axes with $m_\mathrm{JP} = m_\mathrm{s} + m_\mathrm{hs}$.

For an the estimation of buoyancy and gravitation, it is furthermore necessary to determine the effective density of the JPs by

$$\rho_\mathrm{JP} = \frac{V_\mathrm{s}}{V_\mathrm{s} + V_\mathrm{hs}} \cdot \rho_\mathrm{s} + \frac{V_\mathrm{hs}}{V_\mathrm{s} + V_\mathrm{hs}} \cdot \rho_\mathrm{hs}. \tag{5.3.9}$$

As an example, the parameters for the JPs fabricated within the group are given in Table 5.1. These numbers were calculated by using the following quantities for the layer system: $d_\mathrm{hs} = 55$ nm, $d_\mathrm{F} = 10$ nm, $d_\mathrm{cap} = 10$ nm and $M_\mathrm{s,CoFe} = 1.23 \times 10^6$ A/m for the saturation magnetization of Co$_{70}$Fe$_{30}$.[HGM17] The average density of the half shell was estimated at $\rho_\mathrm{hs} = 8000$ kg/m^3 [Huh17], while the density of the silica spheres ρ_s varied for the different bead sizes between 1800 for and 2000 kg/m^3.

5.4   Theoretical Model for the Rotation of Janus Particles

To theoretically describe the rotation dynamics of an exchange-biased JP dispersed in a viscous fluid exposed to a rotational magnetic field, like it is shown in the sketch in Figure 5.10, a model was developed. This approach is based on the two opposing torques acting on the Janus-like magnetic object: the magnetic torque from a rotating homogenous magnetic field and the viscous torque exerted by the surrounding liquid. Note that surface forces, gravity and buoyancy are not considered in the model, i.e., the sphere could be assumed as a force-free body in absence of external fields. It is important to notice that this model is conceived for a single particle under strictly laminar flow conditions, i.e, in a microfluidic environment with no solid walls in the particle's vicinity and no influence or disturbance from neighboring particles. The model can be used to simulate the motion characteristics of a JP in rotational magnetic fields and the trends of the behavior for varying strength of the applied magnetic field as well as the frequency of its rotation.
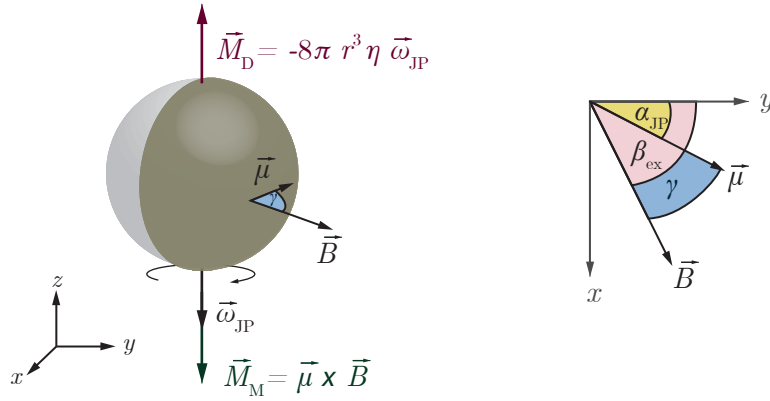

Figure 5.10: Sketch of an exchange-biased JP in a viscous fluid exposed to a rotating magnetic field in the xy-plane with the magnetic and viscous torque indicated. The magnetic moment μ in point-dipole approximation is located in the same plane and results from the assumption of the EB cap in a saturated magnetization state. The clockwise rotating magnetic field causes a clockwise rotation of the JP with an angular velocity ω_{JP}. Here, γ is the phase lag between the orientation of the cap's magnetic moment and the magnetic field. The individual orientations α_{JP} and βex with respect to the x-axis are given on the right.

Based on the rotation of the magnetic field in the xy-plane of the coordinate system, its orientation is described by the angle β_{ex} with respect to the x-axis, while the orientation of the particle with respect to the x-axis is given by α_{JP}. Consequently, the phase between the two orientations is $\gamma = \beta_{ex} - \alpha_{JP}$ (c.f. Figure 5.10. Assuming that the JP rotates with its angular velocity $\omega_{JP} = \frac{d\alpha_{JP}}{dt}$ as a result of the balance of torques between magnetic and viscous torque, M_M and M_D respectively, the equation of motion is given by

$$J_{JP}\frac{d\vec{\omega}_{JP}}{dt} = \vec{M}_D + \vec{M}_M, \tag{5.4.1}$$

with the JP's moment of inertia J_{JP}. Considering Faxén's second law for a sphere with radius r_{JP} in a viscous fluid with a dynamic viscosity η regardless of other spheres in the vicinity that

could affect the flow, the viscous torque on the sphere is given by[HB65]

$$\vec{M}_\mathrm{D} = -8\pi\, r_\mathrm{JP}^3 \cdot \eta \cdot \vec{\omega}_\mathrm{JP}, \tag{5.4.2}$$

while the hydrodynamic radius r_JP is approximated by the nominal radius of the silica sphere. Adding $\vec{M}_\mathrm{D}$ and the magnetic torque $\vec{M}_\mathrm{M}$ in point-dipole approximation, Equation 5.4.1 results in

$$J_\mathrm{JP}\frac{\mathrm{d}\omega_\mathrm{JP}}{\mathrm{d}t} = -8\pi \cdot r_{JP}^3 \cdot \eta \cdot \vec{\omega}_\mathrm{JP} + \vec{\mu}_\mathrm{JP} \times \vec{B}. \tag{5.4.3}$$

Translating the cross product in an angular dependency of the absolute values for the JP's magnetic dipole moment μ_JP and the external magnetic flux density B leads to

$$\frac{\mathrm{d}^2\alpha_\mathrm{JP}}{\mathrm{d}t^2} = \frac{1}{J_\mathrm{JP}}(-8\pi \cdot r_\mathrm{JP}^3 \cdot \eta \cdot \omega_\mathrm{JP} + \mu_\mathrm{JP} \cdot B \cdot \sin(\beta_\mathrm{ex} - \alpha_\mathrm{JP})), \tag{5.4.4}$$

with the particle's angular acceleration $\frac{\mathrm{d}^2\alpha_\mathrm{JP}}{\mathrm{d}t^2}$. To refine the equation of motion, the orientation of the rotational magnetic field β_ex needs to be written in its time dependent form of $\beta_\mathrm{ex} = \omega_\mathrm{ex} \cdot t + \beta_\mathrm{ex,0}$ with the external field's rotational frequency ω_ex. The angle $\beta_\mathrm{ex,0}$ for $t = 0$ denotes the initial misalignment between the magnetic field and the cap's magnetic moment which is assumed to be parallel to the x-axis. The second order differential equation (Equation 5.4.4) bears resemblance to a driven harmonic oscillator where the main difference is the trigonometric dependence on the difference between β_ex and α_JP.

As a result, there is no analytical solution available to the problem, i.e. numerical techniques, e.g. by using the *Python* based library *SciPy*, are necessary to solve the JP's equation of motion. For this purpose the differential equation is written as

$$\frac{\mathrm{d}^2\alpha_\mathrm{JP}}{\mathrm{d}t^2} = -c_1\,\frac{\mathrm{d}\alpha_\mathrm{JP}}{\mathrm{d}t} + c_2\,\sin(\beta_\mathrm{ex} - \alpha_\mathrm{JP}) \tag{5.4.5}$$

by introducing the coefficients c_1 and c_2. These coefficients are typically in a range of 10^7 to 10^{11} when SI units are used and cause high requirements for the computation memory. This is due to the inverse dependence on the moment of inertia with dimensions in the range of 10^{-28}. In order to reduce the necessary computational power for the solution of the differential equation, smaller values for c_1 and c_2 were desired. For this reason, the differential equation was solved on the time scale of milliseconds, which led to a transformation of the constants' units into $[1/\mathrm{ms}]$ and $[1/\mathrm{ms}^2]$ by the multiplication with the factors 10^{-3} and 10^{-6}, respectively:

$$c_1 = 10^{-3}\,\frac{8\pi \cdot R_\mathrm{JP}^3 \cdot \eta}{J_\mathrm{JP}} \quad \text{and} \quad c_2 = 10^{-6}\,\frac{\mu_\mathrm{JP} \cdot B}{J_\mathrm{JP}}. \tag{5.4.6}$$

Next, a set of two first order differential equations is generated from the derived second order differential equation in order to numerically solve the equation with the module *odeint* from the open-source library *SciPy*. The translation

$$y_0 = \alpha_\mathrm{JP}\,,\; y_1 = \frac{\mathrm{d}\alpha_\mathrm{JP}}{\mathrm{d}t}\,,\; y_2 = \frac{\mathrm{d}^2\alpha_\mathrm{JP}}{\mathrm{d}t^2} \tag{5.4.7}$$
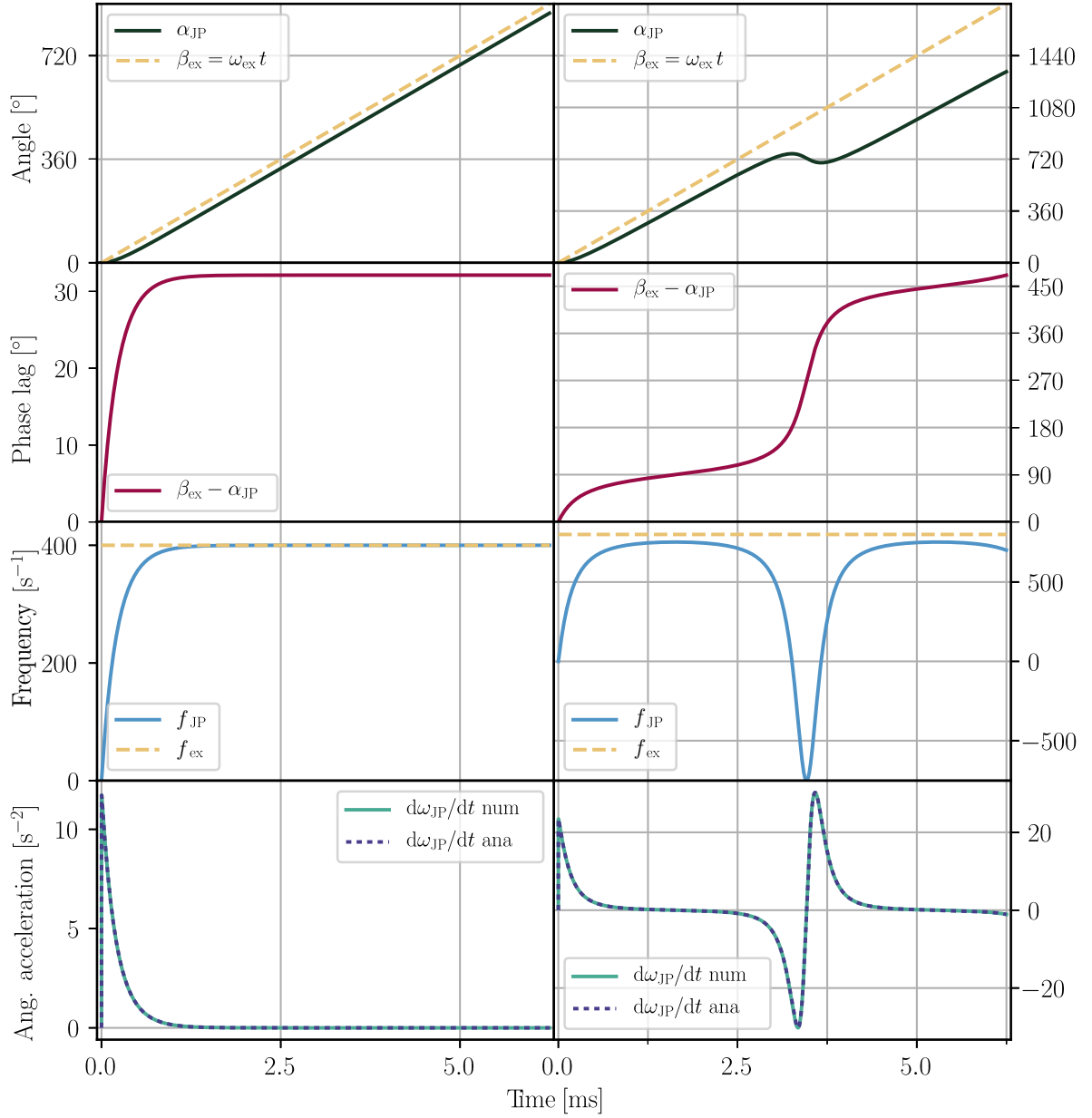
Figure 5.11: The rotation dynamics of a JP (d_{JP} =1 µm) in a rotating magnetic field with B =1 mT are illustrated by the orientation of the bead's cap, the resulting phase lag towards the external magnetic field direction ($\gamma = \beta_{ex} - \alpha_{JP}$), the frequency $f = \omega/2\pi$ of the JP in comparison to the constant driving frequency and the angular acceleration (top to bottom). The plots on the left show the simulated data for the driving field possessing a frequency of 400 Hz in which the JP rotates with a constant phase lag. For comparison the plots on the right give the characteristics for a driving field of 800 Hz while in this case the bead executes a tumbling motion. Note that the time interval is the same in all plots, while it corresponds to two and a half periods for 400 Hz and five periods for 800 Hz, as indicated by the grid. Please also note the different scaling of the y-axes.

then leads to the the following set of equations, which needs to be solved:

$$\frac{\mathrm{d}y_0}{\mathrm{d}t} = y_1 \tag{5.4.8}$$

$$\frac{\mathrm{d}y_1}{\mathrm{d}t} = -c_1 \cdot y_1 + c_2 \cdot \sin(\omega_{\mathrm{ex}} \cdot t + \beta_{\mathrm{ex},0} - y_0). \tag{5.4.9}$$

Here, t is the time interval of interest in milliseconds, which was mostly chosen to be three to ten periods of the external magnetic field's rotation. To numerically solve the equations, the initial values for the problem were given as $\beta_{\mathrm{ex},0} = 0$ and $\alpha_{\mathrm{JP},0} = 0$, i.e. a parallel alignment of the magnetic field and the cap's moment. The obtained results for $y_0 = \alpha_{\mathrm{JP}}$ and $y_1 = \frac{\mathrm{d}\alpha_{\mathrm{JP}}}{\mathrm{d}t}$ were plotted as a function of time and compared to the orientation of the applied magnetic field β_{ex} and its alteration rate ω_{ex}, respectively.

First of all, the characteristics of a stable rotation of the JPs at a constant angular velocity in presence of the driving field are investigated. As a measure for the ability of the JP to synchronously follow the external driving field with the same frequency, the phase lag $\gamma(t) = \beta_{\mathrm{ex}}(t) - \alpha_{\mathrm{JP}}(t)$ present at different times t is examined. As a second indicator for the stability of the rotation, the angular velocity can be compared to the applied driving frequency, as it is shown in the left scope of Figure 5.11. For simplicity reasons the angular velocity of the particle is given as a frequency $f_{\mathrm{JP}} = \omega_{\mathrm{JP}}/2\pi$, when comparing it to the driving field. Since the experiments with JPs are usually performed with magnetic fields in the range of 1 to 5 mT, the simulations were carried out for magnetic flux densities in this range, too. Due to the temporal resolution in the experiments being limited by the frame rate of the camera, frequencies for the external magnetic field below 250 Hz are reasonable, however, the simulations were carried out for frequencies up to 1 kHz.

Two types of motion can be distinguished from the simulated characteristics: the JP either reaches a phase-locked state with the phase lag γ being smaller than 90° within a certain time interval after an initial transient phase or the rotation becomes unstable, i.e, the JP does not rotate at the driving frequency. Starting at small frequencies and high magnetic field strengths already a small angle γ between the field and the JP's effective magnetic moment creates a torque that is large enough to overcome the viscous drag. For higher frequencies the phase lag is increased in order to create higher torques to compensate for the similarly enhanced viscous torque which now originates from the higher angular velocity. When a critical combination of B and ω_{ex} is chosen, the rotation can only be stable at a phase lag of 90°, where the magnetic torque accelerating the JP is maximized and both torques are equal.

Above a certain frequency or below a certain magnetic flux density the viscous torque becomes larger than this maximum magnetic torque. The consequence is the damping of the bead to an angular velocity at which it cannot keep up with the magnetic field anymore. At this point, no coherent phase-locking can be accomplished and γ exceeds 90° causing the magnetic torque to decrease even further. Thus, the JP does not perform a stable rotation with a constant phase lag at the driving frequency but proceeds with a tumbling motion. More explicitly, the particle still rotates, but not with a constant ω_{JP} and the number of rotations that it is lagging towards the field increases with time. Considering the angular velocity of such a bead, it is always smaller

than the driving frequency and can even be decreased to negative values due to the fact that the magnetic torque has an opposed direction once the phase lag has exceeded 180°. This behavior of a periodically changed rotation sense (inverted sign of f_{JP}) can be recognized in the frequency plot in the right scope of Figure 5.11 (and Figure 5.13). In Figure 5.11, the motion characteristics of a 1 µm sized JP in water exposed to a rotational magnetic field with $B = 1$ mT are compared for two different driving frequencies , where the figures on the right-hand side correspond to twice the frequency used for the simulation on the left-hand side, i.e., 400 and 800 Hz. For each driving frequency the orientation of the bead's cap, the resulting phase lag towards the external magnetic field direction ($\gamma = \beta_{\text{ex}} - \alpha_{\text{JP}}$), the frequency $f = \omega/2\pi$ of the JP in comparison to the constant driving frequency and the angular acceleration are given. For the latter, both the numerical derivative between consecutive values of the angular velocity (num) and the analytical derivative from the insertion of the values in Equation 5.4.5 (ana) are illustrated, while their congruence in the images indicate the validity of the numerical solution on the investigated time scale. The left images indicate a transient time which is shorter than one period and a phase-locking at $\gamma = 32°$. Referring to the plots on the right-hand side it can be seen that the phase lag shows inflection points at the angles with maximum magnetic torque, 90° and 270°, which is in agreement with the maxima and minima in the angular velocity, respectively, as well as the zero-crossings in the angular acceleration.

The higher the ratio between viscous and magnetic torque gets, the smaller the overall rotation rate of the sphere becomes and its angular velocity oscillates around zero. For a given magnetic flux density the critical value for the driving frequency $\omega_{\text{ex,c}}$ can be determined, when the maximum torque, i.e, a constant phase lag of 90° is assumed. The conditions for this are a constant angular frequency, which is exactly the driving frequency, while $\mathrm{d}^2\alpha_{\text{JP}}/\mathrm{d}t^2 = 0$. The critical ratio between ω_{ex} and B can be expressed as

$$\left(\frac{\omega_{\text{ex}}}{B}\right)_{\text{crit}} = \frac{\mu_{\text{JP}}}{8\pi r_{\text{JP}}^3 \eta}. \tag{5.4.10}$$

with $\frac{\omega_{\text{ex}}}{B} < (\frac{\omega_{\text{ex}}}{B})_{\text{crit}}$ being the condition for a synchronous and phase-locked JP rotation. For the above chosen example of a JP with a diameter of 1 µm at $B = 1$ mT rotating in water the critical frequency was evaluated to be 752 Hz, which is in accordance to the the before discussed phenomena of a stable rotation at 400 Hz and a tumbling motion at 800 Hz. The closer the parameters for a stable rotation are chosen to a combination of critical values the longer it takes until the constant phase-lock is reached, i.e., the time for the transient regime increases with respect to one period of the applied magnetic field.

To get an impression for the evolution of the phase-locked regime with respect to the parameters B and ω_{ex}, the differential equation was solved numerically for a parameter range in the time interval of five periods from which the phase lag $\gamma(t)$ was determined. Once the phase lag exceeded 90° it was set to a constant value of 90° indicating that the JP's angular velocity is not constant. The results are shown in Figure 5.12 with four false color plots for the phase lag $\gamma(t = 5T)$ of a 1 µm and a 3 µm JP in water and in an aqueous 50 w% glycerol solution. The latter was chosen to illustrate the impact of the fluid viscosity on the rotation dynamics, since
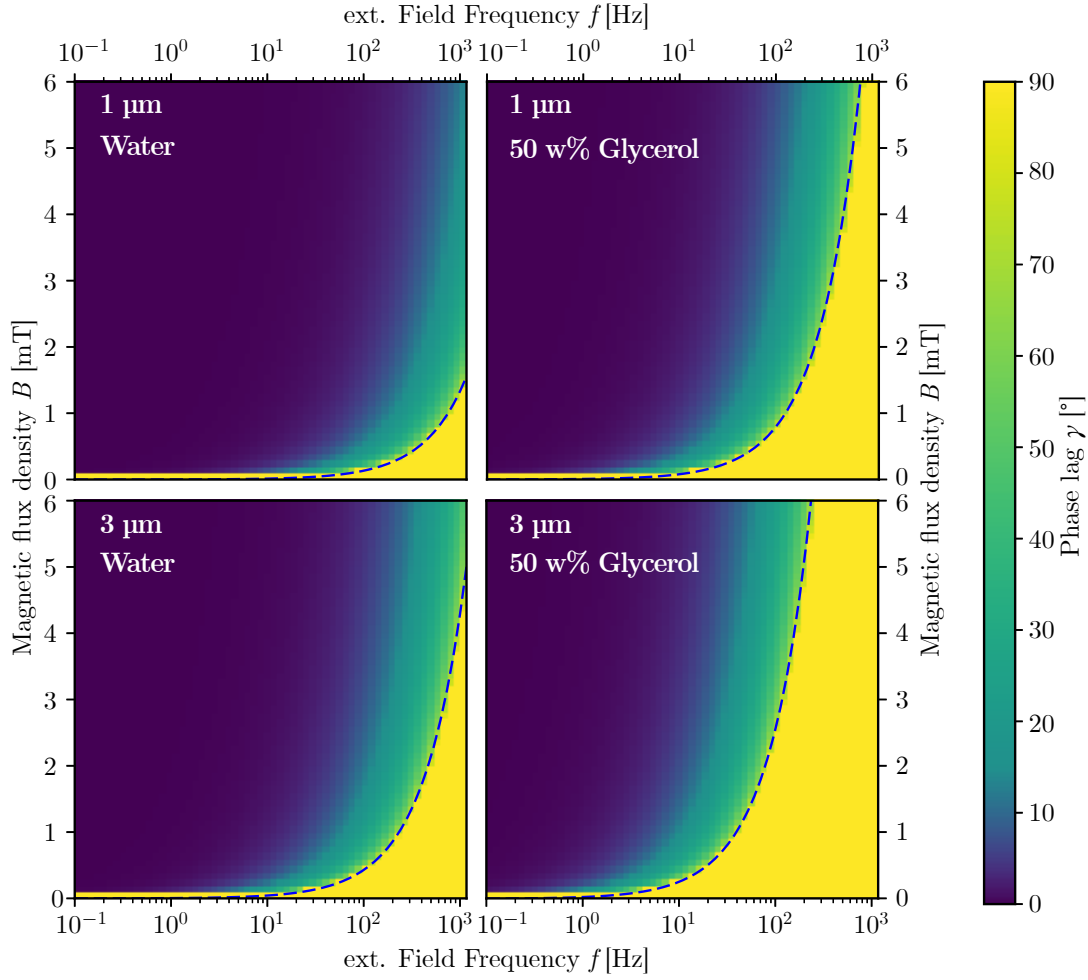
Figure 5.12: False color maps indicating the phase lag $\gamma = \beta_{\text{ex}} - \alpha_{\text{JP}}$ at the time $t = 5T$ with $T = 1/f = 2\pi 7\omega_{\text{ex}}$ being the periodic time of the rotational magnetic field. The four plots resemble the characteristic phase lag for Janus beads with a diameter of 1 and 3 μm at the top and bottom, respectively. The maps on the left show the behavior in water, whereas it is given for a 50 w% mixture of water and glycerol on the right. The dashed line depicts the critical relation of the frequency and the flux density that is given in Equation 5.4.10. Note the logarithmic scale of the abscissa and the non-linearity of the color bar for the phase angle.

the change to a medium of sixfold viscosity ($\eta_{\text{H2O}} = 1.0 \times 10^{-3}$ kg/ms ; $\eta_{\text{gly50}} = 6.0 \times 10^{-3}$ kg/ms at 20 °C [SO51]) is tantamount to an enhancement of the magnitude of the viscous torque. It can be seen that a JP suspended in the more viscous medium rotates with a larger phase lag than compared to pure water, while accordingly the tumbling state is reached at higher magnetic flux densities and at smaller driving frequencies, respectively. Moreover, it can be concluded that a JP with smaller radius is capable for a stable rotation at higher ratios $\frac{\omega_{\text{ex}}}{B}$ than a larger JP, since the critical ratio (c.f. Equation 5.4.10) decreases with increasing JP's radius. In addition to the false color maps, a dashed line is plotted for the critical magnetic flux density in dependence on the driving frequency from Equation 5.4.10. It is clearly visible that the numerically obtained and mapped phase lag γ between the JP's and the magnetic field's orientation after five periods of the driving field is in agreement with the analytically determined critical dependence of the two parameters B and $\omega_{\text{ex}} = 2\pi \cdot f_{\text{ex}}$.
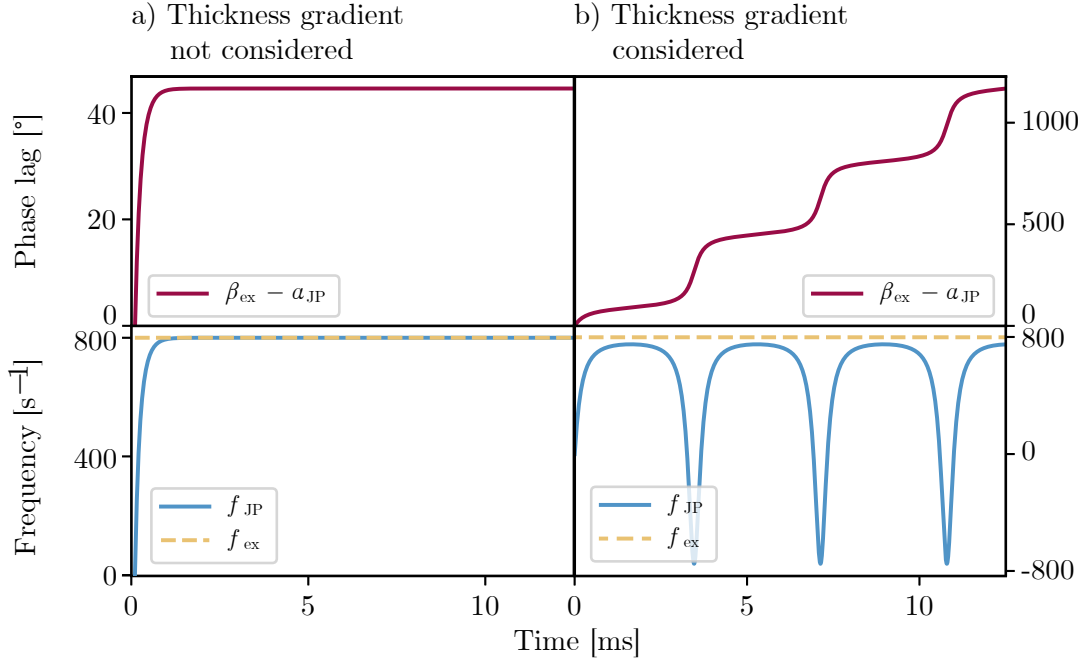
Figure 5.13: Influence of the implementation of a thickness gradient into the simulation due to the reduced volume of the ferromagnetic material. The rotation dynamics of a JP (1 µm) in a rotational driving field of 1 mT with a frequency of 800 Hz in water are shown: The upper plots illustrate the phase lag γ between the JP and the magnetic field, while the lower plots depict the JPs angular velocity, which is expressed by the frequency ($f_{JP} = \omega_{JP}/2\pi$) for better comparison to the constant frequency of the external magnetic field. While the result from the simulation not considering a thickness gradient (left) suggests a coherent rotation of the magnetic field and the JP with a constant phase lag of 45°, the result under consideration of the thickness gradient shows a JP that is lagging more than three full rotations ($1170° \,\hat{=}\, 3.25$ rotations) after the time span of 10 periods for the driving field.

All of the above shown simulations were performed the under the consideration of the magnetic half shell's thickness gradient. The implementation of the cap thickness measured with FIB-SEM is important for the outcome of the simulations, since the magnetic moment of the particle, and thus, the magnetic torque linearly depend on the volume of the ferromagnetic layer. Apart from the magnetic moment, the thickness gradient furthermore influences the particle's mass and its moment of inertia, which also affects the equation of motion. The ratio between the values for the cap volume determined with and without the thickness gradient is in the range of 66 to 68 % depending on the sphere's diameter. Scaling the ferromagnetic volume by this factor reduces its magnetic moment and the torque acting on the JP, where the differences in the simulated rotation dynamics become clearly visible in Figure 5.13. A frequency close to the critical value ($f_{ex} = 800\,\text{Hz} < f_{ex,crit}$ for $B = 1\,\text{mT}$) was chosen in order to demonstrate the effect of neglecting the thickness gradient: while the modeling without the correction factor results in a stable rotation, the use of the correction leads to a tumbling characteristic of the JP at the same conditions.

5.5   Rotational Experiments

In the present section the experimental results from experiments with $1.5\,\mu$m sized JPs in microfluidic environment that were exposed to rotational magnetic fields of variable flux density and frequency are examined. The driving field was solely applied parallel to the image plane (xy) of the optical microscope apparatus and therefore, parallel to the substrate surface of the microfluidic chamber, in which the experiments were performed. The essential goal of this work was to perform a series of proof-of-concept experiments for the rotational actuation of the novel type of exchange-biased Janus particles. The analysis of the experiments primarily includes a reliable evaluation procedure for of the particles' rotational dynamics. During the experiments, a variety of challenges and obstacles were identified, which could lead to systematic errors and will be separately discussed in chapter 6. Besides the description of the tracking procedure for the rotational movement, this section provides information about the experimentally ascertained parameter ranges for the external magnetic field which induce a synchronous rotational motion of the JP with a coherent phase relation to the applied field. Furthermore, this data was used for a quantitative comparison with the theoretical model introduced in section 5.4.

During the experiments, single images of a region of interest containing a JP in motion were taken with the camera at the chosen frame rate and saved from the frame grabber. Subsequently, the images were compiled to a video file using the *Python* module cv2. From the videos the JP's cap was distinguished from as the darker part of the sphere while the rotation of the particle with its equatorial plane was investigated to be perpendicular to the xy-plane in which the applied magnetic field rotated. To evaluate the JP's motion dynamics, the videos were analyzed with the help of the tracking software *Video Spot Tracker* as follows: a rectangular tracking region, also refereed to as track ID, was set at the position of the darker appearance of the JP's cap in the first frame. From the intensity in the rectangle the program recognizes the particle in each frame of the video file and logs the coordinates as well as the orientation of the rectangle. Based on this data, the orientation of the JP, i.e., its angle with respect to the initial orientation, can be shown graphically for the chosen time span. To guarantee sufficient temporal resolution, the frame rate was usually chosen to be ten times the frequency f_{ex} of the driving field or even higher.

In order to get a first impression of the expected particle rotation, the parameters of the rotational magnetic field were chosen to induce a stable rotation of the particle of interest with a constant angular velocity. For this, JPs dispersed in water were exposed to a rotational field with an amplitude of $B = 1\,$mT and a frequency of $f_{\mathrm{ex}} = 1\,$Hz. In order to achieve a high temporal high temporal resolution for the tracked orientation of an individual JP's cap, the images were recorded with a frame rate of $500\,$fps (frames per second). The cap orientation as a function of time is depicted in Figure 5.14 after the minimal value from every measured JP orientation was subtracted. The overall linear progression of the particle orientation with time reveals that the bead performs one full turn in one second, which is in accordance to the rotational frequency of the external field. The angular progression of the driving field is indicated by the linear equation $\beta_{\mathrm{ex}} = \omega_{\mathrm{ex}} \cdot t$. Since there is currently no possibility to correlate the beginning of the video with
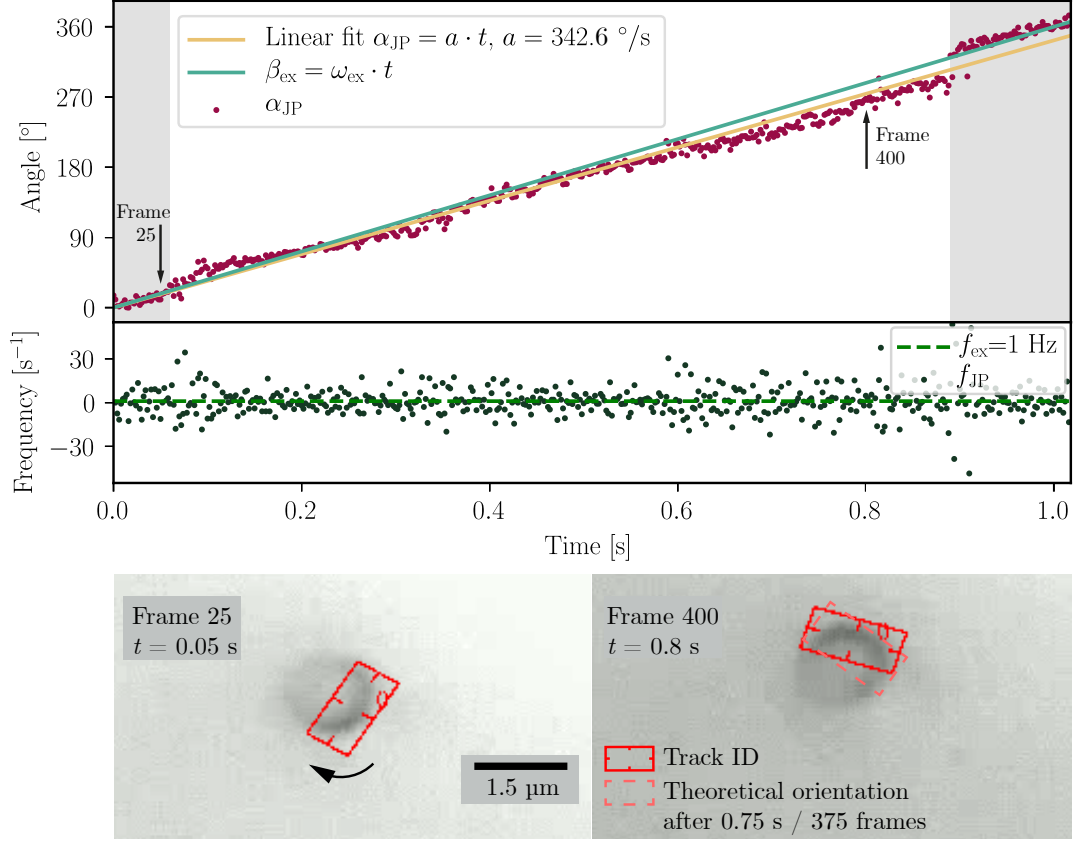
Figure 5.14: Top: the orientation angle of the tracked JP's cap is shown as a function of time for a driving field of amplitude B =1 mT and frequency f_{ex} =1 Hz recorded at 500 fps. Additionally, the orientation of the driving field is indicated assuming zero phase lag between particle and field for t =0, as well as a linear fit for the data. Areas of good agreement between the tracked orientation and the motion predicted from the driving field's orientation are marked by the gray shading. Center: the JP's time-dependent rotational frequency ($f_{JP} = \omega_{JP}/2\pi$) derived from the numerical derivative between neighboring orientation angles in comparison to the driving frequency of 1 Hz. Bottom: exemplary images from the tracking procedure indicating that the orientation of the track ID depends on the illumination conditions. A dashed rectangle is added in the right image to mark the orientation that would be expected after the time interval of Δt =0.75 s between the two frames.

the orientation of the driving field at that precise moment, the phase lag between these quantities is not accessible in the experiments but was discussed in the simulated results. Accordingly, a constant rotation in the experiment implies a phase lag between 0 and 90° which can only be neglected in the analysis, i.e., $\gamma(t = 0)$ is set to zero. Note that $t = 0$ indicates the beginning of the video, but not the start of the rotational field sequence.

The mean deviation between N measured values of α_{JP} and $\beta_{ex} = \omega_{ex}t$,

$$S_{ex} = \frac{1}{N}\sum_{i=1}^{N}|\alpha_{JP,i} - \omega_{ex}\cdot t_i|, \tag{5.5.1}$$

can be calculated as a measure for the agreement between the tracked JP orientation and the orientation of the external magnetic field. For the ranges 0 to 0.06 s and 0.9 to 1.01 s (gray shaded in Figure 5.14) the tracked data points and the graph for the driving field orientation are in good agreement with $S_{\text{ex}} = 5.4°$, while it is 14.0° for the time interval in between (0.06 to 0.9 s, not shaded). Here, the slope of the JP's orientation angle, i.e, its alteration rate ω_{JP} is reduced compared to the angular velocity of the external field ω_{ex}.

The scattering of the tracked data points around the expected linear behavior originates from the uncertainty of the tracked ID's angle which is to some extend caused by the unstable illumination from the white LED of the microscope setup which is expressed in a fluctuation of the image brightness between different frames, as shown in Figure 5.14. On the other hand, a shadow appears at the side of the particle which is facing away from the center of the focal plane, since the focusing of the parallel incident light onto the sample results in a radial intensity profile. Thus, a particle located on the left side of the illumination center is imaged with a shadow on its left side. This causes the appearance of the cap, which is meant to be tracked, to be falsified in the time range when shadow and cap are superimposed and, thus, changes the tracked angle's slope as described above.

Furthermore, a linear regression based on a least square fit procedure ($f(t) = a \cdot t + b$) was performed with the boundary condition of $b = 0$ which resulted in a slope of $a = 342.6 \pm 0.9$ °/s. The average deviation between the data for a sample size of N measurement points and the linear fit function is given by

$$S_{\text{fit}} = \frac{1}{N} \sum_{i=1}^{N} |\alpha_{\text{JP},i} - f(t_i)|, \tag{5.5.2}$$

and results in $S_{\text{fit}}^{\text{tot}} = 9.5°$ for the present case, which can be primarily attributed to the above mentioned tracking uncertainties. This average deviation from the linear regression is therefore smaller than the deviation from the predicted rotation at 1 Hz with $S_{\text{ex}}^{\text{tot}} = 12.5°$. Despite, the overall result of an angular difference of $\alpha_{\text{JP,max}} - \alpha_{\text{JP,min}} = 366°$ within the time interval of $t = 1T = 1$ s proofs a stable rotation of the sphere that is locked to the frequency of the driving field.

Additionally, the difference values between each pair of consecutive data points was used to compare the JP's angular velocity to the driving frequency. The plot containing these instantaneous frequency values in Figure 5.14 emphasizes the effect of the orientation angle's scattering which is related to the tracking uncertainties more clearly. The average angular velocity of the investigated JP is calculated from

$$\bar{f}_{\text{JP}} = \frac{\bar{\omega}_{\text{JP}}}{2\pi} = \frac{1}{2\pi(N-1)} \sum_{i=2}^{N} (\omega_i - \omega_{i-1}). \tag{5.5.3}$$

For the present case with 1 Hz as the driving frequency $\bar{f}_{\text{JP}} = 0.95 \pm 9.53$ Hz where the error represents the one sigma standard deviation, i.e., the square root of the mean squared deviations from the average $\bar{f}_{\text{JP}}$. Although the average value is close to frequency of the external field, the strong scattering causes a relatively high standard deviation.

Two observations substantiate the influence of the above described uncertainties stemming from the unstable and inhomogeneous illumination conditions in the experiment: first, the relatively high uncertainty within the estimation of the particle frequency, and second, the fact that the slope of the linear fit for the orientation angle shows a significant difference form the expected angular progress of 360° per period. The magnitude of the arising errors in the tracking procedure increases the stronger the shadow effect of the sphere is pronounced which should be considered whenever investigating rotational movements of particles. Nevertheless, the overall result of a JP performing one turn in $t = 1\,\mathrm{s}$ at a driving frequency of $1\,\mathrm{Hz}$ led to further experiments in which the influence of the external field parameters amplitude and frequency as well as of the surrounding liquid medium on the particle was investigated more closely.

In a next step, the transition region between the regimes of a stable JP rotation with $f_{\mathrm{JP}} = f_{\mathrm{ex}}$ and an unstable rotation was investigated. For the latter, the simulation results from section 5.4 predict that the particle's average angular velocity is reduced compared to the driving field while the rotation is accompanied by an oscillatory or a tumbling motion.

In a series of measurements with again $1.5\,\mathrm{\mu m}$ JPs dispersed in water, the rotational frequency of the magnetic field was kept at $f_{\mathrm{ex}} = 5\,\mathrm{Hz}$, while the magnetic flux density was varied from $1\,\mathrm{mT}$ to $3\,\mathrm{mT}$ in steps of $1\,\mathrm{mT}$. For a sufficient temporal resolution a frame rate of $500\,\mathrm{fps} = 100 \cdot f_{\mathrm{ex}}$ was chosen. The same procedure was used for an experimental series with the JPs dispersed in a solution of $50\,\mathrm{w\%}$ glycerol in water applying the rotational magnetic fields in the range from $1\,\mathrm{mT}$ to $4\,\mathrm{mT}$. Note that each series only contains data from one individual JP at different values for B. The results for the two different media, which differ in their viscosity by a factor of six, are shown in Figure 5.15. Since it is rather complicated to compare the angular orientations of the particle and the magnetic field in terms of their angular phase lag γ, the rotational lag $\Delta N = \gamma/360° = N_{\mathrm{ex}} - N_{\mathrm{JP}}$ is introduced as a measure for the number of turns the particle is lagging behind the driving field. The plots reveal that the JP in water was able to follow the rotation at $f_{\mathrm{JP}} = f_{\mathrm{ex}}$ for the magnetic flux densities of 2 and $3\,\mathrm{mT}$ while it lags more than one rotation after four periods when the driving field is set to $B = 1\,\mathrm{mT}$. In contrast, the JP in the more viscous medium lags almost four full rotations after four periods of the driving field with $B = 1\,\mathrm{mT}$ indicating a rotation velocity close to zero. A coherent rotation of the JP and the external magnetic field can only be achieved at $4\,\mathrm{mT}$ in the aqueous glycerol mixture, which is twice the value necessary for the JP that had been observed in water. Note that the two investigated particles can differ in their volume and their magnetic content, so that a direct correlation between the studied characteristics is not applicable.

From the model discussed in section 5.4 the critical magnetic flux density necessary for a coherent rotation of a $1.5\,\mathrm{\mu m}$ sized JP at $f_{\mathrm{ex}} = 5\,\mathrm{Hz}$ is predicted to be $0.01\,\mathrm{mT}$ in water and $0.06\,\mathrm{mT}$ in $50\,\mathrm{w\%}$ glycerol (c.f. Equation 5.4.10). Thus, the deviation of the critical value for B from the experiment and the model is more than a factor of 70. However, the trend of the experimental results is in qualitative agreement with the behavior expected from the model: due to the sixfold viscosity the viscous torque acting on the JP is larger in the glycerol solution which corresponds to the necessity of higher magnetic flux densities for a coherent rotation of the sphere at a fixed driving field frequency.
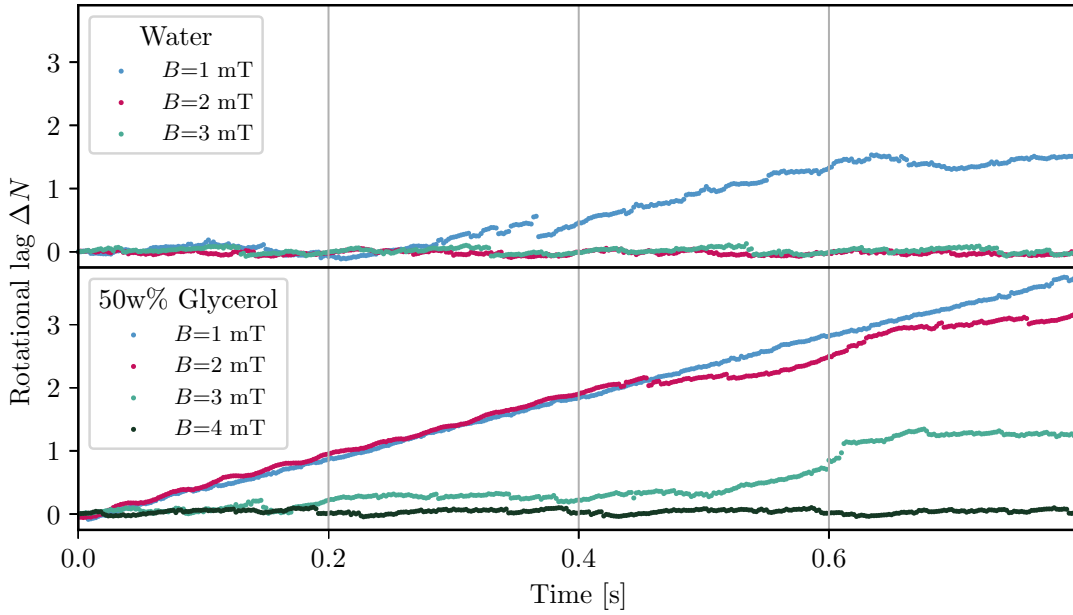
Figure 5.15: Variation of the magnetic flux density B of the driving field at $f_{\mathrm{ex}} = 5\,\mathrm{Hz}$ for a JP in water and another on in an aqueous glycerol solution (50:50 weight fraction). The rotational lag $\Delta N = \gamma/360°$ in dependence of time, with full periods indicated by the grid.

In order to actuate the particles at higher frequencies, a JP in water was exemplary investigated at $B = 2\,\mathrm{mT}$ where the driving field frequency was varied between 40, 45, 50 and 100 Hz. For appropriate temporal resolution the frame rate was adjusted to 400, 450, 500, and 500 fps for each recording, respectively. In Figure 5.16 the rotational lag $\Delta N = N_{\mathrm{ex}} - N_{\mathrm{JP}}$ of the JP in dependence of the time is given for each frequency. From the figure it becomes obvious that even for the lowest frequency of 40 Hz the rotation was not coherent, i.e., the combination of 40 Hz and 2 mT already exceeded the critical ratio for f_{ex} and B. In addition to the absolute turn difference ΔN a relative rotational lag can be determined, which is the rotational lag of the particle with respect to the number of driving field turns N_{ex}:

$$\frac{\Delta N}{N_{\mathrm{ex}}} = \frac{N_{\mathrm{ex}} - N_{\mathrm{JP}}}{N_{\mathrm{ex}}}. \tag{5.5.4}$$

This quantity offers a better comparison between experiments performed with different parameters, since it does not linearly increase as a function of time like the absolute turn difference ΔN, but approaches a constant behavior after a transient regime which was also reproduced with the theoretical model. The numerically obtained solutions for the relative rotational lag for two different sets of parameters for the external magnetic field are presented in Figure 5.17. Since the relative rotational lag is scaled by the number of driving field turns, it reaches its maximum value of unity when the particle does not move with the field at all, while it reaches its minimum for a coherent rotation of particle and magnetic field. The temporal evolution of $\frac{\Delta N}{N_{\mathrm{ex}}}$ for the performed experiments with changing driving frequency is given in the second plot of Figure 5.16 and shows similarities to the theoretical data in its oscillatory behavior. With increasing frequency the relative rotational lag increases and with it its oscillation frequency, while the amplitude of the oscillations is reduced. Furthermore, values for $\Delta N/N_{\mathrm{ex}}(t = 1\mathrm{s})$ as a comparable measure for the
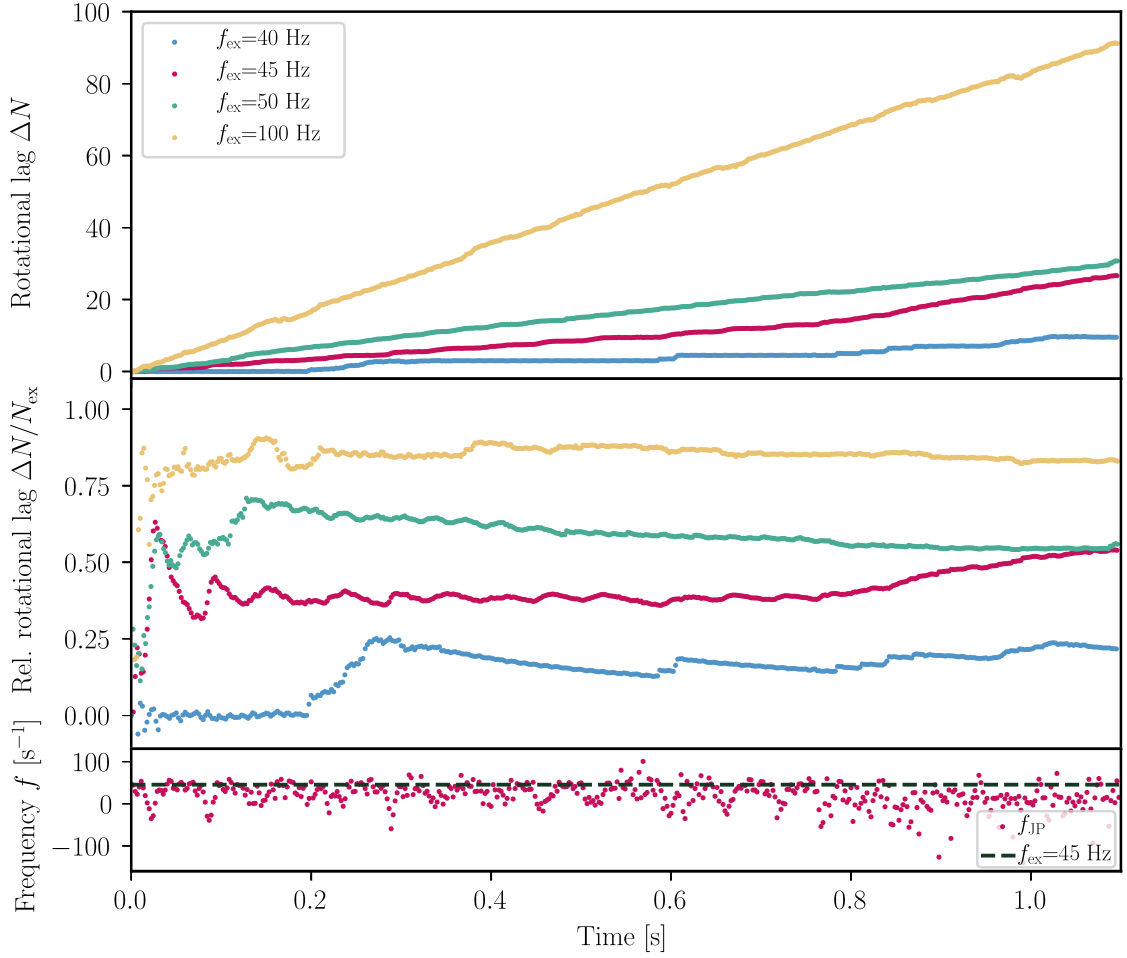
Figure 5.16: Rotational behavior of a single JP in water at four different frequencies of the external rotating magnetic field of $2\,\mathrm{mT}$. The two upper graphs show the rotational lag ΔN of the particle, i.e., how many full rotations it is lagging behind the external field, and the relative lag with respect to the number of magnetic field turns $\Delta N/N_{\mathrm{ex}}$, respectively. The lower plot exemplarily shows the frequency $f_{\mathrm{JP}} = \omega_{\mathrm{JP}}/2\pi$ of the JP in comparison to the frequency $f_{\mathrm{ex}} = 45\,\mathrm{Hz}$ of the external field. Here, a characteristic behavior that is also observed in the simulations can be recognized: the particle's direction of rotation is reversed in a periodic manner as the angular velocity changes its sign.

rotational characteristics obtained for the parameters used in the experiments are summarized in Table 5.2. For this, the number of rotations of the external magnetic field is $N_{\mathrm{ex}} = f_{\mathrm{ex}} \cdot 1\mathrm{s}$ and the number of turns $N_{\mathrm{JP}}(t = 1\mathrm{s})$ the JP performed was derived from linear regression ($f(t) = a \cdot t$) of the temporal progress of the JP's orientation angle within each experiment. Within the chosen frequency regime ($40\,\mathrm{Hz}$ to $100\,\mathrm{Hz}$) the following conclusion can be made: the lower the frequency of the applied field is, the higher is the number of turns the JP is able to perform in the same time, while the number of field rotations is reduced.

Additionally, the average frequency was determined and the values in Table 5.2 reveal that the overall velocity of the JP's rotation is reduced with increasing driving frequency above. In Figure 5.16 the JP's frequency as a function of time is exemplary given for a driving frequency of $f_{\mathrm{ex}} = 45\,\mathrm{Hz}$ and its periodically changing magnitude indicates the periodic inversion of the rotation sense that was previously observed in simulated data.
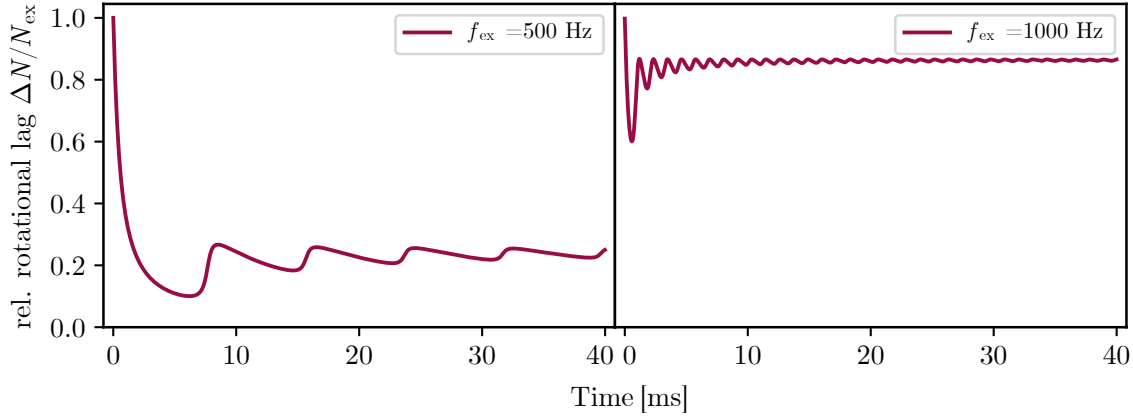
Figure 5.17: Comparison for the relative rotational lag $\Delta N = N_{\mathrm{ex}} - N_{\mathrm{JP}}$ of a $1.5\,\mu m$ JP in water with the driving frequencies 500 and 1000 Hz and $B = 1\,mT$ obtained from numerical approach explained in section 5.4.

In order to visually reconstruct the tracked motion from the recording, a sequence of individual images in the video is depicted as a montage in Figure 5.18 for the exemplary driving field of 40 Hz. The number of rotations counted by eye which are indicated by numbers in the montage is in agreement with the tracked data as well as with the result from the fitting procedure. The time intervals that show a strong increase in the relative rotational lag can be attributed to the image sequences in the montage in which the position of the cap cannot be clearly identified. This could be attributed to a rotational or tumbling motion which is not visible in the image plane. In this case the equatorial plane of the JP is not oriented perpendicular to the plane of the magnetic field's rotation but tilted towards a rather parallel alignment in which the cap faces the top or the bottom of the microfluidic chamber.

In this section, it was shown that the motion characteristics and trends predicted from the simulations (section 5.4) were qualitatively reproduced within the experiments. It was shown that the evaluation of a particle rotation is limited due to the uncertainties of the tracking procedure. Furthermore, the simulated acceleration behavior was not observed in the videos, since the start of the recorded video could not be triggered to the current phase of the driving field. Thus, the missing relation between the orientation of the magnetic field and the particle's orientation also explains why the value of the constant phase lag in the case of stable rotation conditions could not be evaluated. Due to this, the experiments were analyzed with respect to

Table 5.2: Summary of the JP's motion characteristics for rotational fields of the frequency f_{ex} at $B = 2\,mT$. The absolute and the relative rotational lag evaluated from a linear fit for the tracked orientation angle are given for the time interval of $1\,s$. Additionally, the average frequency of the JP in this time interval is given.

Frequency f_{ex}[Hz]	40	45	50	100
N_{JP}	33.13	22.98	22.07	17.02
ΔN	6.87	22.02	27.93	82.98
$\Delta N/N_{\mathrm{ex}}$	0.17	0.49	0.56	0.83
$\bar{f}_{\mathrm{JP}}$ [Hz]	33.45 ± 34.06	22.93 ± 36.27	22.89 ± 29.10	17.04 ± 70.58

the occurrence of unstable and stable rotational states with the constant phase lag remaining unknown. Additionally, the expected increase of the critical ratio ω_{ex}/B for an enhanced viscosity of the surrounding fluid was proven by the data acquired from experiments in two media that differ in their viscosity by a factor of six. The critical magnetic flux density for the actuation of the particles in water was found to be between 1 and 2 mT, while it was between 3 and 4 mT in case of the aqueous glycerol solution as the liquid medium. Furthermore, the rotational lag in case of an asynchronous, non-coherent response of the bead was shown to be increased with increasing frequency or decreasing magnetic flux density of the driving field. However, the obtained values for the investigated characteristics, like the (relative) rotational lag of a JP, differ from the values predicted from the model. The theoretically expected critical magnetic flux density for a fixed driving frequency (c.f. Equation 5.4.10) is at least 70 times higher than the experimentally obtained limit for a constant rotation. Possible reasons for the mentioned deviations between the theoretical predictions and the experimental findings will be discussed in chapter 6 including potential improvements for further research. Over all, the experimental results demonstrate that JPs can be actuated by by an external driving field rotating in the image plane within a range of experimentally realizable parameters for B and f_{ex}.
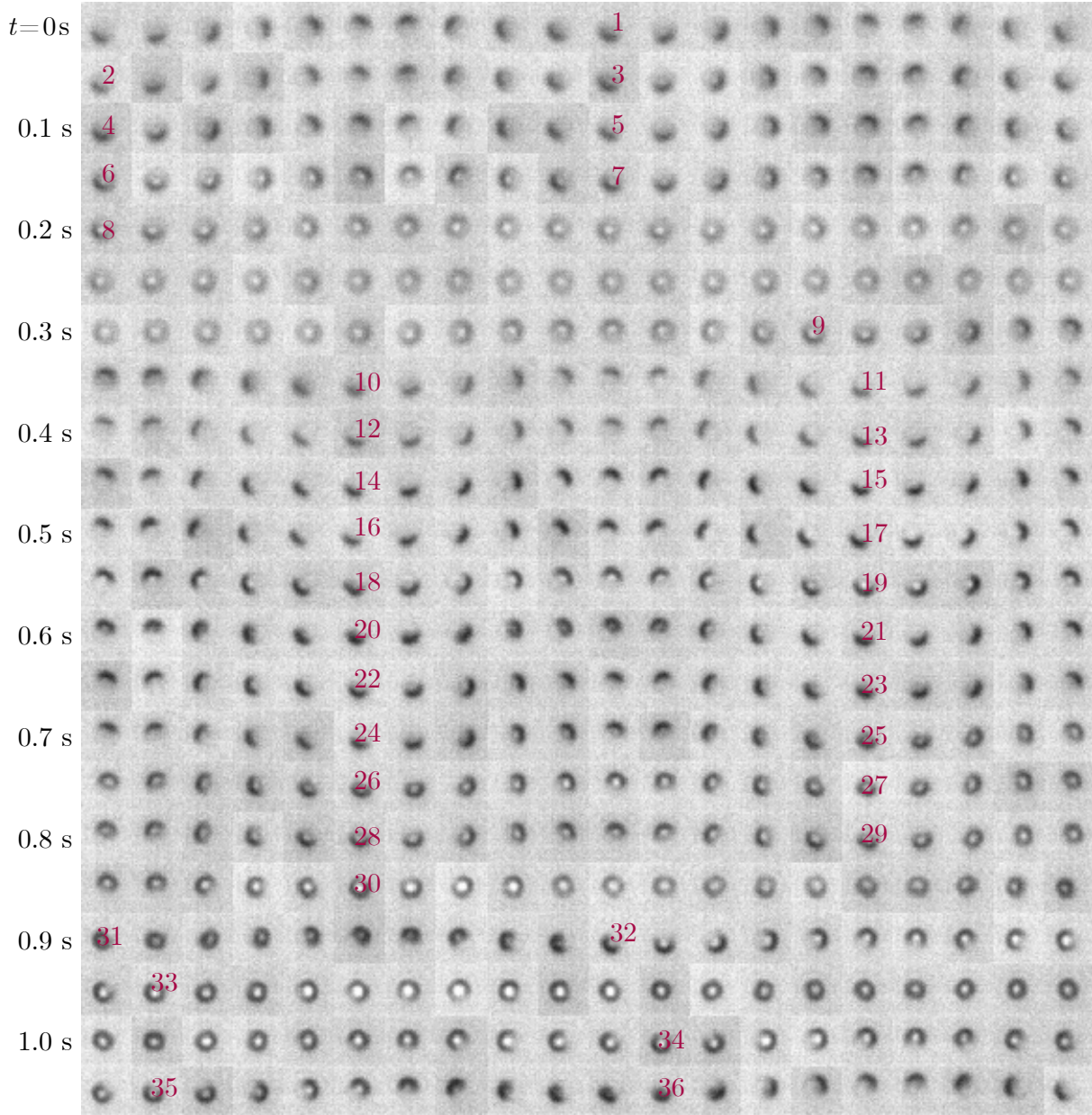
Figure 5.18: Montage of a JP in an external rotational field of $f_{\mathrm{ex}} =40\,\mathrm{Hz}$ and $B =2\,\mathrm{mT}$. From the frame rate of $400\,\mathrm{fps}$ it can be deduced that one line resembles two rotations of the external field. A number is put for every image in which the orientation of the cap is congruent with the first image. This leads to 44 rotations of the magnetic field, while only 36 rotations can be distinguished for the cap of the JP within the time span of the composed images. The data for this experiment acquired with the tracking software is given in Figure 5.16 and accordingly shows a rotational lag of 8 rotations after the investigated time interval of $t = 44T$.

In this chapter the challenges and obstacles that were faced during the experimental procedure for the rotational actuation of the before fabricated and characterized exchange-biased JPs are described. Based on this discussion, potential strategies for future experiments are presented. Moreover, possible reasons for the deviations between the simulated and the experimentally observed rotation dynamics of the JPs are discussed along with an outlook for perspective techniques which could be used for further characterization of the novel microscopic magnetic objects.

For the preparation of the experiment, the volume with the JP solution was dispersed by ultrasonication for 5 to 10 minutes and then applied to the substrate while thoroughly dispersing the drop with the microliter pipette. Subsequently the sample was covered by the glass cover slide and moved to the sample stage in the experimental setup. Within this time the particles are always affected by the earth's gravitational field, which forces the particles to sediment to the ground of both the Eppendorf tube and the microfluidic chamber after application of the fluid due to their comparably larger density with respect to the carrier liquid. Based on the properties evaluated for the 1.5 μm JPs in section 5.3 the sedimentation velocity was determined from balancing gravity, buoyancy, and drag force. For a 1.5 μm sized exchange-biased JP this results in a sedimentation velocity of $v_\mathrm{sed} = 1.5\,\mathrm{\mu m/s}$ in water and $v_\mathrm{sed} = 0.3\,\mathrm{\mu m/s}$ in the aqueous glycerol solution with a dynamic viscosity of $\eta_\mathrm{gly50} = 6.0 \times 10^{-3}\,\mathrm{kg/ms}$[SO51], if the distance-dependent drag coefficient is neglected. This leads to the assumption that at the start of the experiment most of the particles have already sedimented to their equilibrium height above the substrate surface, since the height of the chamber is at maximum 100 μm. Some particles moved out of the current focal plane during the experiment which is due to sedimentation so that no videos could be recorded. In order to solve this issue, the JP sedimentation velocity could be reduced for further experiments. This could be either achieved by changing the density of the carrier fluid in which the particles are dispersed or by changing the particle density, e.g., the use of polymeric particles possessing a smaller density. Note that this would shift the JPs' center of mass further to the capped side and therefore directly influences the rotational properties.

In addition, some of the observed particles in the microfluidic chamber were already adsorbed on the sample surface which was assumed, since these particles could not be actuated within the experimentally accessible strength range of the external magnetic field. Besides the adsorbed particles, a high amount of particles visible in the image frame showed agglomeration to larger clusters. During the experiments, the size of these particle agglomerates or clusters increased which is explained by the remanent ferromagnetic moment of the particle caps giving rise to attractive magnetostatic interaction between the particles. Calculating the interparticulate magnetostatic force in point-dipole approximation with Equation 2.5.2 for parallel aligned moments of magnetically saturated 1.5 µm sized JPs, its magnitude exceeds the interparticulate surface forces, the surface forces between the JP and the substrate surfaces as well as gravity and buoyancy for distances below 10 µm in pure water with an ionic strength of $I = 10^{-5}$ mol/l and the $\zeta-$potential of silica spheres. The resulting agglomeration of the beads is a major challenge when it is desired to focus on the rotation dynamics of individual particles. Potential improvements in terms of reduced agglomeration could be achieved by enhancing the electrostatic repulsion between the particles. Possible methods include changing the ionic strength of the fluid, e.g., by the addition of surfactants,[SGM09] and the functionalization of the particle surface for an enhanced $\zeta-$potential. Furthermore, the adsorption on the substrate surface could be prevented by the application of electric fields for electrostatic repulsion between the substrate and the cover glass by introducing electrically conducting coatings to the substrate and the cover glass, acting as capacitor.

Due to the distance-dependent drag coefficient, the viscous torque increases with decreasing distance between the particle and the walls in its vicinity. While the drag force coefficient can be determined by a Taylor expansion,[WSFX05,HB65] however, no option has been found in literature for implementing a distance dependent coefficient for the drag torque in the presented equation of motion. Nevertheless, the addition of an accurate drag torque coefficient is desirable and would result in critical values for B at a given frequency which are increased by the distance-dependent factor. This would lead to theoretical results that are effectively closer to the experimentally observed limits for a coherent rotation. In order to correctly model the drag torque coefficient, further experimental information concerning the particle-substrate distance would be necessary. This could be achieved by precisely tuning the focus of the microscopic unit from the substrate to the sphere's location under the condition of a reliable and uniform movement of the microscope's step motor without slippage effects. For the recorded videos, this distance remains so far unknown which furthermore makes the comparison of individual particles in terms of their rotational ability not applicable. Apart from the neglected drag coefficient, the viscous torque has been approximated by the use of the nominal sphere radius instead of the hydrodynamic radius of the sphere. The result is an uncertainty in the model which could be corrected by experimentally determining the hydrodynamic radius of the JPs in the liquid medium which is used for the experiment.

Another uncertainty of the simulated rotation dynamics in the theoretical model originates from the JP's magnetic moment, which was assumed as a magnetically saturated point-dipole without spatial extent, although the magnetic characterization confirmed the presence of an
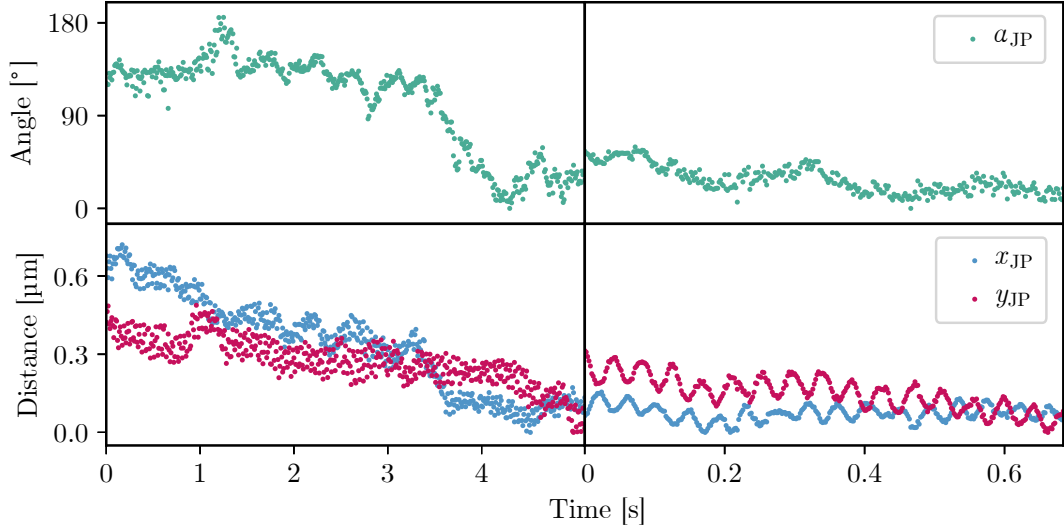
Figure 6.1: The brownian motion of a JP in the absence of an external magnetic field in terms of its $x-$ and $y-$coordinates and the angular orientation of the cap as a function of time. Left: 100 fps. Right: 500 fps. - The plot of the JP position with higher temporal resolution reveals oscillations in the measurement, originating from an external vibrations, e.g., acoustics.

onion state, i.e., the magnetic microstructure within the curved geometry is much more complex than treated in the model. As a result, the modeling was performed for magnetic moments that are higher than those of the fabricated particles in their remanent state. A potentially more realistic approximation could be made using the projection of the magnetization distribution onto the equatorial plane of the JP. Thus, only the magnetization components parallel to this plane are considered for the equivalent point-dipole, which corresponds to the magnetic moment of a saturated planar disc with the same radius. By this, the critical value for B would furthermore be increased from 10 to 20 µT for a 1.5 µm JP rotating with a driving field of 5 Hz in water.

For a more detailed understanding of the rotation dynamics of a JP actuated by a rotating magnetic field, it is desired to monitor the acceleration of the particle once it is exposed to the driving field. This could be achieved by a software-based triggering of the video recording with the start of the magnetic field sequence. The correlation between the initial cap orientation and the direction of the magnetic field would additionally offer a possibility to measure the phase lag γ in case of a stable rotation that is coherent with the external magnetic field.

In order to compare the previously presented results of JPs actuated by rotating magnetic fields to the intrinsic motion of a JP in aqueous environment, videos of a JP were recorded at frame rates of 100 and 500 fps. In this case, the $x-$ and $y-$coordinates of the JP's position were tracked in addition to its orientation and are illustrated in Figure 6.1. Within a time span of 5 s the JP rotates within an angular regime of 0° to 180° and moves translationally in an area of $y_{max} \cdot x_{max}$=0.35 µm².

The mean squared displacement for the Brownian motion of a particle in an infinite fluid as considered by Einstein[Dem13] would result in

$$\overline{x^2}(t = 5 \text{ s}) = \frac{k_\mathrm{B}T}{3\pi\eta r} \cdot t = 2.9 \, \mu\mathrm{m}^2, \tag{6.0.1}$$

which suggests an approximately three times higher lateral displacement from its square root, which could be due to the approximation of the hydrodynamic radius r as the nominal radius as well as the neglected influence of the microfluidic chamber wall in the sphere's vicinity. While the left plot for the JP's position in the figure shows a strong scattering of the tracked distances, the measurement at a higher temporal resolution reveals an oscillatory behavior. The frequency of the oscillation is approximately $25\,\mathrm{Hz}$ and is expected to be related to external (laboratory) influences on the experimental setup that are not sufficiently damped. Based on these findings, the optimization of the setup's damping from external vibrations needs to be concerned.

Further characterization of the fabricated particles could include temporally resolved Kerr microscopy measurements in order to unravel the dynamics of the magnetization reversal of an array of JPs. This could potentially show whether the magnetization of some particles' caps is reversed faster than of others in the array, from which the hypothetical influence of the stray fields from neighboring caps could be evaluated. Finally, the magnetic properties of these exchange-biased JPs should be compared to solely ferromagnetically capped particles of the same ferromagnetic material. Although vortex structures have been proven to be present in soft magnetic permalloy caps of similar size,[SKS12,SKR16] it is not known what kind of magnetization configuration ferromagnetic caps from a hard magnetic material such as $Co_{70}Fe_{30}$ possess. For the accurate modeling of the JPs' rotational motion it is furthermore necessary to measure their hydrodynamic radius for a better estimate of the viscous torque using dynamic light scattering which could potentially be combined with $\zeta-$potential measurements.

CHAPTER 7

CONCLUSION

The deposition of a magnetic thin film system on top of microspheres yields a novel type of micrometer-sized magnetic objects with spherical shape and anisotropic properties. The colloids possessing two faces are widely studied due to their unique magnetic characteristics arising from the curved geometry and due to their ability for remotely controlled transport by external magnetic fields. In the course of this work, micrometer-sized exchange-biased Janus particles were fabricated and analyzed for their physical characteristics in terms of their geometric and structural properties as well as their magnetization behavior. The central goal of this work was set in the rotational actuation of the novel magnetic objects by external magnetic fields. To compare this experimentally obtained information to a model for the rotational dynamics of a Janus particle, the subject was furthermore supposed to be treated theoretically. In order to draw a conclusion, the content of this work is summarized:

First of all, chapter 2 introduced the fundamental aspects about magnetism in flat and curved geometries and examined the current state of research with different kinds of Janus particles. With respect to the transport of magnetic particles in microfluidic environment the emerging forces were described before an overview on the microfluidic experiments and applications of Janus particles in literature was given.

The fabrication process consisting of a self-assembly and a sputter deposition step was outlined in chapter 3 before the necessary methods and devices for the physical characterization of the JPs were explained in chapter 4 along with the experimental setup which was used for the analysis of their rotational actuation.

Chapter 5 included all of the experimental performance and analysis as well as the theoretical discourse on the particles' rotational motion:
In the first place, the appearance of the fabricated Janus particles situated in hexagonal close-packed arrays or submonolayered areas on the sample was described and illustrated by scanning electron microscopy (SEM) and helium ion microscopy (HIM) images in section 5.1. Here, the differences in the particles' shape depending on the substrate used for the particle

self-assembly as well as variations of the connecting junctions created from the deposited thin film between the particles were discussed. The surface properties of the deposited curved EB films were analyzed by atomic force microscopy (AFM). However, the surface roughness was shown to be similar to the textures of planar EB thin films so that an influence from the underlying silica sphere surface could not be assigned. For a more detailed picture of the Janus particles, cross sections were produced by the use of a focused ion beam (FIB) and imaged by SEM. Most importantly, these FIB-SEM images offered the possibility to estimate the thickness gradient of the magnetic cap. The correction factor $\lambda = 66\,\%$ for a $1\,\mu m$ Janus particle was determined as the ratio between the actual cap volume with a thickness gradient and the volume of a cap with uniform thickness and could later on be implemented in the theoretical model to describe the Janus particles' rotational motion.

Next, the magnetic characteristics of a hexagonal close-packed array of Janus particles were revealed from magnetization reversal curves measured in a Kerr magnetometer with longitudinal geometry (L-MOKE) in section 5.2. The easy axis loops illustrated a significant increase of the exchange bias field, the broadness and the slope of the hysteresis curve for the exchange-biased caps in an array in comparison to a planar EB layer system, which is in agreement with the results of other groups obtained for similar microscopically structured magnetic thin films.[ZWM09] For in-plane magnetized Janus particles described in literature, the ferromagnetic caps were shown to possess mainly vortex magnetization configurations for the micrometer size range, mostly using soft magnetic materials.[MNS14,SKS12,SKR16] In contrast, an onion configuration was disclosed for the here presented exchange-biased Janus particles by magnetic force microscopy (MFM) along with topography resolving AFM measurements. From the magnetic charge contrast images it was furthermore proposed that the local magnetic moments might not be strictly aligned tangential to the particles' curved surface but rather tilted towards the equatorial plane of the Janus particles.

After the determination of the necessary physical quantities of the Janus particles had been considered in section 5.3, the derived model for the rotational dynamics of an individual Janus particle in a microfluidic chamber under the described assumptions was presented in section 5.4. The model is based on the equation of motion from balancing the viscous and the magnetic torque that both act on the Janus particle with opposite effects: The magnetic torque exerted on the cap due to the external magnetic field accelerates the Janus particle while the viscous torque damps its motion depending on the angular velocity. In order to determine the temporal evolution of the phase relation between the external field and the sphere as well as its instantaneous rotational frequency compared to the driving frequency, the differential equation was solved numerically for Janus particles of two sizes in two different liquid media with varying viscosity. From the simulated data two different rotational states were distinguished: the particle either performs a coherent rotation with a constant rotational velocity or an unstable rotation accompanied by an oscillatory behavior with an average rotational frequency that is smaller than the driving field's frequency. Furthermore, a critical ratio between the applied magnetic field's rotational frequency and its strength to obtain a stable rotation of the Janus particle coherent with the external magnetic field was found based on the assumptions of the model. Additionally, it was shown that the implementation of the thickness gradient strongly affects the predicted rotational state of the sphere.

The last section of chapter 5 (5.5) contained the analysis of the tracked data from videos recorded during the experiments for the rotational actuation of the fabricated Janus particles by external magnetic fields. Besides the description of the tracking procedure's uncertainties, the results qualitatively reproduced the rotational states previously predicted by the model. The expected increase of the critical ratio between the driving frequency and the magnetic flux density for a medium with increased viscosity was confirmed by the experimental series in which the magnetic field strength was varied for two differently viscous liquid media. Investigations on the unstable, non-coherent rotation unraveled that the average frequency of the particle is reduced for increasing driving frequencies, and thus, the relative rotational lag increases.

The comparison of the experimental and the theoretical findings for the rotational dynamics of a Janus particle indicates their qualitative agreement while deviations in the quantitative information were pointed out. Possible reasons for these findings were discussed in chapter 6 together with potential improvements for further investigations, either of experimental or theoretical nature.

To conclude, a novel type of exchange-biased Janus particle could be successfully fabricated and structurally characterized. FIB-SEM images indicated the presence of a thickness gradient for the magnetic thin film system along the particle curvature with a decrease of down to $39\pm15\,\%$ of the nominal film thickness from which a correction factor for the magnetic cap's volume was derived. The magnetic characterization revealed the presence of an onion configuration, whereas for soft magnetic materials a vortex configuration[SKS12] was previously shown to be energetically preferred. This behavior is due to the use of hard magnetic material and the additional unidirectional anisotropy of the exchange bias. A theoretical model was developed to describe a Janus particle's rotation dynamics when exposed to a rotational magnetic field, where the results of the magnetic and structural characterization were considered. In microfluidic experiments, the particles' rotational motion was investigated with respect to the driving field's strength and frequency as well as the viscosity of the carrier liquid. Overall, it was shown that the fabricated exchange-biased microspheres prove to be magnetically addressable in their rotational degrees of freedom in a controlled fashion which renders them potential actuators in mcirofluidic applications.

BIBLIOGRAPHY

[AHG05] Albrecht, M., G. Hu, I. L. Guhr, T. C. Ulbrich, J. Boneberg, P. Leiderer and G. Schatz. *Magnetic multilayers on nanospheres*. Nature Materials, 4(3), 203 (2005).

[ALS10] Amaladass, E., B. Ludescher, G. Schütz, T. Tyliszczak, M. S. Lee and T. Eimüller. *Nanospheres generate out-of-plane magnetization*. Journal of Applied Physics, 107(5), 10 (2010).

[BAM05] Behrend, C. J., J. N. Anker, B. H. McNaughton and R. Kopelman. *Microrheology with modulated optical nanoprobes (MOONs)*. Journal of Magnetism and Magnetic Materials, 293(1), 663 (2005).

[BGK03] Butt, H.-J., K. Graf and M. Kappl. *Physics and Chemistry of Interfaces*. Wiley-VCH Verlag GmbH & Co. (2003).

[BMS12] Baraban, L., D. Makarov, R. Streubel, I. Mönch, D. Grimm, S. Sanchez and O. G. Schmidt. *Catalytic Janus motors on microfluidic chip: Deterministic motion for targeted cargo delivery*. ACS Nano, 6(4), 3383 (2012).

[BS05] Bergmann, L. and C. Schaefer. *Lehrbuch der Experimentalphysik - Festkörper*. De Gruyter (2005).

[Car16a] Carl Zeiss Microscopy GmbH. *Product Information: ZEISS Crossbeam Family* (2016).

[Car16b] Carl Zeiss Microscopy GmbH. *Product Information: ZEISS GeminiSEM Family* (2016).

[Car16c] Carl Zeiss Microscopy GmbH. *Product Information: ZEISS ORION NanoFab* (2016).

[Car16d] Carl Zeiss Microscopy GmbH. *Zeiss Upgrade Info: EsB Detector* (2016).

[CG97] Chikazumi, S. and C. Graham. *Physics of ferromagnetism*. International series of monographs on physics. Oxford University Press (1997).

[Dan81] Daniatos, G. D. *Design and construction of an atmospheric or environmental SEM (part 1)*. Scanning, 4(1), 9 (1981).

[De 92]   De Gennes, P.-G. *Soft Matter (Nobel Lecture).* Angewandte Chemie International Edition, 31(7), 842 (1992).

[Dem13]   Demtröder, W. *Experimentalphysik 3: Atome, Moleküle und Festkörper.* Springer-Lehrbuch. Springer Berlin Heidelberg (2013).

[EMS16]   Erb, R. M., J. J. Martin, R. Soheilian, C. Pan and J. R. Barber. *Actuating Soft Matter with Magnetic Torque.* Advanced Functional Materials, 26(22), 3859 (2016).

[ESW11]   Ehresmann, A., C. Schmidt, T. Weis and D. Engel. *Thermal exchange bias field drift in field cooled $Mn_{83}Ir_{17}/Co_{70}Fe_{30}$ thin films after 10 keV He ion bombardment.* J. Appl. Phys., 109, 023910 (2011).

[EW14]   Eaton, P. and P. West. *Atomic Force Microscopy.* Oxford University Press (2014).

[Get08]   Getzlaff, M. *Fundamentals of Magnetism.* Springer-Verlag (2008).

[Gia05]   Giannuzzi, F. A., Lucille A ; Stevie. *Introduction to Focused Ion Beams.* Springer US (2005).

[GKS14]   Gaididei, Y., V. P. Kravchuk and D. D. Sheka. *Curvature effects in thin magnetic shells.* Physical Review Letters, 112(25), 1 (2014).

[Gre81]   Gregory, J. *Approximate Expressions for Retarded van der Waals Interaction.* Journal of Colloid And Interface Science, 83(1) (1981).

[Har99]   Hartmann, U. *Magnetic Force Microscopy.* Annual Review of Materials Science, 29, 53 (1999).

[HB65]   Happel, J. and H. Brenner. *Low Reynolds number hydrodynamics: with special applications to particulate media.* Prentice-Hall international series in the physical and chemical engineering sciences. Prentice-Hall (1965).

[HGM17]   Huckfeldt, H., A. Gaul, N. D. Müglich, D. Holzinger, D. Nissen, M. Albrecht, D. Emmrich, A. Beyer, A. Gölzhäuser and A. Ehresmann. *Modification of the saturation magnetization of exchange bias thin film systems upon light-ion bombardment.* Journal of Physics: Condensed Matter, 29(12) (2017).

[HKB15]   Holzinger, D., I. Koch, S. Burgard and A. Ehresmann. *Directed Magnetic Particle Transport above Artificial Magnetic Domains Due to Dynamic Magnetic Potential Energy Landscape Transformation.* ACS Nano, 9, 7323 (2015).

[HLG12]   Holzinger, D., D. Lengemann, F. Göllner, D. Engel and A. Ehresmann. *Controlled movement of superparamagnetic bead rows for microfluid mixing.* Applied Physics Letters, 100, 153504 (2012).

[HNS12]   Hill, R., J. A. Notte and L. Scipioni. *Chapter 2 - Scanning Helium Ion Microscopy,* volume 170 of *Advances in Imaging and Electron Physics,* pages 65 – 148. Elsevier (2012).

[Hol15] Holzinger, D. *Transport magnetischer Partikel durch maßgeschneiderte magnetische Feldlandschaften zur Anwendung in mikrofluidischen Mischprozessen.* Dissertation, Universität Kassel (2015).

[HRT97] Hubert, A., W. Rave and S. L. Tomlinson. *Imaging Magnetic Charges with Magnetic Force Microscopy.* Physica Status Solidi (B), 204, 817 (1997).

[HS09] Hubert, A. and R. Schäfer. *Magnetic Domains - The Analysis of Magnetic Microstructures.* Springer (2009).

[Huc17] Huckfeldt, H. *Strukturelle und magnetische Veränderungen in Schichtsystemen mit Grenzflächenaustauschkopplung nach dem Beschuss mit keV-Heliumionen.* Dissertation, Universität Kassel (2017).

[Huh17] Huhnstock, R. *Transport und Rotationsdynamik von asymmetrisch strukturierten, magnetischen Kolloidpartikeln.* Master thesis, Universität Kassel (2017).

[HZK13] Holzinger, D., N. Zingsem, I. Koch, A. Gaul, M. Fohler, C. Schmidt and A. Ehresmann. *Tailored domain wall charges by individually set in-plane magnetic domains for magnetic field landscape design.* Journal of Applied Physics, 114, 013908 (2013).

[Int] International Centre for Diffraction Data. *ICDD. PDF-4+.*

[Isr11] Israelachvili, J. *Intermolecular and Surface Forces.* Elsevier (2011).

[JCJ94] Jungblut, R., R. Coehoorn, M. T. Johnson, J. aan de Stegge and A. Reinders. *Orientational dependence of the exchange biasing in molecular beam epitaxy grown Ni_{80} Fe_{20} /Fe_{50} Mn_{50} bilayers (invited).* Journal of Applied Physics, 75(10), 6659 (1994).

[KKC04] Kosiorek, A., W. Kandulski, P. Chudzinski, K. Kempa and M. Giersig. *Shadow nanosphere lithography: Simulation and experiment.* Nano Letters, 4(7), 1359 (2004).

[KKP10] Kimling Née Moser, J., V. Kunej, H. F. Pernau, E. Scheer and M. Albrecht. *Magnetoresistive effects in Co/Pd multilayers on self-assembled nanoparticles (invited).* Journal of Applied Physics, 107(9), 449 (2010).

[Kni02] Knight, J. *Honey, I shrunk the lab.* Nature, 418, 474 (2002).

[KSS12] Kravchuk, V. P., D. D. Sheka, R. Streubel, D. Makarov, O. G. Schmidt and Y. Gaididei. *Out-of-surface vortices in spherical shells.* Physical Review B - Condensed Matter and Materials Physics, 85(14), 1 (2012).

[Kub13] Kubitscheck, U., editor. *Fluorescence microscopy : from principles to biological applications.* Wiley-VCH, Weinheim (2013).

[KVLD03] Kläui, M., C. A. F. Vaz, L. Lopez-Diaz and J. A. C. Bland. *Vortex formation in narrow ferromagnetic rings.* Journal of Physics Condensed Matter, 15(21) (2003).

[LLB07]   Liu, C., L. Lagae and G. Borghs. *Manipulation of magnetic particles on chip by magnetophoretic actuation and dielectrophoretic levitation.* Applied Physics Letters, 90, 184109 (2007).

[LYY16]   Lee, K., Y. Yi and Y. Yu. *Remote Control of T Cell Activation Using Magnetic Janus Particles.* Angewandte Chemie - International Edition, 55(26) (2016).

[MB56]   Meiklejohn, W. H. and C. P. Bean. *New Magnetic Anisotropy.* Physical Review, 102, 1413 (1956).

[MB57]   Meiklejohn, W. H. and C. P. Bean. *New Magnetic Anisotropy.* Physical Review, 105, 904 (1957).

[Mer18]   Merkel, M. *Einfluss von Depositions- und Feldkühlparametern auf durch Kathodenzerstäubung hergestellte polykristalline Exchange-Bias-Dünnschichtsysteme.* Master thesis, Universität Kassel (2018).

[MFO95]   Micheletto, R., H. Fukuda and M. Ohtsu. *A Simple Method for the Production of a Two-Dimensional, Ordered Array of Small Latex Particles.* Langmuir, 11(9), 3333 (1995).

[MNS14]   Mitin, D., D. Nissen, P. Schädlich, S. S. P. K. Arekapudi and M. Albrecht. *Single vortex core recording in a magnetic vortex lattice.* Journal of Applied Physics, 115, 063906 (2014).

[MSB87]   Mauri, D., H. C. Siegmann, P. S. Bagus and E. Kay. *Simple model for thin ferromagnetic films exchange coupled to an antiferromagnetic substrate.* Journal of Applied Physics, 62(7), 3047 (1987).

[Müg16]   Müglich, N. D. *Exchange-Bias-Dünnschichtsysteme: Charakterisierung, Modellierung und Anwendung.* Dissertation, Universität Kassel (2016).

[Mye99]   Myers, D. *Surfaces, Interfaces, and Colloids: Principles and Applications.* Wiley-VCH Verlag GmbH & Co. (1999).

[NWE07]   Notte, J., B. Ward, N. Economou, R. Hill, R. Percival, L. Farkas and S. McVey. *An introduction to the helium ion microscope.* AIP Conference Proceedings, 931, 489 (2007).

[Rei85]   Reimer, L. *Scanning Electron Microscopy: Physics of Image Formation and Microanalysis.* Springer Series in Optical Sciences. Springer (1985).

[RLL16]   Rampini, S., P. Li and G. U. Lee. *Micromagnet arrays enable precise manipulation of individual biological analyte-superparamagnetic bead complexes for separation and sensing.* Lab on a Chip, 16(19), 3645 (2016).

[RP77]   Reimer, L. and G. Pfefferkorn. *Rasterelektronenmikroskopie.* Springer Series in Optical Sciences. Springer, 2 edition (1977).

[RRS12] Ren, B., A. Ruditskiy, J. H. K. Song and I. Kretzschmar. *Assembly Behavior of Iron Oxide-Capped Janus Particles in a Magnetic Field.* Langmuir, 28(2), 1149 (2012).

[RZ08] Radu, F. and H. Zabel. *Magnetic Heterostructures.* Springer-Verlag, Berlin, Heidelberg (2008).

[Ses12] Seshan, K. *Handbook of Thin Film Deposition.* William Andrew Publishing, 3 edition (2012).

[SFK16] Streubel, R., P. Fischer, F. Kronast, V. P. Kravchuk, D. D. Sheka, Y. Gaididei, O. G. Schmidt and D. Makarov. *Magnetism in curved geometries.* Journal of Physics D: Applied Physics, 49(36), 363001 (2016).

[SGM09] Smoukov, S. K., S. Gangwal, M. Marquez and O. D. Velev. *Reconfigurable responsive structures assembled from magnetic Janus particles.* Soft Matter, 5(6), 1285 (2009).

[SKG15] Sheka, D. D., V. P. Kravchuk and Y. Gaididei. *Curvature effects in statics and dynamics of low dimensional magnets.* Journal of Physics A: Mathematical and Theoretical, 48(12) (2015).

[SKH16] Seong, Y., T. G. Kang, M. A. Hulsen, J. M. J. Den Toonder and P. D. Anderson. *Magnetic interaction of Janus magnetic particles suspended in a viscous fluid.* Physical Review E - Statistical, Nonlinear, and Soft Matter Physics, 93(2), 1 (2016).

[SKP11] Sinn, I., P. Kinnunen, S. N. Pei, R. Clarke, B. H. McNaughton and R. Kopelman. *Magnetically uniform and tunable Janus particles.* Applied Physics Letters, 98(2), 1 (2011).

[SKR16] Streubel, R., F. Kronast, C. F. Reiche, T. Mühl, A. U. Wolter, O. G. Schmidt and D. Makarov. *Vortex circulation and polarity patterns in closely packed cap arrays.* Applied Physics Letters, 108(4) (2016).

[SKS12] Streubel, R., V. P. Kravchuk, D. D. Sheka, D. Makarov, F. Kronast, O. G. Schmidt and Y. Gaididei. *Equilibrium magnetic states in individual hemispherical permalloy caps.* Applied Physics Letters, 101(13) (2012).

[SKS14] Sloika, M. I., V. P. Kravchuk, D. D. Sheka and Y. Gaididei. *Curvature induced chirality symmetry breaking in vortex core switching phenomena.* Applied Physics Letters, 104(25) (2014).

[SMK12] Streubel, R., D. Makarov, F. Kronast, V. Kravchuk, M. Albrecht and O. G. Schmidt. *Magnetic vortices on closely packed spherically curved surfaces.* Physical Review B - Condensed Matter and Materials Physics, 85(17) (2012).

[SO51] Segur, J. and H. Oberstar. *Viscosity of Glycerol and Its Aqueous Solutions.* Industrial and Engineering Chemistry, 43, 2117 (1951).

[SSK17] Sloika, M. I., D. D. Sheka, V. P. Kravchuk, O. V. Pylypovskyi and Y. Gaididei. *Geometry induced phase transitions in magnetic spherical shell.* Journal of Magnetism and Magnetic Materials, 443, 404 (2017).

[VOK03] Vedmedenko, E. Y., H. P. Oepen and J. Kirschner. *Size-dependent spin reorientation transition in nanoplatelets.* Physical Review B - Condensed Matter and Materials Physics, 67(1), 1 (2003).

[Was12] Waser, R. *Nanoelectronics and Information Technology - Advanced Electronic Materials and Novel Devices.* Wiley-VCH, 3 edition (2012).

[WSFX05] Wirix-Speetjens, R., W. Fyen, K. Xu, J. De Boeck and G. Borghs. *A force study of on-chip magnetic particle transport based on tapered conductors.* IEEE Transactions on Magnetics, 41(10), 4128 (2005).

[YBB12] Yan, J., M. Bloom, S. C. Bae, E. Luijten and S. Granick. *Linking synchronization to self-assembly using magnetic Janus colloids.* Nature, 491(7425), 578 (2012).

[YHH10] Yuet, K. P., D. K. Hwang, R. Haghgooie and P. S. Doyle. *Multifunctional superparamagnetic janus particles.* Langmuir, 26(6), 4281 (2010).

[YSG16] Yi, Y., L. Sanchez, Y. Gao and Y. Yu. *Janus particles for biological imaging and sensing.* The Analyst, 141(12), 3526 (2016).

[ZAV17] Zingsem, N., F. Ahrend, S. Vock, D. Gottlob, I. Krug, H. Doganay, D. Holzinger, V. Neu and A. Ehresmann. *Magnetic charge distribution and stray field landscape of asymmetric néel walls in a magnetically patterned exchange bias layer system.* Journal of Physics D: Applied Physics (2017).

[ZLL12] Zhang, Y. J., W. Li, J. Li, Y. M. Zhang, Y. X. Wang, S. Y. Yang, S. S. Liu, L. C. Wu, G. S. Beach and J. H. Yang. *Perpendicular exchange bias of Pt/Con/CoO multilayer on ordered nanosphere arrays.* Journal of Applied Physics, 111(5) (2012).

[ZWM09] Zhang, Y. J., Y. X. Wang, X. D. Meng, Y. Liu, X. Ding and J. H. Yang. *Exchange bias of NiO/FeNi ordered nanocaps on curved substrate.* Journal of Applied Physics, 105(8) (2009).

FREQUENTLY USED TERMS AND ABBREVIATIONS

AF	Antiferromagnet
AFM	Atomic Force Microscopy
Bead	(Micro-)Particle
Beadsize	Diameter of the considered particle
EB	Exchange Bias
F	Ferromagnet
FIB	Focused Ion Beam
fps	frames per second
HIM	Helium Ion Microscope
LOC	lab-on-a-chip
L-MOKE	Longitudinal Magneto-optical Kerr Effect
	Longitudinal Magneto-optical Kerr Magnetometer
JP	Janus Particle
MOKE	Magneto-optical Kerr Effect
MFL	Magnetic Field Landscape
MFM	Magnetic Force Microscopy
SEM	Scanning Electron Microscope
SPP	Superparamagnetic Particle
w%	Percent weight fraction

DANKSAGUNG

Wenn ich nun auf den letzten Seiten dieser Arbeit die Möglichkeit habe, einigen Menschen für ihren Beitrag zu dieser Arbeit zu danken, dann beginne ich damit bei PROF. DR. ARNO EHRESMANN. Vielen Dank Arno, dass du mir zunächst das Anfertigen dieser Arbeit in deiner Arbeitsgruppe ermöglicht hast, und für deine Offenheit in Gesprächen auch über die Wissenschaft hinaus, die du trotz straffen Zeitplans auch deinen Studenten entgegenbringst.

Bei PROF. DR. THOMAS KUSSEROW bedanke ich mich zunächst für die Übernahme des Zweitgutachtens dieser Arbeit. Ebenso wichtig war für mich aber auch die lehrreiche gemeinsame Durchführung der FIB-SEM Messungen, während denen ich meine Partikel noch einmal aus einer ganz neuen Perspektive kennen lernen konnte. Danke!

I also want to thank DR. KAI ARSTILA from the Physics Department in Jyväskylä for his spontaneous approval of my request to conduct some HIM measurements on a Saturday afternoon during my vacation in Finland. Paljon Kiitoksia.

Wie ich mich bei DR. DENNIS HOLZIGER bedanken kann, bleibt mir schleierhaft. Dennis, du bist einfach ein super klasse spitzenmäßiger Betreuer. Danke für den wissenschaftlichen Austausch, die allzeit beruhigenden Worte in Momenten des Verzagens, die geleisteten Hilfestellungen und vor allem für die Zeit, die du aufgewendet hast, um diese Arbeit mit konstruktiven Verbesserungsvorschlägen zu bereichern. In diesem Zuge gilt außerdem IRIS KOCH ein Dank für die Einführung in die englische Kommasetzung, die ich sicherlich an vielen Stellen trotzdem nicht beherrscht habe. Nicht zu vergessen die vielen Stunden, die ich entweder mit dir oder mit ALEXANDER GAUL oder mit euch beiden vorm AFM verzweifelt bin. Danke euch beiden. ANDREEA TOMITA und RICO HUHNSTOCK, euch gebührt mein Dank dafür, dass ihr mich in das Janus Partikel Team aufgenommen habt!

Bei ANDREAS NEHLS und ANDREA WECKER möchte ich mich außerdem bedanken: Ohne euch würde in diesem Laden gar nichts laufen!

STATEMENT OF AUTHORSHIP

I hereby declare that this submitted master thesis is my own work. All supporting material and sources used are acknowledged as references. I assure that passages which were literally or analogously taken from published documents are marked with the corresponding citation within the text.

Place, Date		Signature